Facultat de Física

Departament de Física Atòmica, Molecular i Nuclear

Vniversitat de València

Future Linear Colliders

Detector R&D, Jet Reconstruction and Top Physics potential

Ignacio García García

PhD thesis under the supervision of
Marcel Vos and Eduardo Ros Martínez

Doctorado en Física, Mención Internacional

Diciembre de 2016

Dr. Marcel Vos,
Científico titular del CSIC, y

Dr. Eduardo Ros,
Investigador científico del CSIC

CERTIFICAN:

Que la presente memoria **Future Linear Colliders: Detector R&D, Jet Reconstruction and Top Physics potential** ha sido realizada bajo su dirección en el Departamento de Física Atómica, Molecular y Nuclear de la Universidad de Valencia por D. Ignacio García García y constituye su trabajo de tesis doctoral para optar al grado de Doctor en Física.

Y para que así conste, firman el presente certificado.

Firmado
Dr. Marcel Vos

Firmado
Dr. Eduardo Ros

El trabajo descrito en esta tesis se ha llevado a cabo en el **Instituto de Física Corpuscular** (IFIC) en Valencia, España.

El IFIC es un centro mixto del Consejo Superior de Investigaciones Científicas (CSIC) y de la Universitat de València. En Julio de 2015 recibió la acreditación **Severo Ochoa** (SEV-2014-0398) que le distingue como Centro de Excelencia. Dicha acreditación reconoce la excelencia y las contribuciones científicas que realizan los centros y unidades a nivel nacional e internacional, su impacto empresarial y social y su capacidad para atraer talento.

Abstract

During the 20^{th} century, discoveries and measurements at colliders, combined with progress in theoretical physics, allowed us to formulate the Standard Model of the interactions between the constituents of matter. Today, there are two advanced projects for a new installation that will collide electrons and positrons covering an energy range from several hundreds of GeV to the multi-TeV scale, the International Linear Collider (ILC) and the Compact Linear Collider (CLIC). These Future Linear Colliders give the opportunity to study the top quark with unprecedented precision. Measurements of top quark properties are of special interest, as the top quark is the heaviest elementary particle of the SM. Precision measurements of top quark properties at e^+e^- colliders promise therefore to be highly sensitive to physics beyond the SM.

This thesis has three complementary parts. The first is dedicated to the R&D of the ILD detector concept for future e^+e^- colliders, more precisely, the innermost region of the detector. A thermo-mechanical characterization of ultra-thin self-supporting silicon sensors is carried out and a first mock-up of the forward tracker is designed and characterized. Additionally, the possibility of integrated micro-cooling circuits in the active silicon sensors is demonstrated.

The program of precision physics scheduled for future colliders requires excellent detectors, but it also demands the best reconstruction algorithms. In the second part of the thesis the jet reconstruction performance is evaluated at different centre-of-mass energies and a new sequential jet reconstruction algorithm is proposed to deal with the expected $\gamma\gamma \to hadrons$ background levels at ILC and CLIC.

The last part is focused on the top quark physics potential of future colliders. I demonstrate that both projects can constrain the top quark $\mathcal{CP}$-conserving electroweak couplings and $\mathcal{CP}$-violating couplings to the % level. The potential of an e^+e^- collider with polarized beams, an integrated luminosity of 500 fb^{-1} and centre-of-mass energies of $\sqrt{s} = 500\,\text{GeV}$ for ILC or $\sqrt{s} = 380\,\text{GeV}$ for CLIC is studied in full simulation. The sensitivity to new physics is over an order of magnitude with respect to what is expected from LHC.

Contents

Chapter 1

The Standard Model of Particle Physics and the Top Quark

1.1 Historical overview

The concept of elementary particles or elementary entities was proposed for the first time by ancient greeks under the name of atoms. However, the concept of indivisible components of matter evolved over time. In the second half of 19^{th} century atomic spectra were studied by chemists and Mendeleiev established the well-known periodic table of elements in 1869[1].

1.1.1 The birth of the modern atom

Pioneering work at the end of the 19^{th} century using cathode ray tubes, radioactive materials and photographic plates began the revolution that was to produce atomic physics. In 1895, W. C. Röntgen discovered an unknown radiation produced in cathode ray tubes which called X-rays. A year later, Becquerel observed that some materials, such as uranium, leave a signal on photographic plates due to its radioactive nature. Finally, J. J. Thomson interpreted cathode rays as 'electrons' and proposed a model of the atom consisting of a swarm of many of electrons with a balancing positive charge.

The beginning of the new century was marked by Planck's discovery of the black-body radiation law. The physical interpretation of this phenomenon led to postulate that energy was quantized. In 1905 Einstein used the Planck constant h to explain the photoelectric effect observed by Herz in 1887. Figure 1.1 shows how illuminated metals emit electrons. The energy of the electrons depends on the frequency of the light, not on its intensity. Einstein's explanation postulates that light of frequency ν is composed of individual quanta -now known as photons- of energy $h\nu$.

[1] This section tries to introduce the reader in the world of particle physics in an informative way, from the first particle discovered in simple experiments to the huge particle colliders of the last decade. This historical review is based on References [1, 2, 3, 4] where a more exhaustive description of the particle discoveries and experiments is done.

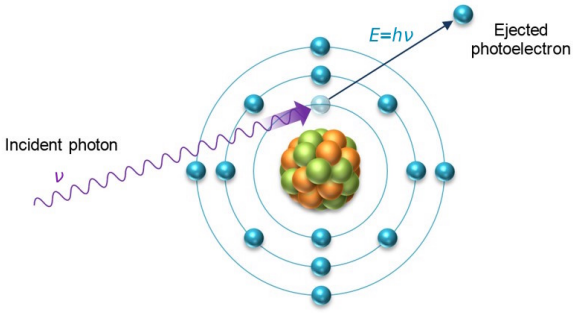

Figure 1.1: The photoelectric effect

Investigations of radioactivity performed by Geiger, Marsden and Rutherford in 1911, consisting in bombarding a thin metal foil with α particles, proved that the atom has a small nucleus with a charge $Z|e|$. Two years later Niels Bohr's atomic model reproduced the electron energy levels and obtained the radius of the hydrogen atom, combining the electron mass m_e and electron charge e with h. Afterwards Rutherford himself proved that the hydrogen nucleus was a fundamental constituent of all other nuclei. He broke a nitrogen nucleus with α particles and extracted hydrogen nuclei which were later called 'protons'.

During the years 1924-1927, quantum mechanics developed rapidly, from de Broglie's waves until Heisenberg's matrix mechanics expressed in the Schrödinger's equation and Dirac's formulation of transition amplitudes. The problem of the electronic structure of the atom was reduced to a set of differential equations, approximations which explained not just hydrogen, but all atoms.

Despite the progress, the structure of the nucleus remained a mystery. By 1926 it was understood that all particles were divided into two classes according to their intrinsic angular momentum, known as 'spin'. Those with half-integer spin (in units of $\hbar = h/2\pi$) are called fermions, while those with integer spin are called bosons. These fundamental facts about spin could not be reconciled with the prevailing picture of the nucleus N_7^{14} composed by 14 protons and 7 electrons. As these are both fermions the nucleus should be a fermion with half-integer spin, but it was shown to have spin 1. The nitrogen spin inconsistency and the enigma of the composition of the nucleus were solved with the discovery of the neutron by Chadwick in 1932. The experiment consisted in bombarding beryllium with α particles. He showed that the electrically neutral radiation that is produced in the process consisted of neutral particles with about the same mass as the proton, later called 'neutrons'. The modern atom was completed. A nucleus with charge Z and mass number A is composed on Z protons and $A - Z$ neutrons surrounded by Z electrons.

1.1.2 The leptons: beyond electrons

As discussed, the electron was the first elementary particle to be identified. In 1906, Millikan measured the electric charge by observing tiny charged droplets of oil between two horizontal metal electrodes. According to the theory developed by Pauli in 1927, the electron spin takes a value of 1/2. The electron therefore is the first element of a family of particles called 'leptons'.

The positron, e^+

Experiments using X-rays and radioactive sources were limited to energies of a few MeV. To obtain higher energy particles it was necessary to use cosmic rays, observed for the first time by V. Hess in 1912, who ascended by balloon with an electrometer to an altitude of 5000 m. Anderson, together with Millikan, studied cosmic-ray particles in a cloud chamber when he discovered the 'positron' in 1933, a particle with the same mass as the electron but the opposite charge. Just a few years before, Dirac's relativistic wave equation for electrons had already predicted the existence of such a particle. Anderson's positron e^+, Thomson's electron e^- and Einstein's photon γ filled all the roles called for in Dirac's relativistic theory.

Muons, μ^- and μ^+

Anderson and Neddermeyer continued studying cosmic radiation. Anderson had observed a new penetrating component of the cosmic rays, particles that curved differently from electrons when passed through a magnetic field. They were negatively charged but curved less abruptly than electrons, but more abruptly than protons, for particles of the same velocity. To account for the difference in curvature, it was supposed that this kind of particles is heavier than an electron but lighter than a proton.

In 1935 Hideki Yukawa predicted the existence of a particle of mass intermediate between electron and proton, around 200 MeV/c^2. This particle was to carry the nuclear force in the same way as the photon carries the electromagnetic force. It was thought initially that Anderson's observation could be consistent with Yukawa's particle. However, in late 1937, Street and Stevenson reported a track that ionized too much to be an electron with the measured momentum, but traveled to far to be a proton. The existence of the 'muon', μ, the second lepton, was confirmed. A decade later, the group formed by Lattes, Occhialini and Powel discovered the pion, π (the Yukawa-like particle), and explained the origin of the penetrating component of the cosmic rays using emulsions.

Electronic and muonic neutrinos (ν_e, ν_μ)

The discovery of the neutron was the key to understanding nuclear β decay. However the problem of the energy non-conservation in some nuclear decay reactions remained. In order to explain this incongruence, in 1930, Pauli postulated the existence of a light, neutral, feebly interacting particle. It was later called 'neutrino', a name coined by Fermi, and was believed to be unobservable. At the time the decay of a neutron from

a nucleus was being considered as a 2-body process, $n \to pe$, that implies a mono-energetic electron signal rather than a continuous distribution. The success of the Fermi theory was convincing evidence for the existence of the neutrino. However, still there had been no detection of interactions by the neutrinos themselves until Cowan and Reines succeeded to observe them in an experiment made in 1956. They used the enormous number of antineutrinos produced in β decays inside a nuclear reactor and water with cadmium and scintillators as detector. The process $\bar{\nu}p \to e^+n$ was observed by detecting both the e^+ and the neutron.

The first theory of the neutron decay $n \to pe\bar{\nu}$, now called 'weak interaction', was proposed by Fermi in 1933. A 4-body point-like interaction without intermediate particle and including a coupling constant G_F nowadays known as Fermi constant. During the next few years the universality of the theory became evident. It was suggested that the pairs (e, ν), (μ, ν) and (n, p) entered into the weak interaction in an equivalent way. Nuclear β decays and, pion and muon decays could be explained considering the interaction of these particle pairs.

Soon after, strong focusing led to the construction of much higher-energy proton machines. The Alternating Gradient Synchrotron (AGS) was completed at Brookhaven in 1960. In 1962, Schwarz, Steinberger and Lederman reported results where neutrino interactions were observed. The neutrino beam was generated by directing the 15 GeV proton beam of AGS to a beryllium target, where secondary kaon and pion decays produced the neutrinos. They observed that neutrinos from the beam could only produce muons but never electrons. This experiment showed that ν_e and ν_μ were distinct particles and there were two conserved quantum numbers, one for muons and another for electrons.

The third lepton, τ

In the following years the construction of e^+e^- storage rings became the way to go ahead in particle physics. Fermion-antifermion pairs were expected to be produced in the e^+e^- annihilation, like the process $e^+e^- \to \mu^+\mu^-$. However in 1975, a team under M. Perl working in the MARK-I experiment of the e^+e^- colliding-ring SPEAR at SLAC, observed events with a muon produced together with an electron of opposite charge and missing particles. They interpreted these events as the pair production of a new lepton, tau (τ), followed by its leptonic decays, $\tau \to e\nu\nu$ and $\tau \to \mu\nu\nu$. The third member of the leptons family was discovered. It is much heavier than the other leptons, and could only be produced in high energy collisions.

The tau neutrino, ν_τ

After the τ discovery there was no doubt about the existence of a third neutrino, ν_τ, but it took a long time to be observed. In 2000, an international collaboration of physicists at Fermilab, made the discovery after a three-year analysis of data from the Direct Observation of the Nu Tau (DONUT) experiment. The DONUT team fired an intense beam of neutrinos, which they expected to contain tau neutrinos, at a target consisting of iron plates with layers of emulsion sandwiched between them. One in 10^{12} tau neutrinos interacted with an iron nucleus to produce a tau lepton, which

subsequently decayed leaving a characteristic track in the emulsion that the team could identify. The lepton family had been completed, in today's Standard Model it is composed by the particles (e, μ, τ) and $(\nu_e, \nu_\mu, \nu_\tau)$.

1.1.3 The era of quarks

Once Yukawa's particle, the pion, was finally discovered, it was soon realized that protons, neutrons and pions were just the first members of a new family of particles. These hadrons differ from leptons, as they manifest strong interactions. This family is divided into two main groups: *mesons*, when the spin is integer, and *baryons*, when the spin is half-integer. The development of more powerful particle accelerators and the measurement of the scattering cross sections uncovered new particles in the form of resonances, particles with extremely small lifetimes. As more particles and resonances were found, certain patterns appeared. It was known that the different processes observed at experiments had to conserve parity symmetry and conserve total angular momentum[2]. The discovery of the π^0 completed the triplet of pions: π^+, π^0, π^-. The approximate equality of the charged and neutral pion masses had already been observed in the neutron and proton masses. It led nuclear physicists to postulate an approximate symmetry, the isotopic spin or *isospin*. Thus as the nucleons represent an isospin doublet, the pions represent an isospin triplet.

In 1953, the Cosmotron at Brookhaven National Laboratory provided an especially important result, the observation of four events in which a pair of unstable particles was produced. If the decays of these particles involved strong interactions, the particle lifetimes should have been ten orders of magnitude smaller than observed. They were called strange particles. The explanation of this unexpected result was given by Gell-Mann and Nishijima, introducing a new additive quantum number called *strangeness*.

The eightfold way and u, d, s quarks

Isospin symmetry could be represented by the neutron and proton, which has the mathematical structure of $SU(2)$. Gell-Mann and Ne'eman proposed a model that was an extension of SU(2) adding strangeness, a SU(3). Baryons and mesons were grouped in octets or combinations of them. It was called the "eightfold way". In Figure 1.2 the baryon and meson octets are displayed. The discovery of a new baryon known as Ω^- by Samios and collaborators in 1964, completed the decuplet of particles with spin 3/2, shown in Figure 1.3

A clearer understanding of SU(3) emerged when Gell-Mann and, independently, G. Zweig, proposed that hadrons were built from three basic constituents, "quarks". Now called u ("up"), d ("down") and s ("strange"), these could explain why the eightfold way was so successful. Mesons were composed of a quark (q) and an antiquark $(\bar{q})$ while baryons are produced from three quarks. For instance, a proton is formed by the combination uud, a neutron by udd, whereas the meson K^0 is a strange particle

[2]Total angular momentum, J, comes from the combined spin angular momentum, s, with the orbital angular momentum l; Parity, P, is defined as $(-1)^{-l}$. Each particle has its own J^P numbers.

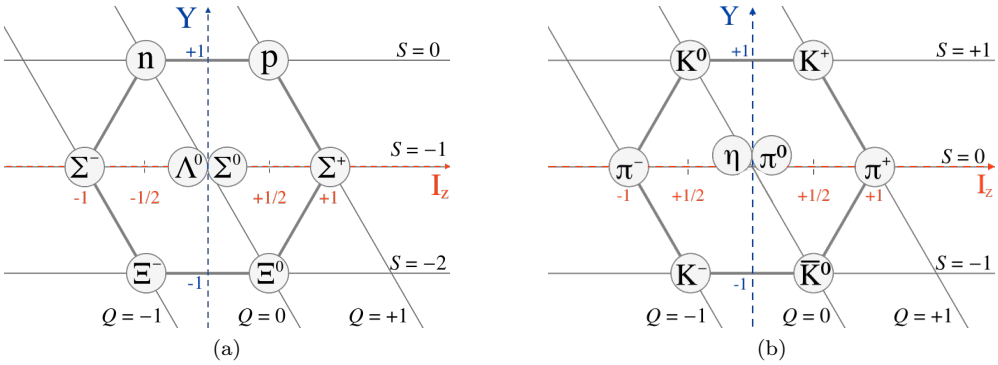

Figure 1.2: The horizontal direction measures I_z, the third component of isospin. The vertical axis measures the hypercharge $Y = B+S$, the sum of baryon number and strangeness. (a) The baryon $J^P = 1/2^+$ octet containing the proton and the neutron. (b) The pseudoescalar (meson) octet.

formed by $d\bar{s}$. Quarks have spin 1/2 and fractionary charge, assigning a charge to the *up* quark of $+2/3e$ (where e is the electron charge) and -1/3e to the other two.

In the late 1960s, deep inelastic electron scattering became a powerful tool to explore nucleon constituents. An example is the experiment carried out by the SLAC-MIT groups, where they scattered electrons from a hydrogen target and detected the outgoing electrons in a large magnetic spectrometer. The most important result was the discovery of "scaling" behaviour, a concept anticipated by Bjorken in 1967. It suggested that experimentally observed strongly interacting particles (hadrons) behave as collections of point-like constituents when probed at high energies. Scaling implied independence of the absolute resolution scale, and hence effectively point-like substructure. The observation of scaling by experiments at SLAC reinforced the faith in quarks as physical entities.

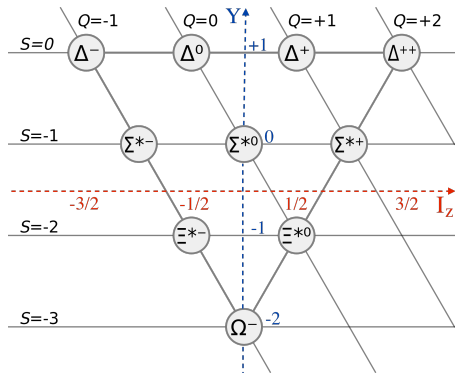

Figure 1.3: The J^P=$3/2^+$ decuplet completed by the discovery of the Ω^-.

Richard Feynman subsequently formulated the parton model. In this picture there were three "valence" quarks in the nucleons that dominated the process of electron scattering, an in addition a "sea" of low-momentum quark-antiquark pairs. The quark-parton model and the experimental confirmation, inspired the formulation of Quantum Chromodynamics (QCD). In this theory the interactions between quarks are the result of exchanging vector particles, called gluons, of spin 1. When a quark scatters, it emits gluons and some of its momentum is given to them. QCD adds a new quantum number, "colour", with an SU(3) structure. Each parton came in three versions, i.e., red, blue and green.

The J/ψ resonance and the c quark

In 1974 the period known as the "November Revolution" began. The J and ψ resonances with 3.1 GeV mass were discovered simultaneously at Brookhaven National Laboratory and SLAC. Once it was realized that they had discovered the same particle, the two teams agreed to name it J/ψ. This particle could not be understood without considering a fourth quark in addition to the original three, the "charmed" or c-quark. A $c\bar{c}$ bound state is the simplest way to explain the absence of neutral strangeness-changing weak currents observed.

The new quark seemed to complete a family of fermions, (c, s, ν_μ, μ), analogously to (u, d, ν_e, e). As pointed out in the Section 1.1.2, during this exciting period of investigation, the τ lepton was also discovered. Hence the third lepton and its neutrino augured a new pair of quarks. Consequently, experiments were extended to search for the next quark.

The b quark

In 1977, the team under L. Lederman at Fermilab discovered the fifth quark, named "bottom" or "beauty". They studied collisions of 400 GeV protons on nuclear targets. Their apparatus was a double-arm spectrometer intended to measure $\mu^+\mu^-$ pairs. A statistically significant peak was observed in the 9.5 GeV region and further analysis certified the discovery of a new resonance named Υ (a $b\bar{b}$ bound state). The story of the J/ψ was recurring. A year later the PLUTO and DASP II detectors in the e^+e^- storage ring DORIS at DESY determined the mass of Υ with better precision and extracted the charge of the b quark, -1/3.

Gluons

QCD postulated the dependence of the strong coupling α_s, between quarks and gluons, on the momentum transfer Q^2. Corrections to the process $e^+e^- \to q\bar{q}$ produce $e^+e^- \to q\bar{q}g$, where g is a gluon. The cross section for this is of order of α_s relative to the process in which no gluon is produced. The $q\bar{q}g$ state could be produced at the SPEAR or DORIS rings, but higher energies were needed to distinguish the $q\bar{q}g$ from the $q\bar{q}$, because both states merged. This was achieved first at PETRA e^+e^- collider located at DESY, which was able to reach more than 30 GeV total center-of-mass energy. This ring had four detectors, TASSO, PLUTO, MARK-J and JADE. All of them

found evidence for the $q\bar{q}g$ final state. They observed that as energy increased, more and more events with a gluon were produced. Some of the events displayed a clean three-jet[3] topology, giving visual evidence for the existence of the gluon, as shown Figure 1.4.

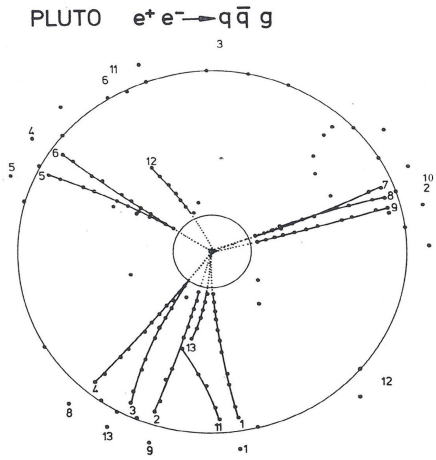

Figure 1.4: An evident 3-jet event (interpreted as $q\bar{q}g$) from PLUTO data at PETRA. [5]

The top quark

After these remarkable events, nobody doubted that the sixth quark must exist. Grouping the quarks in pairs (u, d) and (c, s) according to their charge, the existence of a sixth quark was necessary to complete the third pair together with the b, the t quark or "top". The race for discovering the top quark had started. However, it took a long time until the top quark was directly seen for the first time. The discovery of the W and Z bosons, and the Standard Model (explained in Sections 1.1.4 and 1.2) indicated where to search for the new quark. The top quark decay would be $t \to Wb$ and the W could decay leptonically ($l\nu$) or hadronically ($q\bar{q}$). This, together with the predicted mass around 180 GeV, was the key to discover the top quark in 1995 by the CDF and DØ detectors operating at the 1.8 TeV Tevatron $p\bar{p}$ collider at FERMILAB.

1.1.4 From neutral currents to the Higgs discovery

Fermi's theory of weak interactions was based on the analogy with electromagnetism; from the start it was clear that there might be vector particles transmitting the weak force the way the photon transmits the electromagnetic force. Since the weak interaction is of short range, the vector particle would have to be heavy, and since β decay

[3] A jet is a narrow cone of hadrons and other particles produced by the hadronization of a quark or gluon.

changed nuclear charge, the particle would have to carry charge too. The weak (or W boson) was the object of many searches. In 1961, Glashow developed a model that unified the weak and electromagnetic interactions. This model could accommodate particles like the photon and W^+ and W^-. In addition a new particle was required, the Z boson, neutral like the photon, but heavy. The problem of this theory was that all fields were gauge fields and therefore massless and unphysical.

An important advance was made by Peter Higgs and others, who in 1964 showed how a theory initially containing a massless photon and two scalar particles could turn into a theory with a massive vector particle and one scalar. This "Higgs mechanism" was adopted by Weinberg and Salam to complete Glashow's model and develop the Standard Model of electroweak interactions (a detailed description is given in Section 1.2). The particles of this model were denoted W^+, W^-, W^0 and B. The W's conform the vector particles and B is the scalar. The Higgs mechanism gives mass to the $W^\pm$ bosons, and at the same time, the two neutral particles W^0 and B mixed to produce two physical particles, a massless photon and a Z with a mass comparable to that of the $W^\pm$.

W and Z bosons

Neutral currents had been searched for in Kaon decays without success; they had to be very rare or nonexistent. The large electromagnetic effect always masked the neutral weak current in these processes. It was later realized how to avoid this. The idea was to look for scattering initiated by a neutrino that emitted a Z that subsequently interacted with a nuclear target. Photons could not be emitted, as neutrinos are neutral. The discovery of neutral currents was made in 1973 in the Gargamelle bubble chamber at CERN. The experiment made use of muon antineutrino and neutrino beams. Just one event of the type $\nu_\mu e \to \nu_\mu e$, shown in Figure 1.5, without a final-state muon, was observed. Apart from finding evidence of neutral current events, the experiment measured later, with more statistics, the ratio of neutral to charged currents. This allowed to predict the masses of the W and Z bosons at about 80 and 91 GeV, respectively.

The promising theory of electroweak interactions encouraged to build higher energy machines. A few years later, the CERN super proton synchrotron (SPS) was transformed into a proton-antiproton colliding machine according to the design by C. Rubbia and S. van der Meer, the S$p\bar{p}$S Collider. Quarks from protons colliding with antiquarks from antiprotons could produce the W and the Z bosons at this new powerful accelerator. For instance, if a u quark and a $\bar{d}$ quark collided, a W^+ could be created if the energy of the pair was near the mass of the W. As expected, the W and Z bosons were discovered, in 1983 and 1984 respectively, by the two large detectors, UA-1 and UA-2 at the S$p\bar{p}$S. They were detected via their leptonic decays: $W \to l\nu$ and $Z \to l^+l^-$, l being an electron or a muon. The measured masses are in good agreement with previous predictions of the Standard Model. The W^+, W^-, and Z bosons, together with the photon (γ), constitute the four gauge bosons of the electroweak interaction.

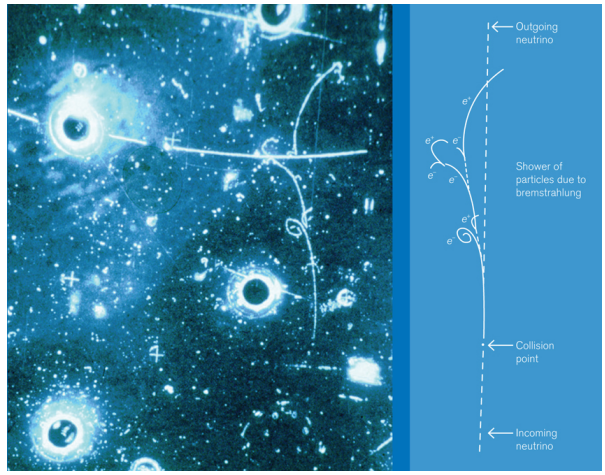

Figure 1.5: Neutral current event observed by the Gargamelle experiment at CERN.

The Higgs boson

The Standard Model was still not complete. The Higgs mechanism required the existence of a new boson, called Higgs boson. The first attempt to search for the Higgs boson was done at the e^+e^- collider Large Electron-Positron Collider (LEP) at CERN in the 1990s. The Higgs boson could be produced through its gauge coupling to the Z, i.e., $e^+e^- \to Z \to ZH$. The LEP searches did not find any conclusive evidence of a SM Higgs boson. The data from the four detectors was combined and a lower bound on the Higgs mass was set at 114.4 GeV.

The search continued at Fermilab with the Tevatron proton-antiproton collider. There was no guarantee that the Tevatron would be able to find the Higgs boson because its mass remained unknown. The CDF and D$\emptyset$ detectors were only able to exclude further ranges for the Higgs mass between 156 GeV and 177 GeV.

Years later the Large Hadron Collider (LHC) at CERN was built in the same 27 km tunnel where LEP was located, a proton-proton collider of up to 7 TeV of energy per beam. One of its goals was to confirm or exclude the existence of the Higgs boson. Collisions at these energy levels should be able to reveal it. Data collection at the LHC started in March 2010. At the end of 2011 the two main particle detectors, ATLAS and CMS had seen among their results an excess around 125 GeV that was becoming too large to ignore. Rapidly both experiments put their effort in finding the Higgs in the energy range around 115–130 GeV and again small but consistent excesses of events were observed across multiple channels. The decay modes observed with greatest significance were $H \to \gamma\gamma$ and $H \to ZZ \to 4$ leptons. Finally, on 4 July 2012, ATLAS and CMS announced they had independently made the same discovery: an unknown boson of mass around 125-126 GeV with a local significance of 5σ. This level of evidence met the formal level of proof required to announce a confirmed discovery.

It is necessary to measure the properties of this new boson accurately to verify its Higgs-like nature. In 2013 the spin-parity of this particle was confirmed. The spin 0 and the even parity strongly indicated that it was a Higgs boson. Coupling measurements so far, with a precision ranging from 10 to 100%, are compatible with the Standard Model.

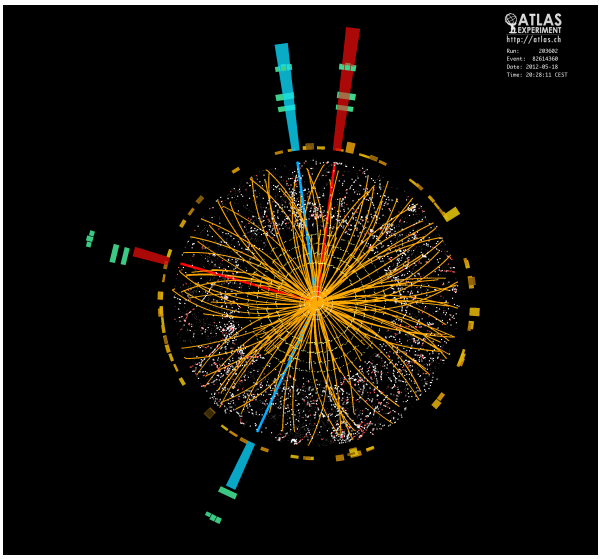

Figure 1.6: Event display of a ($H \rightarrow 4e$) Higgs boson candidate from collisions in 2012 between protons in the ATLAS detector on the LHC.

After the Higgs discovery, the last piece of the puzzle, the Standard Model of particle physics is complete. A theory that describes in a satisfactory way all interactions currently known, except gravity. In the following Section 1.2, the particle content, structure and symmetries of the Standard Model Lagrangian are presented.

1.2 The Standard Model of particle physics

The Standard Model constitutes one of the greatest achievements in modern physics. It provides an elegant theoretical framework, which is able to describe the known experimental facts in particle physics with high precision. It is a relativistic quantum field theory based on the symmetry group $SU(3)_C \otimes SU(2)_L \otimes U(1)_Y$, which describes strong, weak and electromagnetic interactions, via the exchange of spin-1 gauge fields.

The development of the SM was driven by the interplay between theory and experiment. In spite of the impressive phenomenological success discussed in previous section, the SM leaves too many unanswered questions to be considered as a complete description of the fundamental forces. It does not incorporate the theory of gravitation as described by general relativity and does not contain any viable dark matter particle that possesses all of the required properties deduced from observational cosmology. It

also does not incorporate neutrino oscillations and non-zero neutrino masses. For this reason the SM is sometimes regarded as "the theory of almost everything" [2].

1.2.1 Particle content and interactions

All ordinary matter[4] around us is made up of elementary particles. These particles occur in two basic types called quarks and leptons. Each group consists of six particles, which are related in pairs or "generations". The lightest and most stable particles make up the first generation, whereas the heavier and less stable particles belong to the second and third generations. All stable matter in the universe is made up of particles that belong to the first generation; any heavier particles quickly decay to the next most stable level. The six quarks are paired in the three generations, the *up* and *down* quarks form the first generation, followed by the *charm* and *strange* quarks, then the *top* and *bottom* (or beauty) quarks. Additionally quarks come in three different "colours" and only mix in such ways as to form colourless objects. The six leptons are similarly arranged in three generations, the *electron*, the *muon*, the *tau* and their respective *neutrinos*, as shown in Figure 1.7. The electron, the muon and the tau all have an electric charge and a sizable mass, whereas the neutrinos are electrically neutral and have very little mass.

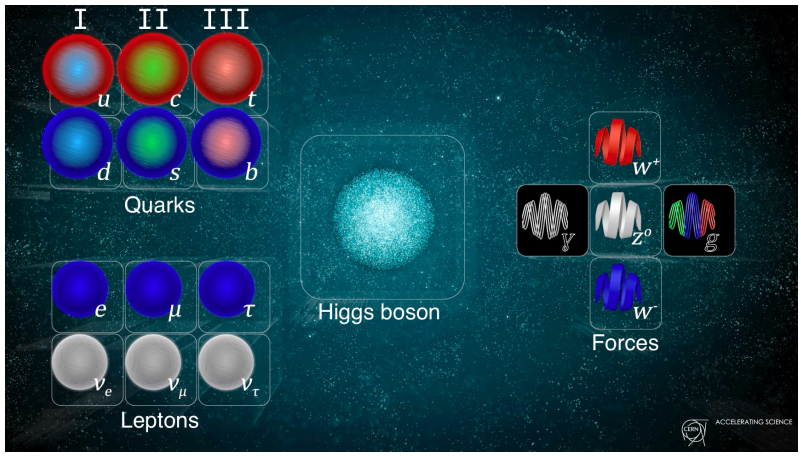

Figure 1.7: The particle content of the Standard Model. On the left, fermions, the building blocks of matter, are subdivided into three families of quarks and leptons. On the right, vector bosons that carry the electromagnetic, weak and strong forces. In the middle, the Higgs boson, responsible for providing mass to all massive particles.

There are four fundamental forces at work in the universe: the strong force, the weak force, the electromagnetic force, and the gravitational force. They act over different ranges and have different strengths. Gravity is the weakest, but is a far-reaching interaction. The electromagnetic force is far-reaching as well, but it is many times

[4]The standard model of cosmology indicates that the total mass–energy of the universe contains 4.9% ordinary matter, 26.8% dark matter and 68.3% dark energy [6]

stronger than gravity. The weak and strong forces are effective over a very short range and dominate only at the level of subatomic particles. Despite its name, the weak force is much stronger than gravity, but it is indeed the weakest of the other three. The strong force, as the name suggests, is the strongest of all four fundamental interactions. Three of the fundamental forces result from the exchange of force-carrier particles, which belong to a broader group called "bosons". Particles of matter transfer discrete amounts of energy by exchanging bosons with each other. Each fundamental force has its own corresponding boson, the strong force is carried by the *gluon*, the electromagnetic force is carried by the *photon*, and the $W^{\pm}$ and Z bosons are responsible for the weak force.

The fifth boson is the Higgs boson, associated with the Higgs field which gives mass to leptons (except neutrinos), quarks, W and Z bosons, and the Higgs boson itself.

1.2.2 Local gauge symmetries

Gauge theories and symmetry principles provide us with a comprehensive description of the presently known fundamental particles and interactions. The SM is based on gauge theories, and the interactions between the elementary particles are governed by a symmetry principle, namely local gauge invariance, which represents an infinite dimensional symmetry group. Global symmetries, such as isospin, or flavour symmetry, are only approximate symmetries and therefore they are not connected to gauge interactions. There is no explanation available for this rule, but gauge interactions play a fundamental role in our present understanding of particle interactions. The mathematical formalism of local gauge symmetries is detailed in Appendix B.1.

a) Quantum electrodynamics

The simplest example of local gauge theory is Quantum Electrodynamics (QED), the quantum field theory of the electromagnetic force. QED mathematically describes all phenomena involving electrically charged particles interacting by means of exchange of photons and represents the quantum counterpart of classical electromagnetism giving a complete account of the interaction between matter and light.

QED is an abelian gauge theory with the symmetry group $U_{em}(1)$ and has one gauge field, the electromagnetic four-potential, with the photon being the gauge boson. The Lagrangian of QED predicts the massless nature of photons. Experimentally we know $m_\gamma < 1 \times 10^{-18}$ eV [3].

In QED, the coupling constant that determines the strength of the electromagnetic interactions is known as the fine-structure constant, $\alpha = \frac{e^2}{4\pi\epsilon_0\hbar c}$. The SM does not predict its value. Therefore, α must be determined experimentally. In fact, α is one of the about 20 empirical parameters in the SM. The most stringent QED test comes from the high-precision measurement of the e and μ anomalous magnetic moments $a_l \equiv (g_l^\gamma - 2/2)$, where $l = e, \mu$. The values of $a_e \approx 10^{-12}$ and $a_\mu \approx 10^{-10}$ are fully compatible with predicted value of the gyromagnetic factor $g_l^\gamma = 2$ by the Dirac equation. Specifically, the measurement of a_e provides the most accurate determination of

the fine-structure constant [3]

$$\alpha^{-1} = 137.035\ 999\ 074 \pm 0.000\ 000\ 032 \tag{1.1}$$

The impressive precision of this value promotes QED to the level of one of the most precise theories ever built to describe nature.

b) Quantum chromodynamics

As discussed earlier, mesons are $M \equiv q\bar{q}$ states, while baryons have three constituents, $B \equiv qqq$. However, in order to satisfy the Fermi-Dirac statistics[5], one needs to assume the existence of a new quantum number, *colour*, such that each species of quark may have $N_C = 3$ different colours: (red, green, blue).

There is no evidence of extra states with non-zero colour, thus to avoid this one needs to further postulate that all asymptotic states are colourless. This assumption is known as *quark confinement*: since quarks carry colour they are confined within colour-singlet bound states.

Experimentally the colour quantum number is tested through the measurement of the ratio [1]:

$$R_{e^+e^-} \equiv \frac{\sigma(e^+e^- \to hadrons)}{\sigma(e^+e^- \to \mu^+\mu^-)} \tag{1.2}$$

The production of hadrons occurs through $e^+e^- \to \gamma^*, Z^* \to q\bar{q} \to hadrons$. Since quarks are assumed to be confined, the probability to hadronize is just one. Therefore, one can estimate the inclusive cross-section into hadrons summing over all possible quarks in the final state. The electroweak production factors which are common with the $e^+e^- \to \gamma^*, Z^* \to \mu^+\mu^-$ process cancel in the ratio. At energies well below the Z peak, the cross-section is dominated by the γ-exchange amplitude and the ratio $R_{e^+e^-}$ is then given by the sum of the quark electric charges squared:

$$R_{e^+e^-} \approx N_C \sum_{f=1}^{N_f} Q_f^2 = \begin{cases} \dfrac{2}{3}N_C = 2, & (N_f = 3\ :\ u,d,s) \\ \dfrac{10}{9}N_C = \dfrac{10}{3}, & (N_f = 4\ :\ u,d,s,c) \\ \dfrac{11}{9}N_C = \dfrac{11}{3}, & (N_f = 5\ :\ u,d,s,c,b) \end{cases} \tag{1.3}$$

This formula involves an explicit sum over the N_f quark flavours multiplied by the number of different colour possibilities N_C, taken to be three. Notice that the top quark is not included, as its mass is larger than the Z mass. The measured ratio is shown in Figure 1.8. The simple rule in Equation 1.3 provides a good description of the observed behaviour of R over a broad range of energies. Thus it seems natural to

[5] Fermions obey a statistical rule described by Fermi, Dirac and Pauli called the "exclusion principle". No two fermions may be described by the same quantum numbers.

take colour as the charge associated with the strong forces and try to build a quantum field theory based on it. That theory is known as QCD.

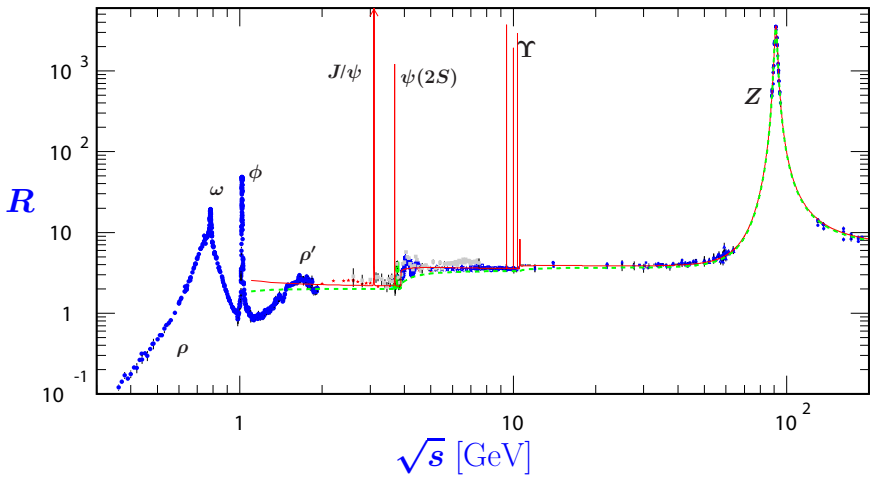

Figure 1.8: World data on the ratio $R_{e^+e^-}$ [7]. The broken lines show the naive quark model approximation with NC = 3. The solid curve is the 3-loop perturbative QCD prediction.

QCD is represented by the symmetry group $SU(3)_c$, the gauge group of the colour triplets, and the gluon is the associated gauge boson. The $SU(3)_C$ gauge symmetry forbids to add a mass term for the gluon fields because it is not invariant under the local transformation. Gluons are, therefore, massless spin-1 particles.

Properties of QCD

- All interactions are given in terms of a single universal coupling g_s, which is called the *strong coupling constant*, commonly defined as $\alpha_s = \frac{g_s^2}{4\pi}$. Experimentally, the value of the coupling constant is determined as $\alpha_s(M_Z^2) = 0.1185$ [3] at M_Z energy escale. Cubic (g_s^3) and quartic g_s^4 gluon self-interactions are allowed in QCD.

- The phenomenon known as *asymptotic freedom* implies that the strong force between quarks becomes weaker at short distances, but increases at large distances, a property known as the *quark confinement*.

- At high-energy collisions in a particle collider, "free" quarks or gluons might be created. Due to the colour confinement, these cannot exist individually. They combine with quarks and antiquarks spontaneously created from the vacuum to form hadrons. This process is called *hadronization*. The tight cone of particles created by the hadronization of a single quark is called a jet.

1.2.3 Electroweak unification

Weak interactions are distinguished from QED and QCD by some characteristic properties like lifetimes, strength of coupling, cross-sections, and violation of symmetries. These interactions are short-ranged, which requires massive messenger particles, seemingly inconsistent with gauge invariance. They come in two types, charged and neutral current interactions, which couple quarks and leptons differently. Charged current interactions, mediated by the $W^{\pm}$ bosons, only involve left-handed fermions and readily change flavour, as in the strange quark decay $s \to ue^{-}\bar{\nu}_e$. Neutral current interactions mediated by the Z boson, on the other hand, couple both left- and right-handed fermions, and flavour-changing neutral currents are strongly suppressed.

To describe electroweak interactions, one needs a more elaborate structure than QED or QCD Lagrangians. The EW theory is a "chiral" gauge theory[6], hence the building blocks are massless left- and right-handed fermions. The electroweak gauge group is a product of two groups, $G_{EW} \equiv SU(2)_L \otimes U(1)_Y$. The non-Abelian group $SU(2)_L$ is associated to the "weak isospin" quantum number and the $U(1_Y)$ charge is the weak hypercharge Y, which is related to the electric charge Q by

$$Q = I_3 + \frac{Y}{2} \tag{1.4}$$

where I_3 is the third component of the weak isospin. In the weak interactions only the left-handed components couple to the $SU(2)_L$ gauge field. This suggests to form doublets from quarks u_L and d_L, and leptons e_L and ν_L, keeping the right-handed fields as singlets. Hence $SU(2)_L$ multiplets can be represented as follows:

$$q_L = \begin{pmatrix} u_L \\ d_L \end{pmatrix}, \qquad u_R, \qquad d_R, \qquad l_L = \begin{pmatrix} \nu_L \\ e_L \end{pmatrix}, \qquad e_R, \tag{1.5}$$

where the right-handed neutrino is omitted because it is not part of the SM. The EW theory generates four gauge bosons which can be identified by the physical bosons W^+, W^-, Z and γ and establishes the following relation between the $SU(2)_L$ and $U(1)_Y$ couplings to the electromagnetic coupling:

$$g \sin\theta_W = g' \cos\theta_W = e, \tag{1.6}$$

where θ_W is the Weinberg or weak mixing angle, g and g' are the couplings constants of the charged and neutral currents, and e is the electromagnetic constant coupling. This relation provides the unification of the electroweak interactions. The mathematical formalism of the EW theory and its Lagrangian are presented in Appendix B.2.

The Lagrangian in Equation B.14 describes mathematically the interaction between fermions (quarks and leptons) and gauge bosons. It allows to deduce expressions for the fermion couplings to Z and γ bosons as a function of their charge and isospin quantum numbers. These expressions are shown in Table 1.1. Note that members of

[6] In quantum field theory, a chiral gauge theory is a quantum field theory with charged chiral fermions. The electroweak model breaks parity maximally, which means that the charged weak gauge bosons only couple to left-handed quarks and leptons while the neutral electroweak Z boson couples to both left- and right-handed fermions

Table 1.1: Neutral-current couplings of quarks and leptons to Z and γ bosons

Couplings	(u, c, t)	(d, s, b)	$(\nu_e, \nu_\mu, \nu_\tau)$	(e, μ, τ)
$2v_f$	$1 - \frac{8}{3}\sin^2\theta_W$	$-1 + \frac{4}{3}\sin^2\theta_W$	1	$-1 + 4\sin^2\theta_W$
$2a_f$	1	-1	1	-1

the same family have the same values of Q_f and I_3^f, for instance $Q_{(u,c,t)} = 2/3$ and $I_3^{(u,c,t)} = 1/2$. The top quark couplings to Z and γ are the main topic of this thesis. In Chapter 6 an analysis of the process $e^+e^- \to Z/\gamma \to t\bar{t}$ is presented, that allows the extraction of these electroweak couplings.

1.2.4 Spontaneous Symmetry Breaking

The physical Z and $W^\pm$ bosons have a non-zero mass, which is forbidden by the local gauge symmetry of the group G_{EW}. That incongruence is solved through Spontaneous Symmetry Breaking (SSB), a mechanism that generates masses for the gauge bosons and fermions without destroying gauge invariance. In the SM this mechanism is known as the *Higgs mechanism*. It allows to match the spontaneous symmetry breaking by vacuum with the massless Goldstone bosons[7]. The Higgs mechanism makes a clever use of local gauge symmetry, converting massless gauge bosons into massive ones and explains why the $W^\pm$ and Z bosons are massive. In a similar way, fermion masses are also generated. The mass of each particle will depend on how strong it interacts with the Higgs field. A mathematical formulation of the SSB and the Higgs mechanism is given in Appendix B.2.2.

1.2.5 Experimental particle masses

The SM does not predict the values of some of its parameters. These parameters and their values have to be established by experiment. Among these parameters one can find the masses of the leptons and quarks, the Higgs boson mass or the gauge couplings g, g_S, g'. Tables 1.2 and 1.3 list the measured values of the fundamental SM particles.

The SSB mechanism yields a precise prediction for the $W^\pm$ and Z masses, relating them to the vacuum expectation value v of the Higgs boson through the Eq. B.25. Thus, M_Z is predicted to be larger than M_W, in agreement with the measured masses in Table 1.2 [3].

From experiment, one obtains the electroweak mixing angle

$$\sin^2\theta_W = 1 - \frac{M_W^2}{M_Z^2} = 0.023. \tag{1.7}$$

One can estimate the Weinberg angle θ_W from the muon decay $\mu^- \to e^-\bar{\nu}_e\nu_\mu$. Due

[7] Goldstone bosons are spin-0 bosons that appear necessarily in models exhibiting spontaneous breakdown of continuous symmetries.

Table 1.2: Experimental mass and charge of the gauge bosons. Values taken from *Review of Particle Physics*, Particle Data Group [3].

Bosons	γ	*gluon*	W	Z	H
Mass[GeV]	$< 10^{-27}$	0	80.385 ± 0.015	91.1876 ± 0.0021	125.09 ± 0.24
Q[e]	$< 10^{-35}$	0	± 1	0	0

to the large mass of the W propagator, the decay can be well approximated through a local four-fermion interaction, i.e.,

$$\frac{4\pi\alpha}{\sin^2\theta_W M_W^2} = 4\sqrt{2}G_F \tag{1.8}$$

where G_F is the Fermi coupling constant. The most precise determination of its value is provided by the measured muon lifetime from [8]

$$G_F = (1.166\ 378\ 8 \pm 0.000\ 000\ 7) \cdot 10^{-6}\ \text{GeV}^{-2} \tag{1.9}$$

Therefore the precisely measured values of the QED coupling constant α, M_W and G_F imply

$$\sin^2\theta_W = 0.215, \tag{1.10}$$

in rough agreement with the value obtained from the Z and W masses. The difference is explained by higher order corrections, as explained in next Section 1.2.6. Additionally, the Fermi constant gives a direct determination of the electroweak scale, i.e., the scalar vacuum expectation value:

$$v = \left(\sqrt{2}G_F\right)^{-1/2} = 246\text{GeV} \tag{1.11}$$

The experimental limit on the photon mass is totally compatible with the predicted massless boson by the SM. Also the gluon is theoretically massless, however a mass as large as a few MeV cannot be excluded. The experimental mass of the Higgs boson comes from the combined fit of the ATLAS and CMS experiments data at 7-8 TeV collisions at the LHC [9].

Unlike the leptons, quarks are confined inside hadrons and are not observed as physical particles. Quark masses therefore can not be measured directly, but must be determined indirectly through their influence on hadronic properties. Table 1.3 (a) shows experimental values for the quark masses. Any quantitative statement about the value of a quark mass must make careful reference to the particular theoretical framework that is used to define it. Thus it is important to keep this scheme dependence in mind. The most commonly used renormalization scheme for QCD perturbation theory is the modified minimal subtraction, or $\overline{\text{MS}}$, scheme [11].

It is a well-known experimental fact that the neutrinos and antineutrinos are of three light varieties or flavours: $(\nu_e, \nu_\mu, \nu_\tau)$. The SM describes them as left-handed massless fields. However, experiments with solar, atmospheric, reactor and accelerator

Table 1.3: Experimental mass and charge of the elementary fermions. The u, d and s-quark masses are estimates of so-called "current-quark masses", in a mass-independent subtraction scheme such as $\overline{\text{MS}}$. The c and b-quark masses are the "running" masses in the $\overline{\text{MS}}$ scheme. For the b-quark the 1S mass is also quoted. Finally the t-quark mass is the pole mass from the world combination of Tevatron and LHC measurements [10].

(a)

Quarks	Mass [GeV]	Q[e]
u	$(2.3\ ^{+0.7}_{-0.5}) \cdot 10^{-3}$	2/3
d	$(4.8\ ^{+0.5}_{-0.3}) \cdot 10^{-3}$	-1/3
s	$(95 \pm 5) \cdot 10^{-3}$	-1/3
c	1.275 ± 0.025	2/3
b	$\overline{\text{MS}} : 4.18 \pm 0.03$ $1\text{S} : 4.66 \pm 0.03$	-1/3
t	$173.34 \pm 0.27 \pm 0.71$	2/3

(b)

Leptons	Mass [MeV]	Q[e]
e	0.510998928 ± 0.000000011	-1
ν_e	$2 \cdot 10^{-6}$	0
μ	105.6583715 ± 0.0000035	-1
ν_μ	< 0.19	0
τ	1776.86 ± 0.12	-1
ν_τ	$< 18.2 \pm 0.48$	0

neutrinos have provided compelling evidence for the existence of neutrino oscillations, transitions in flight between the different flavour neutrinos, only explicable by non-zero neutrino masses and neutrino mixing. There are ways to incorporate small non-zero neutrino masses (and lepton-flavor violation) through a lepton mixing matrix. For instance, if sterile ν_R fields are included in the model, one has an additional Yukawa term in equation B.28, giving rise to a neutrino mass matrix $m_\nu = \lambda_\nu \frac{v}{\sqrt{2}}$.

1.2.6 QED and QCD corrections

The increasing precision of experimental data in elementary particle physics requires an equally precise theoretical description. Quantum field theories are solved using perturbative expansions. In QED, for instance, any observable can be written as:

$$O = O_0 + \alpha O_1 + \alpha^2 O_2 + \alpha^3 O_3 + ..., \tag{1.12}$$

where O_0 corresponds to the observable at tree level and $\alpha^n O_n$ (with $n > 0$) denotes the n^{th}-order correction to the observable. Therefore, corrections described by one- and multi-loop Feynman diagrams have to be considered. They got the name of radiative corrections, since in QED they correspond to the emission and absorption of photons. One-loop Feynman diagrams of QED are shown in Figure 1.9.

The first order of QCD corrections are commonly named as next-to-leading-order (NLO) and higher-order corrections as N^{n}LO, with n being the number of loops considered in Feynman diagrams.

In calculations in QED and QCD one finds two problems, the ultraviolet and the infrared divergences. One can get rid of these divergences and obtain finite corrections to the cross-sections of elementary processes using a technique called renormalisation.

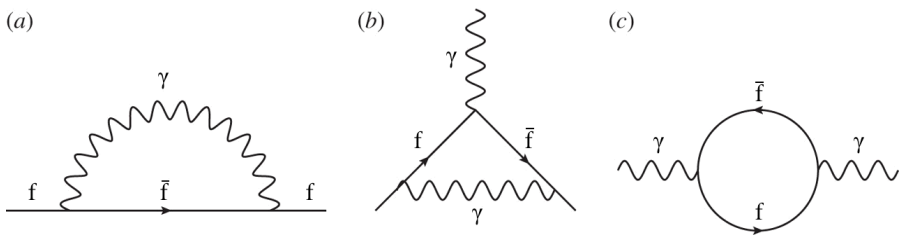

Figure 1.9: Divergent first-order loops of QED

The infinite terms can be reabsorbed within the constants of the theory. For example, in QED divergences are reabsorbed within α and m_e:

$$\alpha(Q^2) = \alpha_0 \left[1 + \frac{\alpha_0}{3\pi} f\left(\frac{Q^2}{m_e^2}\right) + O(\alpha_0^2)\right], \tag{1.13}$$

where α_0 is the "primary" constant appearing in the Lagrangian and $\alpha(Q^2)$ the "renormalized" value that should merge with the measured value. The function $f(Q^2/m_e^2)$ is the finite correction which causes the coupling to run with the energy scale Q^2. The resulting QED running coupling $\alpha(Q^2)$ decreases at large distances (decreasing Q^2). This can be intuitively understood as the charge screening generated by the virtual fermion pairs, shown in Figure 1.9 (c). It turns out that the effect is really small and can safely be ignored at atomic or nuclear scales. Nevertheless, it gives rise to a significant difference between the constant evaluated at electron and Z mass scales [3]

$$\alpha(m_e^2)^{-1} = 137.035\ 999\ 074 \pm 0.000\ 000\ 032 \quad > \quad \alpha(M_Z^2)^{-1} = 128.95 \pm 0.05 \tag{1.14}$$

For $Q^2 >> m_e^2$ the correction function can be approximated to $f(Q^2/m_e^2) \approx \ln(Q^2/m_e^2)$ [8].

$$\alpha(Q^2) = \frac{\alpha_0}{1 + \beta_0 \alpha_0 \ln(Q^2/m_e^2)} \quad \text{with} \quad \beta_0 = \frac{-1}{3\pi} \tag{1.15}$$

This result is not exact, and is known as the leading log (LL) approximation. Additionally, there are corrections that imply more complicated propagator diagrams like multi-photon exchange between loops, not discussed here.

To calculate the propagator loop correction in QCD, one does not only have to consider quark loops such as these in left diagram of Figure 1.10, like electron loops in QED, but also gluon loops shown in right diagram of Figure 1.10. The quark loop gives rise to a positive contribution to the β function (screening) while the gluon loop contribution is negative (anti-screening).

Since the reference scale $Q^2 = 0$ cannot be used in QCD, one has to specify an input value $Q^2(\mu^2)$ at some arbitrary reference scale μ^2. It is known as the renormalisation

[8] $1 + X + X^+X^3 + ... = \frac{1}{1+X}$

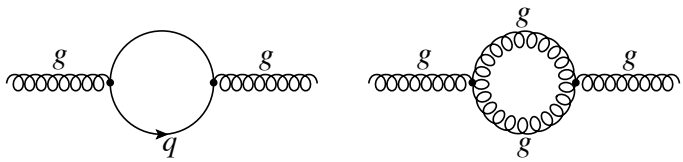

Figure 1.10: QCD first-order loops.

scale. Hence, analogously to QED, the formula for the one-loop running coupling constant in QCD is

$$\alpha_s(Q^2) = \frac{\alpha_s(\mu^2)}{1 + \beta_0 \alpha_s(\mu^2) \ln(Q^2/\mu^2)} \quad \text{with} \quad \beta_0 = \frac{11N_c - 2N_f}{2\pi}, \tag{1.16}$$

where N_c is the number of colours (3) and N_f is the number of flavours (6 in the SM). The expression for the running coupling constant can be simplified when we define the QCD scale parameter Λ as follows:

$$\alpha_s(Q^2) = \frac{1}{\beta_0 \ln(Q^2/\Lambda^2)} \tag{1.17}$$

For $Q^2 = M_Z^2$, the value of α_s is of the order of 0.12. At this energy only five quarks can be excited inside the loops. This value implies that $\Lambda \approx 200$ MeV. Figure 1.11 shows how the strong coupling constant α_s decreases with the energy scale Q.

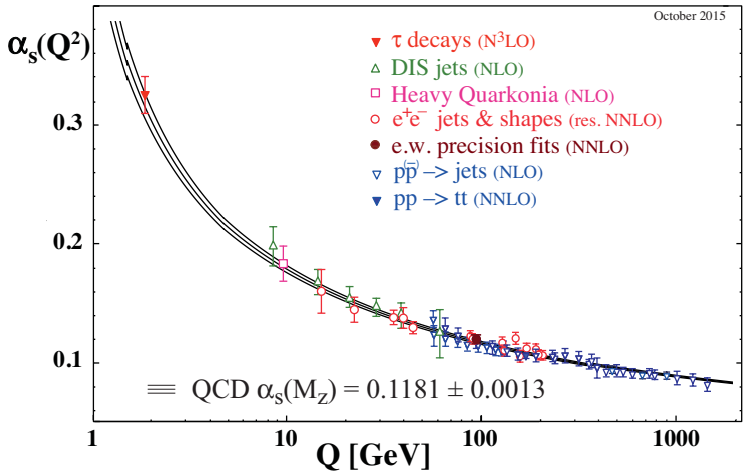

Figure 1.11: Summary of measurements of α_s as a function of the energy scale Q [3]. The respective degree of QCD perturbation theory used in the extraction of α_s is indicated in brackets (NLO: next-to-leading order; NNLO: next-to-next-to leading order; res. NNLO: NNLO matched with resumed next-to-leading logs; N^{3}LO: next-to-NNLO)

1.2.7 $\mathcal{CP}$ violation

While parity and charge conjugation are violated by the weak interactions in a maximal way, the product of the two discrete transformations is still a good symmetry of the gauge interactions. In fact, $\mathcal{CP}$ appears to be a symmetry of nearly all observed phenomena. However, a slight violation of the $\mathcal{CP}$ symmetry at the level of 0.2% is observed in the neutral kaon system and more sizable signals of $\mathcal{CP}$ violation have been recently established at the B factories [12].

Direct $\mathcal{CP}$ violation is allowed in the Standard Model if a complex phase appears in the Cabibbo-Kobayashi-Maskawa (CKM) matrix describing quark mixing. The CKM matrix couples any 'up-type' quark with all 'down-type' quarks. The 'standard' CKM parametrization is:

$$V = \begin{pmatrix} V_{ud} & V_{us} & V_{ub} \\ V_{cd} & V_{cs} & V_{cb} \\ V_{td} & V_{ts} & V_{tb} \end{pmatrix}$$

It is described by three angles and one phase

$$V = \begin{bmatrix} c_{12}c_{13} & s_{12}c_{13} & s_{13}e^{-i\delta_{13}} \\ -s_{12}c_{23} - c_{12}s_{23}s_{13}e^{i\delta_{13}} & c_{12}c_{23} - s_{12}s_{23}s_{13}e^{i\delta_{13}} & s_{23}c_{13} \\ s_{12}s_{23} - c_{12}c_{23}s_{13}e^{i\delta_{13}} & -c_{12}s_{23} - s_{12}c_{23}s_{13}e^{i\delta_{13}} & c_{23}c_{13} \end{bmatrix}, \quad (1.18)$$

where $c_{ij} \equiv \cos\theta_{ij}$ and $s_{ij} \equiv \sin\theta_{ij}$, with i and j the number of the quark generation $(i, j = 1, 2, 3)$.

A necessary condition for the appearance of the complex phase δ_{13} is the presence of at least three generations of quarks. In fact, it was for this reason that the third generation was assumed to exist, before the discovery of the b and the τ. With only two generations, the SM could not explain the observed $\mathcal{CP}$ violation in the K system ($\sim 2 \times 10^{-3}$). In that system, $\mathcal{CP}$ violation effects can only appear at the one-loop level, where the top quark is present.

$\mathcal{CP}$ violation has not been observed in the top quark sector. Precision measurements lead us to predict very small effects in the SM, but extensions could lead to non-negligible effects. Future e^+e^- colliders have the potential to measure that phenomenon through the study of the $t\bar{t}$ production process. In the Chapter 6, sensitive observables to $\mathcal{CP}$ violation effects in top quark decays are investigated in the ILC and CLIC environments.

1.3 The Top Quark

This section is dedicated exclusively to the *top* quark, the particle that is the focus of this thesis. The top quark was discovered at the CDF and D∅ experiments at the Tevatron. Apart from the top quark mass and the CKM matrix elements, the SM predicts all properties of top quarks and their decays with high precision. Since the top quark lifetime is much shorter than the time required for hadronization, top quark properties can be measured directly and usually with much less uncertainty than

those for other quarks, where these characteristics are derived from their bound states. Differences between measured properties and the precisely known SM predictions offer sensitive tests for new physics beyond the SM.

1.3.1 Top quark properties

The top quark is the heaviest known elementary particle, even heavier than the Higgs boson. Its large mass is the reason for its very short lifetime. In the SM the top quark has the same quantum numbers and interactions as all other up-type quarks. It is the weak isospin partner of the b quark with spin 1/2 and electric charge $Q_t = +2/3$. The left-handed top quark is the upper component of the weak isospin doublet and the right-handed component is a weak isospin singlet. It is a colour triplet with respect to the $SU(3)_C$ gauge group. From the theory side, the top quark is absolutely needed to ensure cancellation of the chiral anomaly in the SM and therefore to ensure its consistency as a quantum field theory. An accurate knowledge of its properties (mass, couplings, production cross section, decay branching ratios, etc.) can bring key information on fundamental interactions at the electroweak breaking scale and beyond.

Top quark mass and lifetime

Measurements of the top quark mass, m_t, using kinematic properties of the decay products of the top quark, i.e., using direct approaches, have been performed by the ATLAS, CDF, CMS, and DØ Collaborations using a variety of experimental techniques. The first world combination of m_t measurements was performed in 2014 [10] and taking into account the correlations between the colliders, experiments, and analysis channels for all sources of systematic uncertainty considered. The combined value is $m_t = 173.34 \pm 0.27(stat) \pm 0.71(syst)$ GeV, which corresponds to a relative uncertainty of 0.44%. The latest results from averaged 7-8 TeV data at CMS get even a more precise measurement ∼0.5 GeV [13]. Expectations range from a pessimistic 500 MeV after the complete LHC program to 200 MeV. These prospects do not include the uncertainty in the interpretation of the direct mass measurement as the pole mass [14]. On the other hand the most precise measurement of the top quark pole mass to date, with data collected by ATLAS at 7 TeV and luminosity of 4.6 fb^{-1}, is found in Reference [15]. They show that the normalized differential cross section of the $t\bar{t} + 1jet$ system as a function of its invariant mass can be used for a precise measurement of the top quark mass using the pole-mass scheme at NLO theoretical accuracy in QCD.

The lifetime τ and the related resonance width $\Gamma = 1/\tau$ are primary characteristics of any particle. A small value of the top lifetime τ_t is expected due to its large mass and the large value of V_{tb}. The width of the top quark is computed in the SM to be 1.32 GeV with about 1% uncertainty [16] which translates into a top quark lifetime of ($\tau_t \approx 5 \times 10^{-25} s$) that is much smaller than the typical time for formation of QCD bound state hadrons ($\tau_{QCD} \approx 1/\Lambda_{QCD} \approx 3 \times 10^{-24} s$). Therefore hadrons containing a top quark are not expected to exist. It is impossible to measure such a short lifetime directly by measuring the distance between creation and decay. An alternative approach used for strongly interacting decays is the measurement of the

width. The most precise measurement of the top quark width was obtained by CMS [17] using the indirect method proposed by DØ experiment [18], $\Gamma_t = 1.36 \pm 0.02$ (stat) $^{+0.14}_{-0.11}$ (syst) GeV, in good agreement with the SM prediction.

V_{tb} element of CKM matrix and top quark decay

The matrix element V_{tb} is close to unity while the elements V_{td} and V_{ts} are very small ($|V_{td}| = (8.4 \pm 0.6) \times 10^{-3}, |V_{ts}| = (40.0 \pm 2.7) \times 10^{-3}$ [3]). A global fit in the SM gives $|V_{tb}| = 0.999146\ ^{+0.000021}_{-0.000046}$ [3]. Any experimental deviation from this value will be evidence for new BSM physics. The large mass and the small mixing of the top quark cause the top quark to decay to a W boson and b quark with a probability close to 100%. Feynman diagrams of the top and anti top quark decays are shown in Figure 1.12.

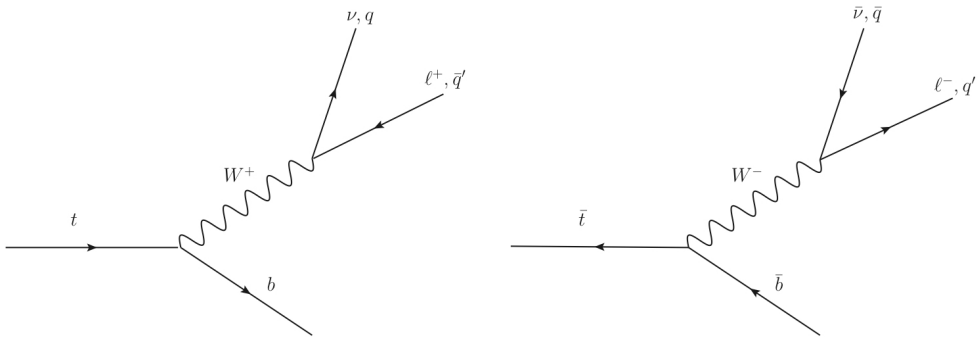

(a) $t \to W^+ b$ (b) $t \to W^+ b$

Figure 1.12: Top and anti-top quark decay.

Since the top quark decays to a W boson and a b quark, the final state is determined by the way that the W boson decays. The W boson can decay into a lepton plus its associated neutrino or in a light quark pair. Hence $t\bar{t}$ pair decays can be classified according to the decays of the two W coming from these tops. If both W bosons decay to a lepton plus a neutrino, the final state has two leptons, two b-jets and missing transverse energy (E_T) carried by the two neutrinos (*dileptonic channel*). If one W decays to a lepton and the other to quark pairs (*semi-leptonic channel or "lepton+jets"*), the final state is one lepton, four quarks (of which two are b-quarks) and a neutrino. If both W bosons decay to quarks (*fully-hadronic channel*), the final state has six quark jets. The three final states correspond to 10.5%, 43.8% and 45.7% of $t\bar{t}$ events, respectively.

Top quark electroweak couplings

At the LHC, significant progress has been achieved in the study of the processes $p\bar{p} \to t\bar{t}\gamma$, $t\bar{t}Z$, and $t\bar{t}W$, which together with $t\bar{t}H$ associated production, will provide

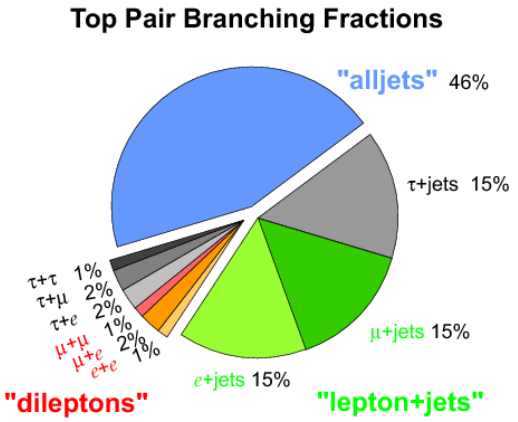

Figure 1.13: $t\bar{t}$ pair branching fractions.

further information on the top-quark electroweak couplings. The prospects study presented by [19] is an analysis at leading order QCD. The analysis carried out in [20] suggests that higher-order effects in the theory may allow for an improvement of the LHC precision by up to 40% the precision. Electroweak couplings are measured also in single t quark production. In the effective field theory approach, assuming $SU(2)_L \times U(1)_Y$ gauge symmetry for the operators, the relation

$$\frac{\delta g_L^{tbW}}{g_L^{tbW}} \approx 0.35 \frac{\delta g_L^Z}{g_L^Z} \tag{1.19}$$

can be established. Here g_L^{tbW} is the charged current coupling of the decay $t \to Wb$.

The CMS Collaboration [21] reports a precision for the t-b transition probability V_{tb} of about 4%. In the Standard Model V_{tb} is identical to g_L^{tbW}. Hence, by means of Eq. 1.19 the coupling of left-handed t quarks to the Z boson can be derived to a precision of order 11%. Noting that $\sigma(pp \to \bar{t}tZ) \propto (g_L^Z)^2 + (g_R^Z)^2$ this allows in principle also for deriving $(g_R^Z)^2$, albeit with a poor precision given that $(g_L^Z)^2 \gg (g_R^Z)^2$. Loop corrections in heavy flavour physics as e.g. in the processes $b \to s\gamma$, $B \to \mu^+\mu^-$ or $K \to \mu^+\mu^-$, respectively, may also lead to competitive determinations of δg_L^Z [22]. However, again g_R^Z can only be constrained rather poorly.

In e^+e^- colliders with $\sqrt{s} > 2m_t$ top quark pairs are produced in $e^+e^- \to Z\gamma \to t\bar{t}$, giving direct access to the EW couplings. Note at this point that the interference between the γ and the Z in case of $e^+e^- \to t\bar{t}$ will allow for measuring the sign of the form factors that will be unnoticed in associated $\bar{t}tZ$ at the LHC.

In Chapter 6 the potential measurements of the top quark couplings to the electroweak gauge bosons Z and γ at e^+e^- colliders, as a probe for BSM physics, are explored.

1.3.2 Top quark production at hadron colliders

Two classes of top quark production exist at hadron colliders. The first proceeds by the strong QCD force in which a quark and anti-quark or a pair of gluons interact to produce a top and anti-top quark. Feynman diagrams of these processes are shown in Figures 1.14 (a) and (b). The top pair production can be also take place through the electroweak process $q\bar{q} \to Z/\gamma \to t\bar{t}$, but with a very small cross section. Approximately 85% of the production cross section at the Tevatron is from $q\bar{q}$ annihilation, with the remainder from gluon-gluon fusion, while at LHC energies about 90% of the production is from the latter process at $\sqrt{s} = 14$ TeV ($\approx 80\%$ at $\sqrt{s} = 7$ TeV).

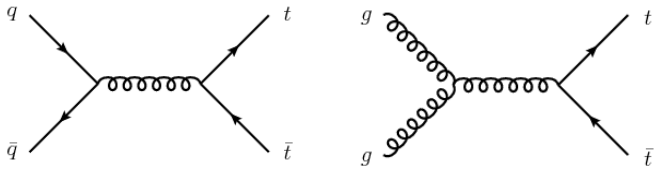

(a) $q\bar{q} \to g \to t\bar{t}$ (b) $gg \to g \to t\bar{t}$

Figure 1.14: Feynman diagrams of the $t\bar{t}$ pair production at tree level via $q\bar{q}$ (a) and gg fusion (b).

The combination of CDF and DØ results [23] yields $\sigma_{t\bar{t}} = 7.60 \pm 0.41$ pb, in good agreement with the NNLO theoretical prediction [24] of 7.16 pb. Recent DØ updates of the l+jets and di-lepton channel cross sections using the full 9.7 fb^{-1} of data are combined to give $\sigma_{t\bar{t}} = 7.73 \pm 0.56$ pb [25]. The individual ATLAS and CMS inclusive cross measurements at $\sqrt{s} = 8$ TeV and their combination [26], $\sigma_{t\bar{t}} = 241.5 \pm 8.5$ pb are also in good agreement with the NNLO prediction [24] of 245.8 pb. These results and their NNLO+NNLL predictions are shown in the left plot of Figure 1.16.

The second class of processes proceeds through the weak interaction with a W boson propagator, leading to a single top quark in the final state, associated with at least one other jet. Electroweak single top-quark production mechanisms, namely from $q\bar{q} \to W* \to t\bar{b}$, $qb \to \bar{q}t$, mediated by virtual s-channel and t-channel W-bosons, and Wt-associated production, through ($bg \to W^-t$), lead to somewhat smaller cross sections. Feynman diagrams of these processes are shown in Figure 1.15.

The dominant production at the Tevatron is through s-channel and t-channel W-boson exchange. Associated production with a W-boson (Wt production) has a cross section that is too small to observe at the Tevatron. The CDF and DØ experiments combined their measurements of the s-channel production for maximum precision with a resulting cross section of $\sigma_s = 1.29\ ^{+0.26}_{-0.24}$ pb [27]. In the same time, they also present the $s+t$ combined cross section measurement resulting in $\sigma_{s+t} = 3.30\ ^{+0.52}_{-0.40}$ pb.

At the LHC, the t-channel cross section is expected to be more than three times as large as s-channel and Wt production, combined. Both ATLAS and CMS have measured single top at 7 TeV and 8 TeV. The measured t-channel cross-section at 7 TeV is $\sigma_t = 67.2 \pm 6.1$ pb, and they find $\sigma_t = 82.6 \pm 1.2(stat.) \pm 11.4(syst.)$ pb at 8 TeV

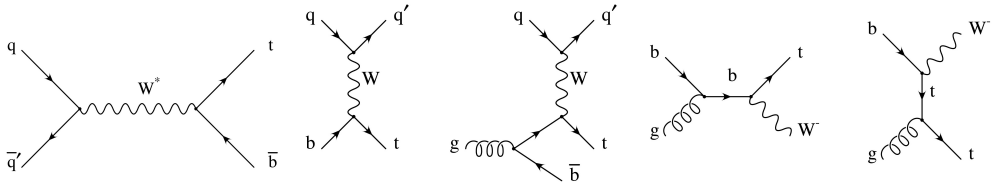

(a) s-channel (b) t-channel (c) W-associated production

Figure 1.15: Feynman diagrams for the electroweak production of single top quarks.

[28]. Additionally both, ATLAS and CMS, also provide evidence for the associate Wt production at 7 TeV, resulting in $\sigma_{Wt} = 16.8 \pm 2.9(stat.) \pm 4.9(syst.)$ pb [29]. In the right plot of Figure 1.16 these measurements are compared to the NNLO predictions.

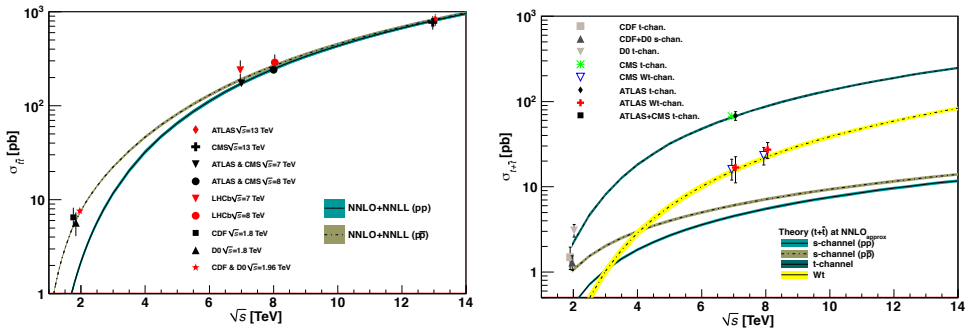

Figure 1.16: Measured and predicted $t\bar{t}$ and single top production cross sections from Tevatron energies in $p\bar{p}$ collisions to LHC energies in pp collisions [3]. Tevatron data points are at $\sqrt{s}$= 1.96 TeV and LHC data points at $\sqrt{s}$= 7 TeV, $\sqrt{s}$= 8 TeV and $\sqrt{s}$= 13 TeV.

Thanks to the large statistics now available at the LHC, both CMS and ATLAS experiments also performed differential cross-section measurements in single-top t-channel production. Such measurements are extremely useful as they test our understanding of both QCD and EW top quark interactions.

1.3.3 Top quark production at e^+e^- colliders

Due to its large mass, the top quark is the only quark so far not studied in electron-positron annihilation. LEP, the last operative e^+e^- collider, achieved a maximum c.o.m. energy of 209 GeV, not enough to create top quarks.

The tree level diagram of the electroweak $t\bar{t}$ production via exchange of Z/γ bosons at the e^+e^- colliders is presented in Figure 1.17 (a). The cross section for this process for a range of center-of-mass energies is in Figure 1.18. Single top quark production through the process $e^+e^- \to tWb$ can also occur, giving rise to the same six-fermion final state. One of the diagrams contributing to the single top process is presented

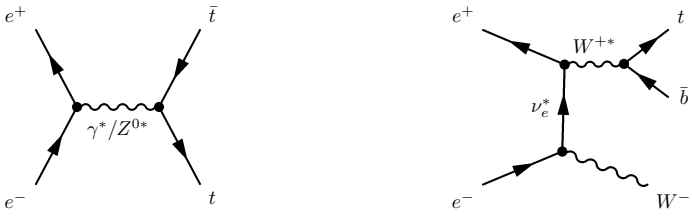

(a) $t\bar{t}$ pair production (b) Single t quark production

Figure 1.17: Diagrams of the $t\bar{t}$ and single top production at e^+e^- colliders: (a) Tree level $t\bar{t}$ pair production, (b) single t quark production.

in Figure 1.17 (b). The single top quark production process is the most important source of contamination to $t\bar{t}$ processes. Both processes are entangled by interference between different diagrams and are indistinguishable experimentally at $\sqrt{s} = 500$ GeV as pointed out in Reference [30].

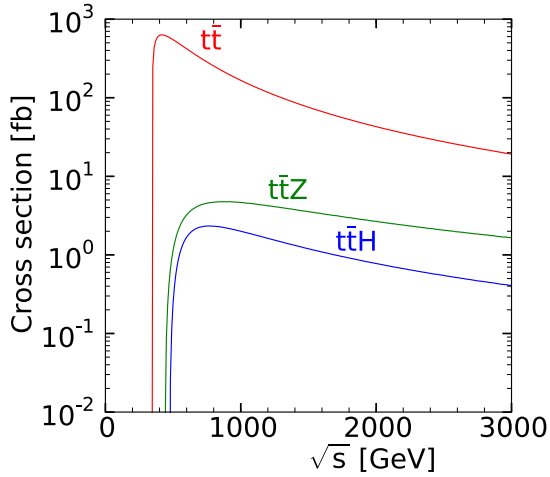

Figure 1.18: The cross section as a function of the center-of-mass energy of lepton colliders. The three curves correspond to top quark pair production (the upper, red curve) and to associated production of a top quark pair with a Z-boson (the central, green curve) or a Higgs boson (the lowest, blue curve)

The top quark pair production threshold at electron-positron colliders has been identified as a key element in the program of high-energy lepton colliders. A precise measurement of the shape of the sharp rise of the cross-section around $\sqrt{s} = 2m_t$ can provide competitive measurements of the top mass, the Yukawa coupling or the coupling constant α_s [31]. Precision tests of the top electroweak couplings to Z and γ can be performed at energies above the top pair production threshold, as is discussed in Chapter 6. Furthermore, e^+e^- colliders, running at the TeV energy scale, give

access to the $t\bar{t}Z$ and $t\bar{t}H$ associated production processes. It allows to extract the top Yukawa coupling and explore the Higgs $\mathcal{CP}$ properties, as well as to look for contributions from "new physics" at high scale. The cross section of the $t\bar{t}$ production together with the associated productions to Z and H are plotted in Figure 1.18 as a function of the center-of-mass energy.

1.3.4 A window to new physics

The top quark, as the weak isospin partner of the b-quark, plays an important role in the SM and in its predictions for experiments. Its mass is a key parameter providing, together with the Higgs mass, constraints on the stability limit of the Standard Model. The result is shown in Figure 1.19. The area defined by the current measured values and uncertainties of $\alpha_s(MZ)$, m_t and M_h is located in the metastability region, but close to the boundary with the stability region. However, the lifetime of such a metastable vacuum is estimated to be much larger than the current age of the Universe.

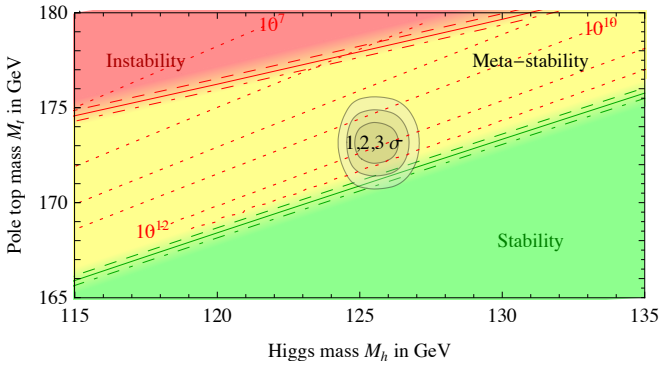

Figure 1.19: Regions of stability, meta-stability and instability of the SM vacuum in the $m_t - M_h$ plane close to the experimentally allowed range of M_h and m_t at 1, 2, and 3σ.

The exclusion of the SM as a valid quantum theory up to the Planck scale is only at the 2 sigma level with today's measured top quark and Higgs boson masses, so one can not fully reject the hypothesis that the SM works all the way up to the Planck scale. Clearly, a better precision of the top quark mass is needed as may be achieved at the LHC, but certainly at future e^+e^- colliders.

The top quark plays a central role in many Beyond Standard Model (BSM) scenarios. This suggests the use of signatures in the production of pairs or single top quarks to search for signals of such BSM scenarios.

In seeking extensions to the SM, most new models invoke large couplings between the new particles and the top quark. Thus we have the prospect of finding new particles such as heavy Z bosons or vector-like quarks whose decays contain top quarks, or particles such as charged Higgs bosons that could appear in the top decays. In

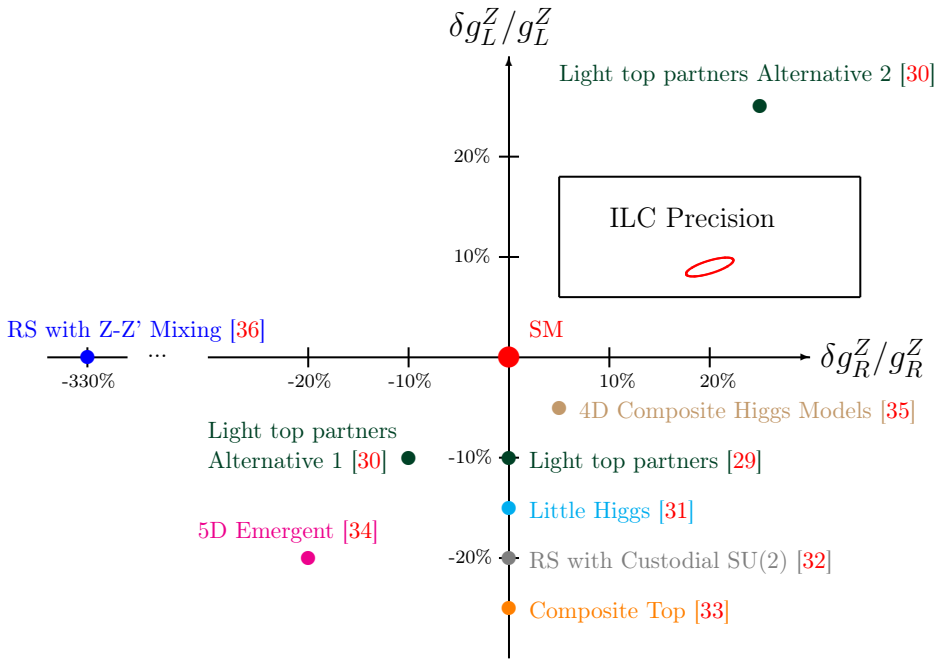

Figure 1.20: Predictions of several models that incorporate Randall-Sundrum (RS) models and/or compositeness or Little Higgs models on the deviations of the left- and right-handed couplings of the t quark to the Z^0 boson. The ellipse in the frame in the upper right corner indicates the precision that can be expected for the ILC running at a centre-of-mass energy of $\sqrt{s} = 500$ GeV after having accumulated $\mathcal{L} = 500\,\mathrm{fb}^{-1}$ of integrated luminosity shared equally between the beam polarisations $P(e^-)$, $P(e^+) = \pm 0.8, \mp 0.3$. The original version of this figure can be found in [32].

supersymmetric models, the need for cancellation of the large loop contributions arising from the large top quark mass suggests that the companion top squarks should have a lower mass than other sparticle masses, thus making them prime candidates for a first sighting of supersymmetry.

The expected high precision measurements at a linear e^+e^- collider allows for a profound exploration of effects by new physics. The findings from [33] can be confronted with predictions in the framework of Randall-Sundrum models and/or compositeness models such as [34, 35, 36, 37, 38, 39, 40, 41] or Little Higgs models as e.g. [42]. All these models entail deviations from the Standard Model values of the top quark couplings to the Z boson that will be measurable at the ILC as illustrated in Figure 1.20. Therefore, the electroweak couplings of the top quark to the Z and γ bosons are of special interest in the search of new physics.

Chapter 2

Future Linear Colliders

The discovery of a Higgs boson at the LHC was a big step in our understanding of the fundamental interactions of nature and the structure of matter described by the Standard Model. In order to establish the mechanism of electroweak symmetry breaking, all Higgs boson properties (mass, couplings, width, spin) must be precisely measured. The LHC has excellent prospects for the future runs 2 and 3 where proton-proton beams collide with an energy of $\sqrt{s}$ =13 TeV since May 2015. In the following decade the LHC will run with a high luminosity upgrade, the HL-LHC [43]. Despite that, e^+e^- colliders are needed to definitively test the electroweak theory with an unprecedented precision. A high-energy lepton collider also offers a very interesting top physics programme. In Chapter 6, the potential of e^+e^- colliders for the extraction of top quark electroweak couplings is compared to the precision achievable at LHC.

High-energy e^+e^- colliders have already been essential instruments in the past to search for the fundamental constituents of matter and to study their interactions. Today, the most advanced design for a future collider is the International Linear Collider (ILC) that is set up for a centre-of-mass energy range of $\sqrt{s}$ = 250 - 500 GeV (extendable to 1 TeV) [44]. A second proposal, somewhat less advanced and more challenging than ILC, is the Compact Linear Collider (CLIC), a multi–TeV linear e^+e^- collider. It is based on a two-beam acceleration technique that would provide high-luminosity e^+e^- collisions covering a centre-of-mass energy range from 380 GeV to 3 TeV [45]. In the following sections the acceleration techniques, the detector systems and the energy stages of ILC and CLIC colliders are discussed.

2.1 The physics case for lepton colliders

ILC and CLIC offer many opportunities for measurements that will address the most important current problems of particle physics. These colliders would provide unique views of the Higgs boson, the top quark, and possible new particles relevant to the mysteries of the matter content of the universe through measurements of very high precision. ILC and CLIC are thus essential tools that will advance our understanding of the basic laws of nature.

Table 2.1: Standard Model and Beyond Standard Model processes to be studied by the ILC at different energies [48].

Energy	Reaction	Physics Goal
91 GeV	$e^+e^- \to Z$	ultra-precision electroweak
160 GeV	$e^+e^- \to WW$	ultra-precision W mass
250 GeV	$e^+e^- \to Zh$	precision Higgs couplings
350–400 GeV	$e^+e^- \to t\bar{t}$	top quark mass and couplings
	$e^+e^- \to WW$	precision W couplings
	$e^+e^- \to \nu\bar{\nu}h$	precision Higgs couplings
500 GeV	$e^+e^- \to f\bar{f}$	precision search for Z'
	$e^+e^- \to t\bar{t}h$	Higgs coupling to top
	$e^+e^- \to Zhh$	Higgs self-coupling
	$e^+e^- \to \tilde{\chi}\tilde{\chi}$	search for supersymmetry
	$e^+e^- \to AH, H^+H^-$	search for extended Higgs states
700–1000 GeV	$e^+e^- \to \nu\bar{\nu}hh$	Higgs self-coupling
	$e^+e^- \to \nu\bar{\nu}VV$	composite Higgs sector
	$e^+e^- \to \nu\bar{\nu}t\bar{t}$	composite Higgs and top
	$e^+e^- \to \tilde{t}\tilde{t}^*$	search for supersymmetry

After the discovery of a Higgs boson with a mass around 125 GeV [46, 47], it's known that a c.o.m. of 250 GeV is enough to produce a Higgs boson in association with a Z boson (Higgsstrahlung). This is therefore a good energy to carry out accurate model-independent measurements of the Higgs couplings to fermions and bosons. The 500 GeV run is more sensitive to gauge boson fusion production and $t\bar{t}H$ production. Together, the two runs provide precision for all Higgs couplings. The first stage of CLIC, proposed to be at 380 GeV, gives simultaneous access to Higgs measurements through the Higgsstrahlung and WW-fusion production processes.

Within the top quark studies, the top mass can be measured with a precision of tens of MeV through a threshold scan of the top-antitop pair production around 350 GeV. Precision top quark couplings studies are best performed between 400 - 500 GeV. The low-energy stage of CLIC also focuses on precision top physics, including a ∼15% of the running time dedicated to the threshold scan of top pair production [45].

Table 2.1 gives some examples measurements that can be performed at the center-of-mass energies accessible to a linear collider. The highest-energy point shows the capability to follow up on discoveries at the LHC.

The highest energy stages of CLIC (1.5 TeV and 3 TeV) open the energy frontier, allowing for the discovery of new physics phenomena, while also giving access to additional Higgs and top properties such as the top-Yukawa coupling, the Higgs self-coupling and rare Higgs branching ratios. The ultimate CLIC energy stage of 3 TeV further enlarges the CLIC physics potential. It will give access to the discovery and accurate measurements of pair-produced particles with a mass up to 1.5 TeV or single

particles up to 3 TeV. In this context new electroweak particles or dark matter candidates are of special interest, as they may escape detection at the LHC. Moreover, the 3 TeV stage completes the full CLIC potential for precision SM physics, providing indirect sensitivity to BSM physics through precision measurements, where, for instance, Z' and Higgs compositeness models can be probed up to scales of approximately 20 TeV and 70 TeV, respectively.

Through the combination of direct searches and precision measurements, ILC and CLIC can not only produce discoveries, but will also enable sharper and more informative analysis of new particles discovered at the LHC.

2.2 The International Linear Collider (ILC)

The International Linear Collider is a 31 km-long high-luminosity linear electron-positron collider based on 1.3 GHz superconducting radio-frequency accelerating technology. The centre-of-mass energy spans a range between 250 - 500 GeV, with the possibility to upgrade the machine up to 1 TeV. The collider design is the result of nearly twenty years of R&D. The superconducting cavities are based on the work done in the 1990s by the TESLA collaboration [49]. Since 2005, the design of the ILC project is a worldwide international collaboration that has given rise to a consensuated technical design reflected in the TDR [50]. The host country for the accelerator has not yet been chosen. Japan is considered the most likely location for this facility.

2.2.1 ILC stages

While performance requirements at the maximum energy dictate many of the key parameters and the overall geometry and cost of the machine, running at lower energies is also an important part of the physics potential of the ILC. The baseline operational range of c.o.m energy from 250 GeV to 1 TeV has been set by the physics community to make the most of the ILC.

Table 2.2: Luminosity and running time of the G-20, H-20, I-20 and Snowmass scenarios [44].

	Stage	**500**			**500 LumiUP**		
Scenario	$\sqrt{s}$ [GeV]	500	350	250	500	350	250
G-20	$\int \mathscr{L} dt$ [fb^{-1}]	1000	200	500	4000	-	-
	time [years]	5.5	1.3	3.1	8.3	-	-
H-20	$\int \mathscr{L} dt$ [fb^{-1}]	500	200	500	3500	-	1500
	time [years]	3.7	1.3	3.1	7.5	-	3.1
I-20	$\int \mathscr{L} dt$ [fb^{-1}]	500	200	500	3500	1500	-
	time [years]	3.7	1.3	3.1	7.5	3.4	-
	Stage	**500**			**500 LumiUP**		
Scenario	$\sqrt{s}$ [GeV]	250	500	350	250	350	500
Snow	$\int \mathscr{L} dt$ [fb^{-1}]	250	500	200	900	-	1100
	time [years]	4.1	1.8	1.3	3.3	-	1.9

The physics program of the ILC is rich, with the collider operating at different

centre-of-mass energy points to optimize the physics return. Operations will start at the highest centre-of-mass energy of 500 GeV, followed by 250 and 350 GeV running, for an initial total of eight to ten years. The collider luminosity will then be upgraded for intense running for about another decade. A possible final stage with an energy upgrade up to 1 TeV is also considered. Table 2.2 summarizes the running stages for different scenarios, being H-20 the most accepted by the ILC community.

2.2.2 Machine parameters and accelerator

The ILC accelerator comprise a length of 31 km, hosting two main linacs of 11 km each one and 5 km that comprise the beam delivery lines and the interaction point with the detector. Figure 2.1 shows a schematic view of the accelerator layout and the location of the main sub-systems.

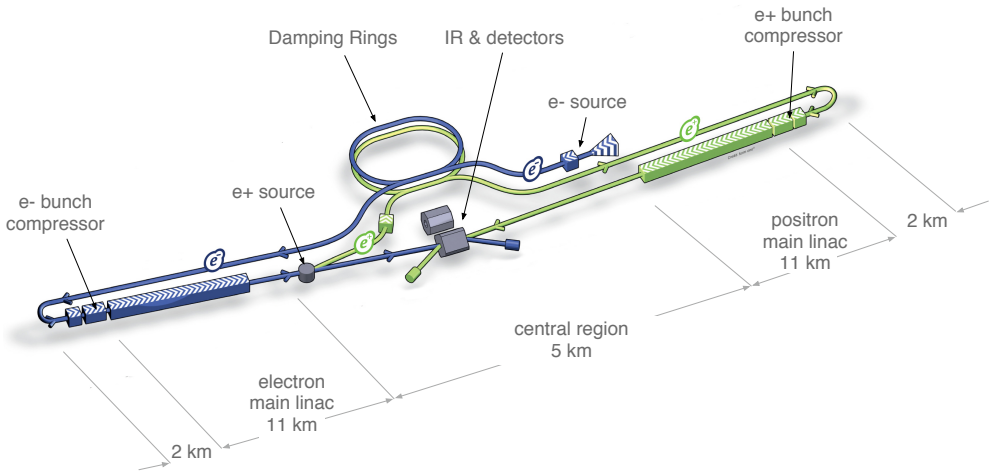

Figure 2.1: An overview graphic of the planned ILC based on the accelerator design of the Technical Design Report (TDR) [51, 52].

The main sub-systems of the accelerator are:

- **Electron source**

  A photocathode DC gun generates bunch trains of polarised electrons. The polarisation of the electrons is expected to be 80% or higher. Then electrons are accelerated up to 5 GeV and sent to the electron damping ring.

- **Positron source**

  To produce the positrons, the beam from the electron main linac passes through a long helical undulator to generate a multi-MeV photon beam which hits a thin metal target to generate showers of electrons and positrons. The remaining photons and the created electrons are separated and then dumped. The positrons are accelerated to 5 GeV and enter their damping ring.

- **Beam polarization**

  The baseline polarimeters of the ILC should provide a 0.5% accuracy on the beam polarisation. The degree of polarization is 80% for the electron beam and 30% for the positron beam (higher values are possible for both species).

- **Damping rings**

  The 5 GeV electron and positron damping rings (DR), with a circumference of 3.2 km, share a common tunnel. The ILC damping rings must accept e^- and e^+ beams with large transverse and longitudinal emittances and damp them to the low emittances required for high-luminosity operation.

- **Bunch-compressors**

  Electron and positron beams are transported from the damping rings to the main linac. A two-stage bunch-compressor reduces the size of the bunch trains from several mm to a few hundred μm before the injection into the main linac.

- **Superconducting RF Main Linacs**

  The main linacs are 11 km long. The accelerating elements of the main linac are superconductive radio-frequency 1.3 GHz cavities with an average accelerating gradient of 31.5 MV/m and a pulse length of 1.6 ms.

- **Beam delivery system (BDS)**

  Two BDS, each 2.2 km long, which bring the beams into collision with a 14 mrad crossing angle at a single interaction point (IP) where the experiment is located.

Table 2.3: Summary table of the 250-500 GeV baseline parameters for the ILC.

Centre-of-mass energy	E_{CM}	GeV	250	350	500
Luminosity pulse repetition rate		Hz	5	5	5
Positron production mode			10 Hz	nom.	nom.
Estimated AC power	P_{AC}	MW	122	121	163
Bunch population	N	$\times 10^{10}$	2	2	2
Number of bunches	n_b		1312	1312	1312
Linac bunch interval	Δt_b	ns	554	554	554
RMS bunch length	σ_z	µm	300	300	300
Normalized horizontal emittance at IP	$\gamma\epsilon_x$	µm	10	10	10
Normalized vertical emittance at IP	$\gamma\epsilon_y$	nm	35	35	35
Horizontal beta function at IP	β_x^*	mm	13	16	11
Vertical beta function at IP	β_y^*	mm	0.41	0.34	0.48
RMS horizontal beam size at IP	σ_x^*	nm	729	684	474
RMS vertical beam size at IP	σ_y^*	nm	7.7	5.9	5.9
Vertical disruption parameter	D_y		24.5	24.3	24.6
Fractional RMS energy loss to beamstrahlung	δ_{BS}	%	0.97	1.9	4.5
Luminosity	L	$\times 10^{34}\,\mathrm{cm}^{-2}\mathrm{s}^{-1}$	0.75	1.0	1.8
Fraction of L in top 1% E_{CM}	$L_{0.01}$	%	87	77	58
Electron polarisation	P_-	%	80	80	80
Positron polarisation	P_+	%	30	30	30
Electron relative energy spread at IP	$\Delta p/p$	%	0.19	0.16	0.13
Positron relative energy spread at IP	$\Delta p/p$	%	0.15	0.10	0.07

The parameters of the 250-500 GeV baseline design are shown in Table 2.3. These parameters represent relatively conservative operating points resulting from optimization subject to the constraints imposed by the various accelerator sub-systems.

2.3 The Compact Linear Collider (CLIC)

The Compact Linear Collider (CLIC) is a high-energy and high-luminosity e^+e^-collider project under development by the world-wide CLIC collaboration. The design was presented in the Conceptual Design Report (CDR)[53] after years of a large number of simulation studies and R&D tests. The nominal collision energy is 3 TeV. CLIC is based on a novel two-beam acceleration technique with acceleration gradients at the level of 100 MV/m. Recent implementation studies for CLIC have converged towards a staged approach offering a unique physics programme covering two decades. In this scheme, CLIC would provide high-luminosity e^+e^- collisions within a centre-of-mass energy range from 380 GeV to 3 TeV [45].

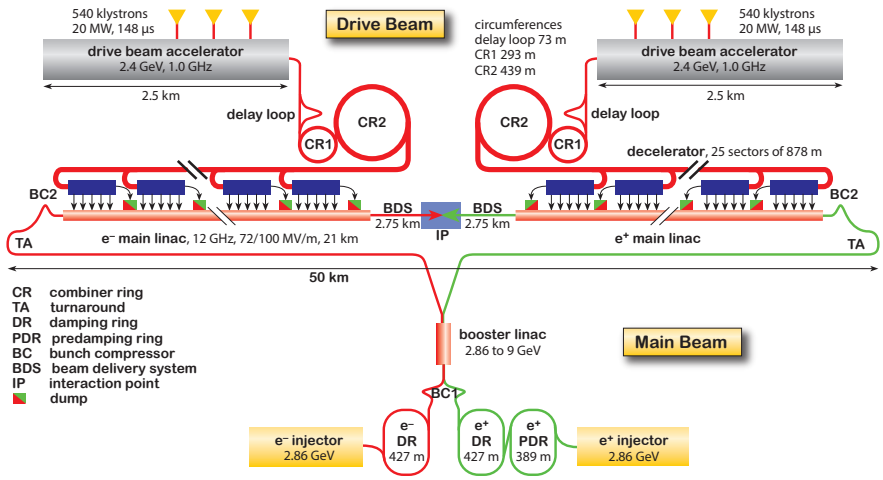

Figure 2.2: Overview of the CLIC layout at $\sqrt{s} = 3$ TeV based on the updated staging baseline document [45].

2.3.1 CLIC stages

The CLIC project presents an ambitious long-term programme, with three energy stages lasting 7, 5 and 6 years, respectively to achieve the integrated luminosity goals, interrupted by 2-year upgrade periods. The total duration of the three-stage programme is about 22 years from the start of beam commissioning. The operating scenario currently planned for the complete CLIC programme is outlined in Figure 2.3 in terms of the luminosity and integrated luminosity as a function of time in years.

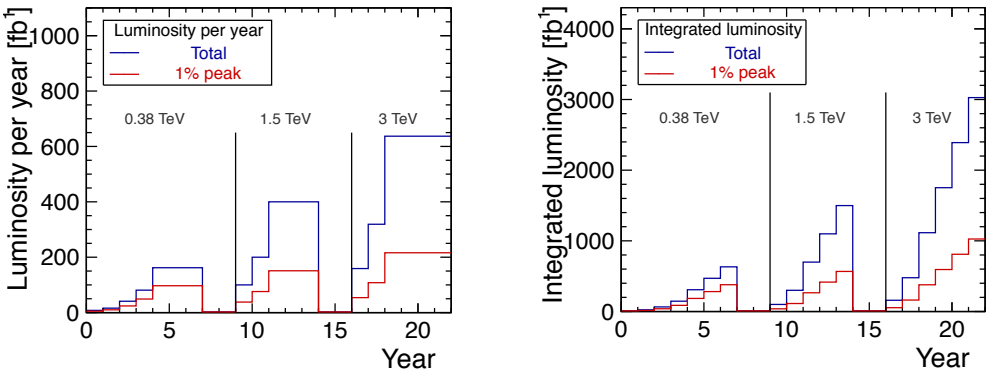

(a) Luminosity per year

(b) Integrated luminosity

Figure 2.3: The luminosity is increase each year (5%, 10%, 25%, 50%) in the first four-years stage and two years (25%, 50%) in subsequent stages.

The duration of each stage is defined by the integrated luminosity targets of 500 fb^{-1} at 380 GeV, 1.5 ab^{-1} at 1.5 TeV and 3 ab^{-1} at 3 TeV collision energy. During the first stage a top threshold scan will be performed near 350 GeV. For this scan an additional integrated luminosity of 100 fb^{-1} will be collected during a few months of CLIC operation. The high-energy programme would be adapted depending on new discoveries at LHC or "elsewhere".

2.3.2 Machine parameters and accelerator

The conceptual layout of CLIC at 3 TeV is shown in Figure 2.2. The main components are:

- **Polarized electron source**

  The CLIC polarized electron source consists of a DC-photo gun, a 1 GHz bunching system, and a 2 GHz accelerator. The electrons are accelerated up to 200 MeV before injection into the common injector linac. A spin-rotator in front of the pre-damping ring orients the spin vertically in the rings. The electron source produces spin-polarized electrons with a degree of polarization of 80% or higher.

- **Positron source**

  The baseline design for the CLIC positron source provides only unpolarized positrons. The source consists of a conventional primary electron-beam linac with energy of 5 GeV, followed by hybrid tungsten targets, a positron capture section, and a pre-injector linac to accelerate the positrons to 200 MeV.

- **Pre-damping and Damping rings**

  The main purpose of the CLIC damping rings is to 'cool' the incoming electron and positron beams to the very small emittances needed for collisions. This goal

is achieved with four rings, a pre-damping and a main damping ring for each particle species. A pre-damping ring (PDRs) is needed to damp the large input emittance, particularly of the positrons, at the high repetition rate of 50 Hz.

- **Booster Linac**

  The booster linac accelerates the beam to the main linac injection energy of 9 GeV. The same linac is shared by electrons and positrons.

- **Ring to Main linac transport (RTML)**

  The RTML connects the damping rings and the main linacs. It consists of beam lines for the transport of the beams from the central injector site, which is close to the surface, to the outer ends of the main linac, which is about 100 m underground. It includes sections for longitudinal bunch compression and spin rotation. The two RTMLs for electrons and positrons each have a total length of approximately 27 km.

- **Drive-beam accelerator (DBA)**

  The DBA consists of 24 short bunch trains of 244 ns length, which follow each other at about 6 μs intervals. DBAs generate then 142 μs long drive-beam pulses and accelerate them to a final energy of 2.4 GeV. For that purpose, normal conducting fully-loaded accelerating structures with an RF frequency of 1 GHz are used. The two DBAs are identical and have a total length of 2.6 km, including injectors and bunch compressors, and provide Drive-Beam pulses for the positron and the electron main linacs in order to achieve the challenging accelerating gradient of 100 MV/m.

- **Delay loops and combiner rings (CR)**

  The time compression of the drive-beam pulses takes place in the Delay Loops and Combiner Rings (CR1 and CR2). An RF deflector operating at the bunch frequency will deflect subsequent 244 ns long trains alternately into the loop or along the straight path. If the flight time of the electrons between the two paths exactly matches the length of the train, the bunches of the delayed train will be placed between the bunches of the following train using a second deflector. The combined train therefore has twice the bunch repetition frequency and twice the peak current. These trains are then injected into the combiner rings, where the bunch repetition frequency is increased to 12 GHz and the peak current to 101 A, reducing the bunch length to 1 mm.

- **Main linacs**

  The two main linacs, one for positrons and one for electrons, accelerate the beams from an initial energy of 9 GeV to the final value of 1.5 TeV using normal conducting accelerating structures with an RF frequency of 12 GHz and a gradient of 100 MV/m. The linac design is identical for electrons and positrons and the linacs are each about 21 km long.

- **Beam delivery systems (BDS)**

  The CLIC BDS transports the e^+/e^- beams from the exit of the high energy linacs, focusing them to the sizes required to meet the CLIC luminosity goals ($\sigma_x = 45$ nm, $\sigma_y = 1$ nm in the nominal parameters) and bringing them into collision with a 20 mrad crossing angle.

The CLIC accelerator can be built in energy stages, re-using existing equipment for subsequent stages. At each energy stage the centre-of-mass energy can be tuned to lower values within a range of a factor three and with limited loss on luminosity performance. A more detailed list of the parameters assumed for the present scenario, with stages at 380 GeV, 1.5 TeV and 3 TeV are given in Table 9 of Reference [45]. In this scenario the first and second stage use a single drive-beam generation complex to feed both linacs, while in the third stage each linac is fed by a separate complex.

2.4 The International Large Detector (ILD)

In this section the performance and specifications of the ILD detector concept for ILC are discussed in further detail. The ILD detector [54], shown in Figure 2.4, is optimised for excellent jet energy resolution over a wide solid angle and for high-precision reconstruction of exclusive final states. The detector is relatively large, and has a sizeable magnetic field to separate charged from neutral particles and to sweep away low-momentum backgrounds. A major goal in the design is the event reconstruction within the Particle Flow Algorithm (PFA) that requires a very robust pattern recognition of particles in the tracker and in the calorimeter.

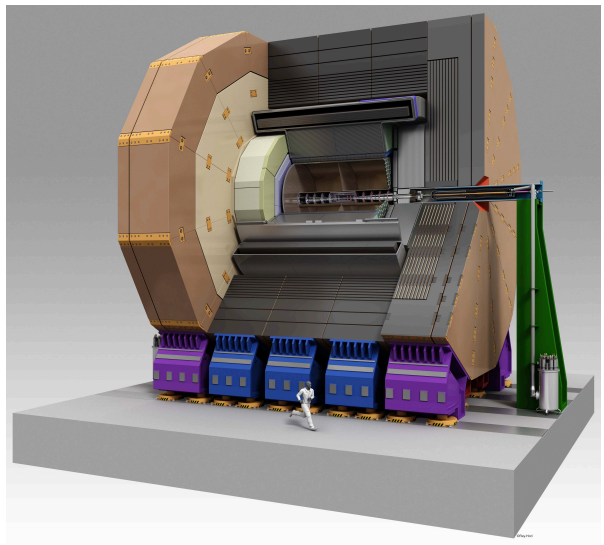

Figure 2.4: Artistic view of the ILD concept.

A system of unprecedented granularity is proposed for the ILD calorimeters. Both the electromagnetic and the hadronic calorimeters are located inside the magnet. The flux from the coil is returned through an iron yoke, which is additionally instrumented to serve as a muon filter. The most forward region is filled by complementary small calorimeters to complete the solid angle coverage and measure precisely the luminosity of the collider.

The tracker system is a combination of a powerful large-volume TPC and an extensive silicon tracking system. The TPC provides up to 200 space points per particle, allowing efficient and highly redundant pattern recognition. Silicon tracking layers, both inside and outside of the TPC provide additional high precision points and precise vertex information.

2.4.1 Tracking systems

The ILD concept combines continuous tracking in the TPC with discrete tracking through silicon detectors. This combination has been chosen to provide a robust system with superb pattern recognition ability.

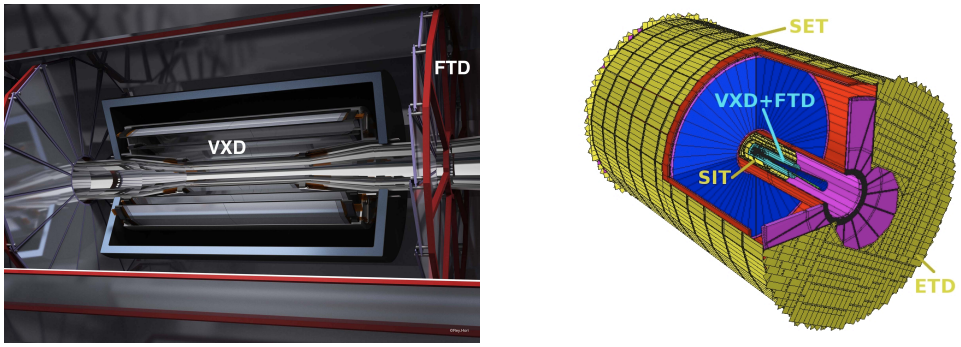

(a) (b)

Figure 2.5: (a) ILD tracking detectors view. (b) 3D detailed GEANT 4 simulation description of the silicon system as sketched.

The interaction point is surrounded by a multi-layer pixel Vertex Detector (VTX) followed by a system of strip and pixel detectors allowing a spatial resolution near the IP better than 3 μm. In the barrel, two layers of silicon Strip Inner Tracking Detectors (SITs) are arranged to bridge the gap between the VTX and the TPC. Outside the TPC, there are two systems of Si-strip detectors, one behind the end-plate of the TPC (ETD) and one in between the TPC and the Electromagnetic Calorimeter (ECAL) (SET). In the forward region, a system of silicon pixel and silicon strip, the Forward Tracking Disks (FTDs), provides small polar angle tracking coverage (down to $\theta = 7^{o}$).

A large TPC measures tracks position at 224 points providing full coverage down to $\theta = 37^{o}$, as shown in Figure 2.6. It is optimized for excellent three-dimensional

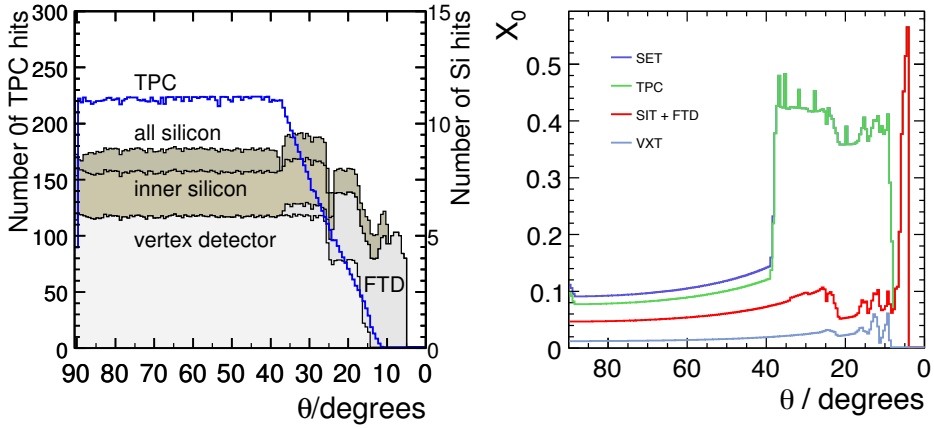

Figure 2.6: (Left) Average number of hits for simulated charged particle tracks as a function of polar angle. (Right) Average total radiation length of the material in the tracking detectors as a function of polar angle

continuous tracking and minimum material in the field cage and the end plate. It also allows particle identification capabilities based on the energy loss of particles per unit of distance (dE/dx). The central inner tracking system, consisting of the six layer VTX and the two layer SIT, provides eight precise measurements down to $\theta = 26°$. The innermost and middle double layer of the VTX extend the coverage down to $\theta = 16°$. Finally, the FTD provides up to a maximum of five measurement points for tracks in the most forward region.

The performance of the tracking system can be summarised by its combined momentum resolution, shown in Figure 2.7. A resolution of

$$\sigma(p_T)/p_T = 2 \times 10^{-5} p_T \oplus a \tag{2.1}$$

can be achieved. For tracks with high p_T the first term is dominant. For soft tracks the second term, $a = 1 \times 10^{-4}$, due to the multiple scattering drives the resolution.

The goal of the ILD vertexing system is given in terms of the resolution on the track impact parameter:

$$\sigma(d_0) < 5[\mu m] \oplus \frac{10[\mu m]}{p_T \sin^{3/2}\theta} \tag{2.2}$$

This goal is crucial for the identification of heavy (bottom and charm) quarks, commonly known as $b(c)$-tagging. Because of the relatively large distance of the innermost FTD disk to the interaction point, the impact parameter resolution degrades for very shallow tracks, $\theta < 15°$. The momentum and impact parameter resolution are shown as a function of polar angle in Figure 2.7.

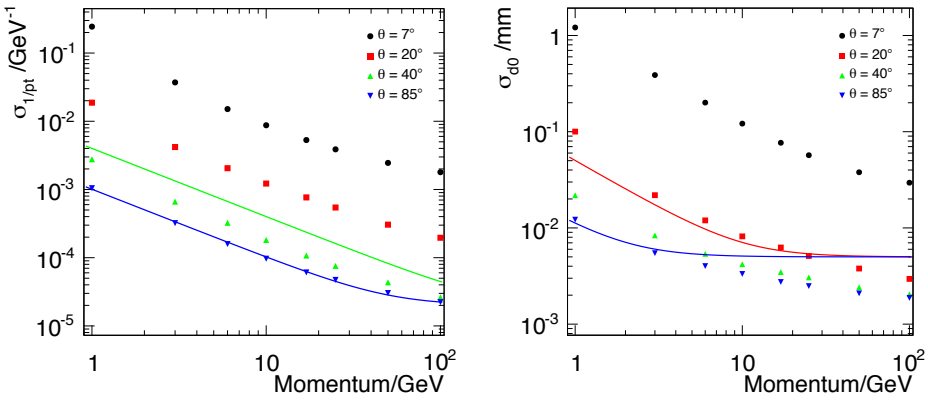

Figure 2.7: Transverse momentum resolution for different angles relative to the beam (*left*). The impact parameter resolution as a function of the particle momentum (*right*).

2.4.2 Calorimeters: ECAL and HCAL

The combined ILD electromagnetic and hadronic calorimeter systems consist of a central barrel part and two end caps. The entire barrel system is contained within the volume of the cylindrical superconducting solenoid. Both calorimeter sections have active layers between tungsten and steel absorber layers.

The particle flow paradigm[1] [55] has a large impact on the design of the electromagnetic calorimeter system. A key requirement is the capability of the system to separate overlapping showers from each other. A calorimeter for particle flow thus needs to be able to do pattern recognition in the shower. Thus an excellent three-dimensional granularity of the device is of utmost importance.

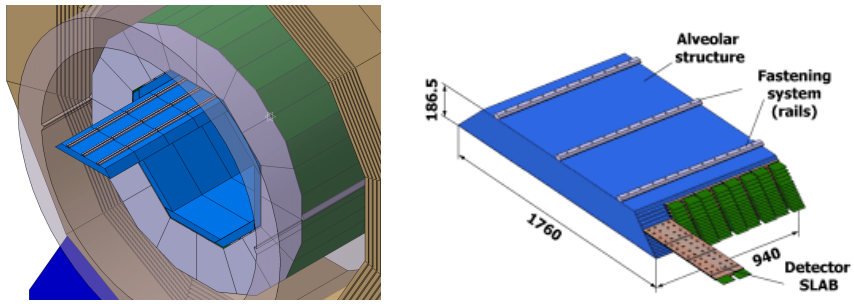

Figure 2.8: The electromagnetic calorimeter in blue (left) and one module from the barrel (right).

For ECAL a solution with 30 readout layers equipped with pixels of 5×5 mm^2 size and a thickness of the ECAL of $24X_0$ has been chosen as the baseline. Silicon Photo

[1] Explained in more detail in Section 4.2.3

Multipliers (SiPM) can cover large areas, are reliable and simple to operate, allow for a thin readout layer and can operate in the 3.5 T strong central magnetic field. In order to have a better separation of close-by showers in the calorimeter, a system with a small Molière radius is advantageous. Hence the choice of dense material (Tungsten) as the absorber. Further help in the separation between electromagnetic and hadronic showers can come from a large ratio between interaction length and radiation length. A small radiation length will move the start of the electromagnetic shower earlier in the calorimeter, while a large interaction length will reduce the fraction of hadronic showers starting in the ECAL.

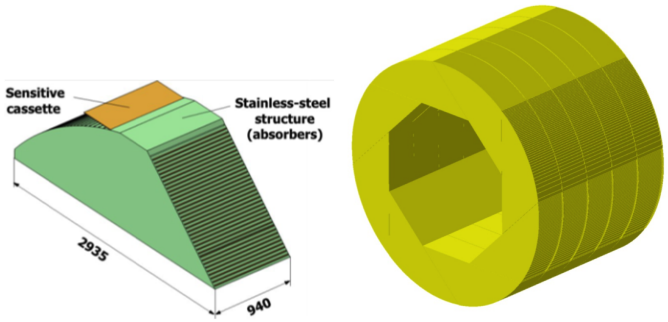

Figure 2.9: The HCAL barrel and end caps (right) and one module from the barrel (left).

The role of the Hadronic Calorimeter (HCAL) is to separate the deposits of charged and neutral hadrons and to precisely measure the energy of the neutrals. Their contribution to the jet energy, around 10% on average, fluctuates over a wide range from event to event, and the accuracy of the measurement is the dominant contribution to the particle flow resolution for jet energies up to about 100 GeV. For higher energies, the performance is dominated by confusion, and both topological pattern recognition and energy information are important for correct track cluster assignment. The HCAL is conceived as a sampling calorimeter with steel absorber and 3×3 cm^2 scintillator tiles or gaseous devices with a segmentation of 1×1 cm^2 as active medium. Due to the rigidity of stainless steel, a self-supporting structure without auxiliary supports (dead regions) can be realised. The fine sampling is beneficial both for the measurement of the sizeable electromagnetic energy part in hadronic showers and for the topological resolution of shower substructure, needed for particle separation and weighting. A superb jet substructure performance is shown in Chapter 5.

2.4.3 Magnet and muon detection system

The ILD detector design asks for a nominal 3.5 T and maximum 4 T solenoidal central field in a warm aperture of 6.88 m in diameter and 7.35 m in length. In addition, in order to suppress background from incoherent pairs from beamstrahlung, an anti-DID (Detector-Integrated-Dipole) is needed. In order to achieve high precision tracking with the TPC, accurate field mapping after construction is requested.

The iron yoke will be instrumented to be used for the detection of muons and for measuring showers escaping the hadron calorimeter (tail catcher). A stable, highly efficient muon identification system with excellent hadron rejection is an important requirement to meet the physics goals of the ILD detector.

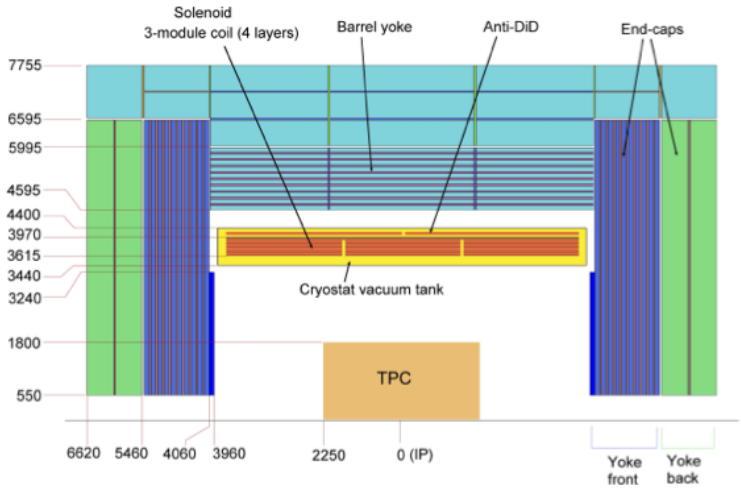

Figure 2.10: ILD magnet cross section, dimensions are in mm (half upper part, cylindrical symmetry).

As shown in Figure 2.10, the barrel part of the yoke is equipped with one sensitive layer in front of the iron yoke, 10 layers spaced by 14 cm in the yoke, followed by three sensitive layers spaced by 60 cm. The forward part of the yoke is equipped with 10 layers spaced by 14 cm, followed by two sensitive layers spaced by 60 cm.

In addition, the yoke serves as the main mechanical structure of the ILD detector and, combined with the calorimeters, should make the detector self-shielding in terms of magnetic field. That allows to work in the vicinity of the detector while its magnet is powered, the fringe field should be less than 50 G at 15 m from the IP, in the radial direction.

2.5 Summary

The ILC is a mature, "shovel-ready" design for a future e^+e^- collider operating at centre-of-mass energies between 250 GeV and 500 GeV, extendable to 1 TeV. Such a e^+e^- can measure the electroweak properties of the Higgs boson and the top quark with unprecedented precision. CLIC, apart from that, can also extend the centre-of-mass energy to the TeV scale, adding extra potential for new physics searches. A complete detector concept based on particle flow has been developed. High-resolution tracking systems and high-granularity calorimeters provide the sensitivity required by the physics case for lepton colliders.

Chapter 3

Detector R&D: ultra-transparent, self-supporting silicon detectors with integrated cooling

As discussed in Chapter 2, detectors for future colliders have been designed to achieve the requirements of the physics program over the full range of c.o.m. energies from a few hundreds of GeV to 3 TeV. This has motivated highly granular calorimeters and highly efficient tracking systems with very low mass detectors and supports. A worldwide detector R&D effort is ongoing to fully satisfy the challenging requirements.

The current generation of solid-state position sensitive devices has better precision, greater integration and less material than previous generations of detectors. Detector solutions have been developed for 50 micron thin, small-pixel sensors with a resolution of a few microns. Ultra-thin sensors require new concepts for mechanical support that maintain good thermo-mechanical performance at a fraction of the material budget traditionally reserved for these services. In the following sections[1] the all-silicon pixel detectors concept is presented and the performance of different cooling strategies for future detectors is evaluated.

3.1 Ultra-light Silicon Detectors

Detector concept studies for future linear colliders have established a number of challenging performance goals based on the analysis of benchmark channels and an evaluation of the future e^+e^- colliders environment. The first layer of the ILC and CLIC

[1]The thermo-mechanical tests presented in this chapter have been performed by the author in three institutes, IFIC, DESY and CERN. The power pulsing system, presented in Section 3.2, was developed by José Manuel Deltoro as part of his final degree work in Electronic Engineering. The shown results on integrated cooling in silicon detectors are based on Reference [56].

vertex detectors must cope with large backgrounds due to incoherent pair production. The required impact parameter resolution (Equation 2.2) goal represents a considerable improvement over vertex detectors built at collider experiments to date; the constant term is better by a factor of two to four than what was achieved at previous colliders and at the LHC. Achieving the requirement for the second (material) term is even more challenging; it has to decrease by a factor of six to ten with respect to most previous experiments.

Intense detector R&D has yielded several candidate technologies that can meet these requirements. A good example is the DEPleted Field Effect Transistor (DEPFET) [57, 58] technology, a highly granular, ultra-transparent active pixel detector for high-performance vertex reconstruction at future collider experiments. It reduces the material in the sensitive area to approximately 0.15 X_0 of radiation length. A DEPFET vertex detector for a future linear collider was proposed for the first time in 2002 [59, 60]. The DEPFET collaboration has since shown that finely segmented devices with large in-pixel gain can indeed be constructed and operated. Read-out and control ASIC have been designed and produced, and a novel ladder design with excellent thermo-mechanical properties has been developed.

3.1.1 Cooling strategies

To achieve an ultra low-mass detector configuration, cooling systems for future detectors must have the minimum impact on the material budget. Detector concepts for future electron-positron colliders [54, 48] aim for a total material budget of 0.12 - 0.2% X_0/layer. This would be equivalent to only 100-200 μm of silicon. Below, three cooling strategies compatible with this material budget are described:

- **Power-pulsing**

  The power-pulsing scheme is actively pursued by the R&D effort for a future linear collider at the energy frontier (ILC, CLIC). The detectors follow the duty cycle of the machine (approximately 1 ms of collisions every 200 ms for the ILC, 150 ns of collisions every 20 ms for CLIC), going to a "stand-by" state during the long intervals between bunch trains, thus reducing the average power consumption by a large factor. One of the most significant benefits of power-pulsing is that the vertex and tracking detector may not need active cooling. This significantly lowers the overall mass budget for these detectors, which is crucial for obtaining the required resolution.

- **Air flow cooling**

  The use of conventional liquid/two-phase cooling solutions would result in a significant increase in material budget from both the cooling medium and its tubing. Therefore, the use of a dry gas (air or N_2) as a coolant for the inner region detectors would be a suitable option to achieve the specified material budget. The flow for barrel cooling is assumed to be from one barrel end to the other. This cooling method has been tested recently with a mock-up of the vertex detector for CLIC [61].

- **Micro-Channel Cooling (MCC)**

  Micro-cooling channels integrated in the detector itself provide a very effective means of removing heat. Bringing the cooling circuit to within hundreds of microns of the heat source and removing thermal barriers (material interfaces, glue layers) reduces the temperature gradient between the heat source and the cooling liquid. The minimal extra material in cooling fluid and circuits helps to reduce the material involved in removing the heat from the detector.

3.1.2 Mechanical samples

To evaluate the performance of the cooling strategies presented before, a number of mechanical samples, based on the silicon-on-insulator thinning concept [62] developed for DEPFET active pixel detectors, were produced. These thermo-mechanical samples are equipped with resistive circuits implemented in an Aluminium layer deposited on the surface, that simulate the heat-load from the read-out and steering electronics. Narrow traces are laid out in a serpentine geometry to maximize the length of the trace and thus achieve a resistance of 10-100 Ω.

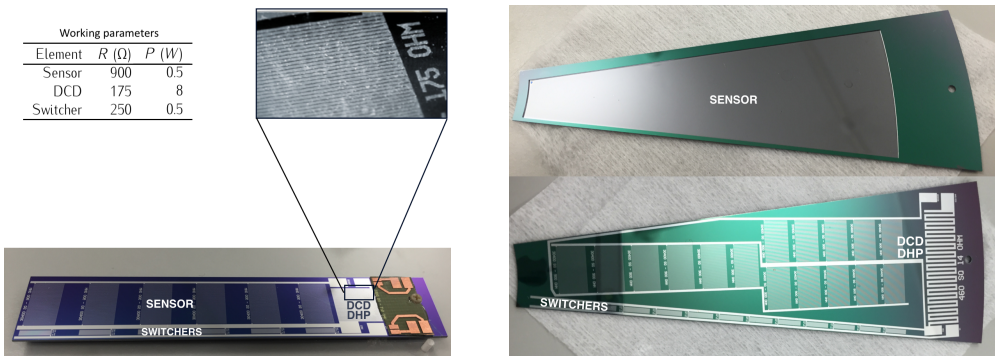

(a) (b)

Figure 3.1: (a) Silicon mechanical sample based on the DEPFET ladder for the PXD of Belle II experiment. (b) Petal-shaped sample for the FTD of the ILD detector concept. The frame has a thickness of 500 μm, whereas the sensor (central) region is thinned to 75 μm.

Pictures of two types of mechanical samples are shown in Figures 3.1(a) and 3.1(b). Three independent circuits roughly correspond to the end-of-ladder electronics of the DEPFET ladder design for Belle II (this is where the read-out chips are located), the balcony with steering chips (running along the lower edge of the images) and the sensor itself (the grey areas that cover the full width of the sensor). The instantaneous power dissipation is up to 6 W on less than 1 cm^2 of the end-of-ladder area. On the sensor area and balcony, 1 W and 0.5 W are dissipated respectively.

Apart from the mechanical silicon ladders for the barrel region, several petal-shaped mechanical samples were also produced to characterise thermally the forward region of the vertex detector, as shown in Figure 3.1(b). Petals were designed with the required

dimensions to equip the FTD-DEPFET concept presented in DBD [54]. Disks are fully covered by 24 petals, 12 petals per face, and sensors are optimised to yield excellent $r - \phi$ resolution of 3-5μm, with narrow read-out columns oriented radially along R.

3.2 Power pulsing

Pulsed powering may lead to temperature excursions, to significant mechanical stress and to vibrations that can affect detector performance or its life time. It is therefore crucial that prototypes are tested in a realistic environment. In the following the design and performance of a multi-channel power supply developed to provide short pulses of programmable high power to the mechanical samples are presented. The system is intended primarily for tests of prototypes for ILC and CLIC, but is sufficiently flexible that it can be reprogrammed with the duty cycle of other machines.

3.2.1 Power pulsing system

The pulsed power system developed at Instituto de Física Corpuscular (IFIC) [63], shown in Figure 3.2(a), was designed to generate short pulses of power. Several output channels – up to 32 – are available. The system can be reconfigured to different circumstances by reprogramming the central unit. The voltage level on the output of the different channels can be programmed individually. Simultaneous operation of several channels with different voltage levels is possible. The duty cycle – both the repetition frequency and the duration of the pulse – is programmable, such that the same setup can be used to study the ILC and CLIC environment. Figure 3.2(b) shows the pulses of three channels for an ILC duty cycle of 1/200 ms.

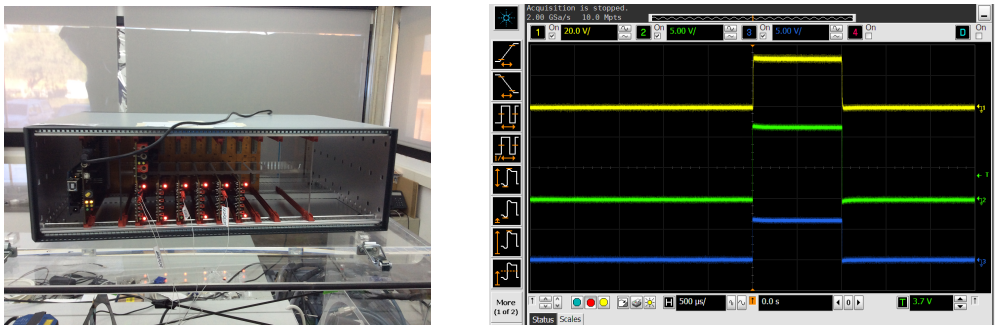

(a) (b)

Figure 3.2: (a) Picture of the pulsed powering system developed at IFIC; (a) Output pulses provided by the power pulsing system for the three independent circuits over the silicon samples.

The system is implemented as five types of inter-connected Printed Circuit Board (PCB): a central control unit, an input board, the backplane that connects everything

and two output boards. The control board houses the central microprocessor that controls the output voltage levels and steers the duty cycle. The system is based on the Arduino "open hardware" platform [64]. Through a number of multiplexers the Arduino control unit can decide which board is activated, which output board is programmed and which output board can report its output voltage measurement[2].

3.2.2 Experimental setup

The thermal characterization of the ladder with a pulsed power supply is carried out in the experimental setups shown in Figure 3.3. The setup consists of a conventional power supply connected to the pulsing system, an oscilloscope to check the output pulses and a specific device for thermal measurements. Particularly, in a first attempt, in the experiment shown in Figure 3.3(a), a Bragg fibre read-out system [66] jointly with an interrogator is used to measure the temperature of the hottest region of the ladder (approximately in the centre).

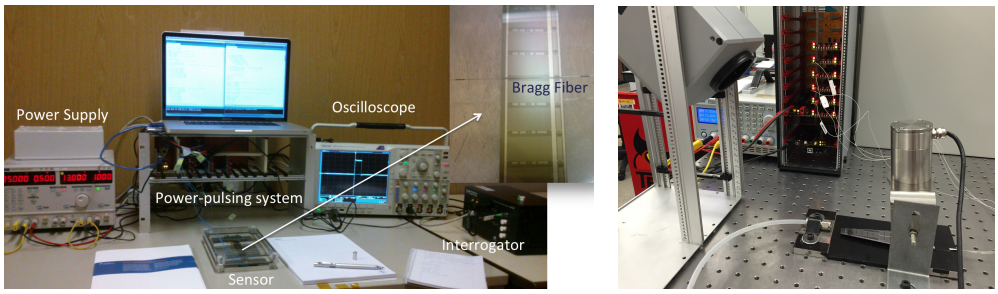

(a) (b)

Figure 3.3: Photographs of the setup for thermo-mechanical characterization of low-mass pulsed-power supplied detectors proptotypes, a ladder sample in (a) and a petal sample in (b).

On the second experiment with the petal-shaped silicon samples shown in Figure 3.3(b), the temperature profile is monitored with a thermal infra-red camera (FLIR Systems ThermaCAM SC500) in order to locate the hottest point. A more precise reading of this hot spot is acquired with a second single-spot infra-red sensor (Optris CTLaser OPTCTLLTFCF1).

The impact of this cooling method on the mechanical stability is evaluated with a non-contact capacitative sensor (Micro-Epsilon Capa NCDT 6100). This kind of sensors is sensitive to displacements and vibrations produced on a target surface by external factors or temperature changes. It measures quick changes in capacitance which translates later into changes in position with an accuracy level of 0.15 μm.

[2]This work formed part of the AIDA Work Package 9 (WP9.3.2 [65])

3.2.3 Thermo-mechanical performance

The power pulsing supply is used to generate 1 ms pulses with large peak power, followed by 200 ms without power consumption, representing the bunch structure of the ILC. The maximum value of the power pulses which is supplied to the three independent circuits of the mechanical samples corresponds to the nominal load of a DEPFET sensor presented in Section 3.1.2. Then silicon samples are subjected to a heating-cooling cycle. It means that the power supply is initially switched off and subsequently it is switched on in order to evaluate its impact on the temperature of the sample. Despite the high-speed read out (1 KHz) of the Bragg fibres, temperature changes registered on samples are limited by the thermal inertia of the Silicon which yields a time constant of 7 s. Hence rapid thermal variations below 7 s are absent. Figure 3.4(a) shows the thermal curve of the Silicon during a heating-cooling cycle.

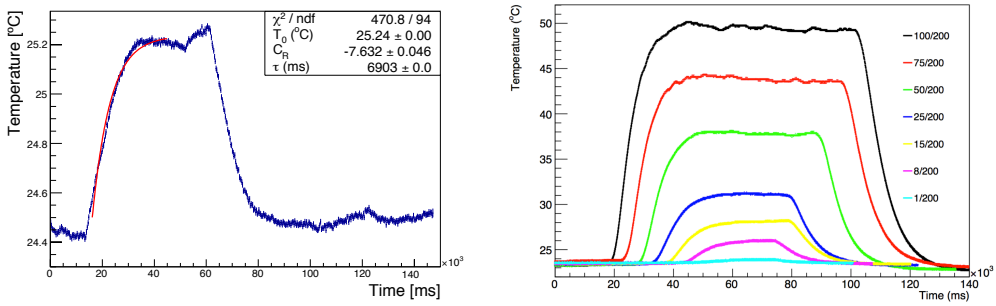

(a) (b)

Figure 3.4: (a) Heating-cooling curve of the silicon sensor upon a rapid change in the power supplied to the resistive circuits that mimic the power consumption of the read-out electronics; (b) Heating-cooling curves for different duty cycles, from 1/200 (ILC) to 100/200.

A new set of measurements was performed varying the length of the pulse, starting from the ILC duty cycle of 1 ms pulse duration each 200 ms to a pulse of 100 ms. Results are shown in Figure 3.4(b). As longer is the pulse larger temperature gradient is achieved on the silicon surface. For instance, when the sensor is powered half of the time (which correspond to the black curve in 3.4(b)) a temperature increase of 27°C is obtained. However, duty cycles under 50/200 offer better cooling performance maintaining acceptable temperature gradients below 10°C.

The last measurement focuses on very fast thermal excursions. The measurements from a long time series are averaged to create a precise measurement on a 201 ms window, shown in Figure 3.5. No fast thermal excursions are observed. An upper limit on the magnitude was derived of 0.1°C.

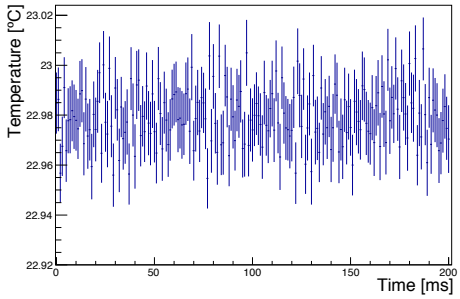

Figure 3.5: Average thermal excursions within a 201 ms window.

3.3 Air flow cooling

Air flow cooling is the most conventional strategy for electronic systems because of its simplicity and the small added material. Thus, using a dry gas for cooling the innermost regions of a future detector would be able to fulfil the required detector specifications. However, in position-sensitive devices the mechanical impact can be dangerous when the required spatial resolution is only a few microns. In this section, amplitudes of vibration and eigen modes are evaluated for a thin silicon petal in an air flow.

3.3.1 FTD mechanical support

In order to study the thermo-mechanical behaviour of the dummy petals, a first mock-up of the FTD for the ILD detector was developed at IFIC. A picture of the mock-up is shown in Figure 3.6. The disk was designed with the dimensions of the FTD-1 indicated in [54], the inner radius is 39 mm (9 mm radially separated from the beam pipe) and the outer is 164 mm. The disk supports a total of 24 petals, 12 petals in the forward face and 12 in the backward face with the aim the get the maximum sensitive area as possible. Figure 3.6(b) shows a picture of the disk with 2 silicon petals and the remaining ten made of stainless steel.

3.3.2 Experimental setup

The mechanical characterization was mainly carried out in the CLIC laboratory at CERN, described in [61]. A small half-disk, shown in Figure 3.7(a), hosting the sensor was tested in the wind-tunnel of Figure 3.7(b).

The platform allows to rotate the system freely, therefore the half-disk can be oriented at different angles respect to the air flow direction. A ventilator is used to force the air along the wind tunnel. Close to the air vent, a metallic sheet provides the transition from the round opening of the ventilator to the rectangular cross section of the wind tunnel. Openings at different locations on the wind tunnel allow measuring the air temperature (using IST Class A PT1000 sensors) and air velocity (using Schmidt

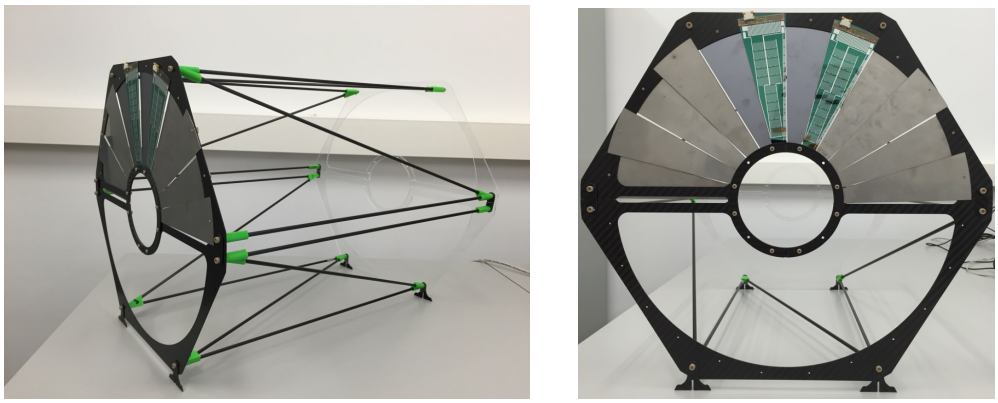

(a) (b)

Figure 3.6: (a) FTD mock-up formed by a 1 mm thickness carbon-fiber disk (left), a plastic disk (right) joined by CF tubes and 3D printed joints. (b) Front view of the disk.

SS 20.400 flow sensors). The mechanical impact of the air is determined using a triangulating sensor (Micro-Epsilon OptoNCDT ILD2300-10) located a few centimetres above the sensor. This sensor provides readings of the distance to the petal perpendicular to the sensor surface with a resolution of 0.15 μm. The read-out frequency of 1.5 kHz is sufficient to monitor vibrations in the most important frequency range. All data were acquired using a National Instruments CompactDAQ system and processed using a custom made LabVIEW program provided by CLIC laboratory responsible.

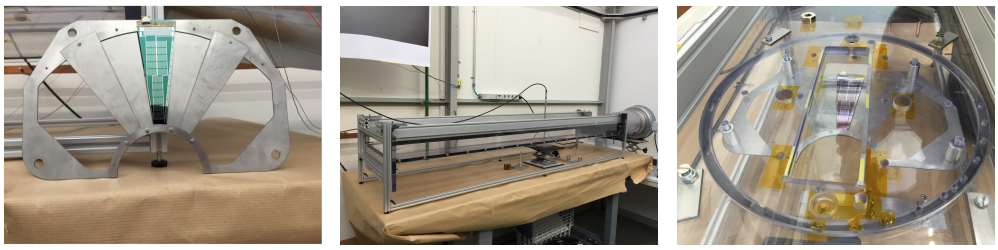

(a) (b) (c)

Figure 3.7: (a) Re-designed stainless steel disk. (b) Wind tunnel at the CLIC laboratory. The ventilator located on the right of the photo sucks the air through the rectangular tunnel. In the middle a platform is mounted to work as a support structure for the samples. (c) Top view of the platform.

3.3.3 Thermo-Mechanical performance

Thermal performance

The thermal measurements were registered with the same temperature sensors presented in section 3.2.2. The air speed was fixed at 2.5 m/s for two reasons, first because the mechanical impact is small and fulfils the spatial-resolution requirements of the detector and second because it is expected to be fast enough to dissipate a large fraction of the heat produced by the nominal power of the sensors, as it was argued in [58].

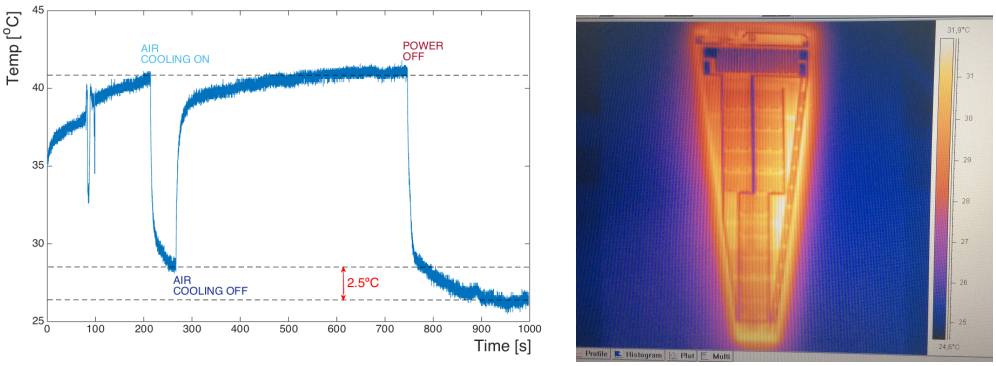

(a) (b)

Figure 3.8: (a) Heating-cooling cycle. (b) Thermal image of the powered petal.

The silicon petal was submitted to a heating-cooling cycle. First, half the nominal power (3W, 0.5W, 0.25W) is supplied to the dummy, once the temperature achieves a stable maximum the air flow is turned on for cooling. The heating-cooling curve is shown in 3.8(a). An air speed of 2.5 m/s speed can dissipate approximately 85% of the heat of the mechanical sample. The initial temperature increase of 15°C is reduced to 2.5°C when the air is flowing. If one extrapolates this result to the nominal power configuration (6W, 1W, 0.5W), it is expected to keep the temperature gradients below 10°C.

Mechanical performance

In order to evaluate the impact on the mechanical stability of the silicon petal due to an air flow, the following measurements were considered:

- Amplitude of vibration dependence with the air velocity
- Impact of the air incidence angle
- Extraction of the vibration eigenfrequencies

For the first measurement, the air velocity is varied from the lowest value given by the system (1.7 m/s) to the highest (12.3 m/s). Figure 3.9(a) shows the Root Mean Square (RMS)[3] of the position, which is a measure of the vibration amplitude, as a function of the air velocity. The dependence is fit to a parabolic curve. According to the results, for an air velocity of 6 m/s or below, the out-of-plane vibrations are kept below 2 μm. Therefore, the mechanical impact of the air flow is not disturbing for velocities of a few m/s.

In the next measurement, the platform is rotated from the initial position, tagged as 0°, to 180° in steps of 30°. In this case, the air velocity is fixed to a value of 7.5 m/s.

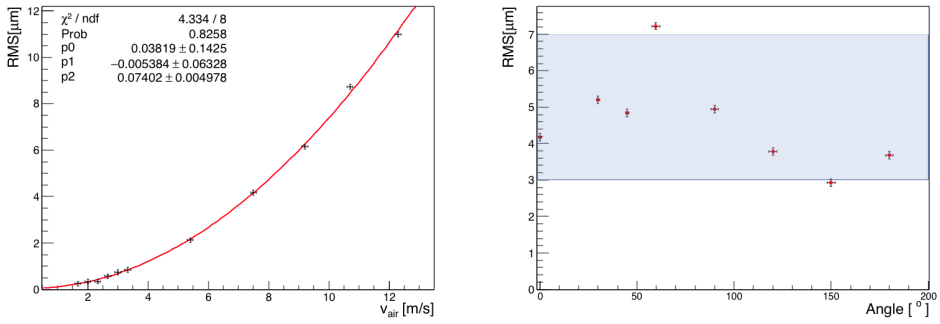

(a) (b)

Figure 3.9: Mechanical performance: Amplitude of vibration (or RMS) as a function of (a) the air velocity; (b) the angular position.

Results in Figure 3.9(b) show that the amplitude varies within a range of 3-7 μm depending on the angular position. The highest impact is observed for 60° and the lowest at 150°, while 90° gives an intermediate value. It might be consequence of the asymmetric structure of the petal. When the air hits the narrowest part of the petal first, it produces smaller vibrations. On the contrary, if the air flows from the widest part in the opposite direction, the mechanical impact increase producing amplitudes that are twice bigger. Hence, an air cooling system for the FTD should blow air radially from the inner part of the disk outwards in order to minimize vibrations in the silicon petals.

Finally, the last part of the mechanical characterization took place at IFIC. The measurement of the eigenfrequencies of a system requires well defined boundary conditions (clamping points, air speed, material, etc...). To extract the eigenmodes of the petal, it should be isolated from external influences, i.e., the configuration shown in Figure 3.7(a) is not valid for this purpose because of the frequencies of the entire

[3] RMS $= \frac{\text{Peak-to-Peak}}{2\sqrt{2}}$ where Peak-to-Peak is the change between the highest amplitude value of the measured signal and the lowest.

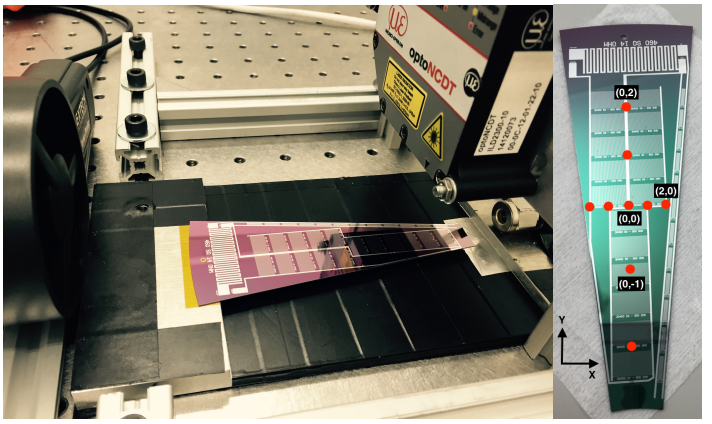

(a) (b)

Figure 3.10: (a) Setup for modal characterization of a single silicon petal. (b) Spatial points of measurement in the (x, y)-plane.

structure can overlap with the eigenfrequencies of the silicon petal. Pictures of the new setup are shown in Figure 3.10(a). Mechanical vibrations are read with the same Epsilon triangulating sensor. Air flow is supplied by a common compressed air system, impacting first on the narrower part of the petal. For that experiment the air speed was fixed at 2.5 m/s and the petal was clamped only in a single point, allowing the other end to move freely.

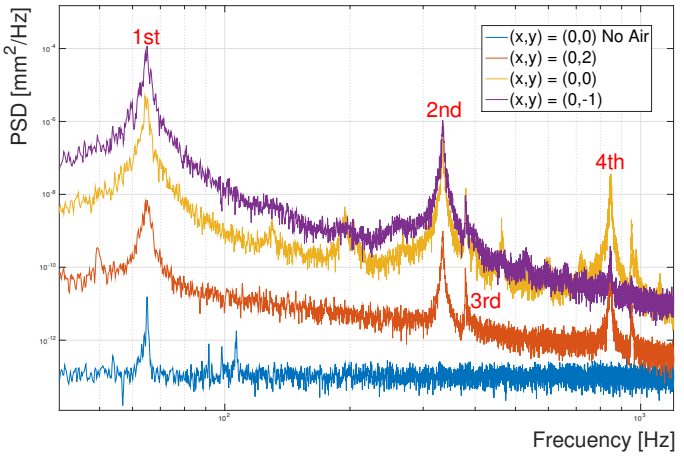

Figure 3.11: The spectral power density of 4 time series registered with the triangulating sensor at different points over the petal.

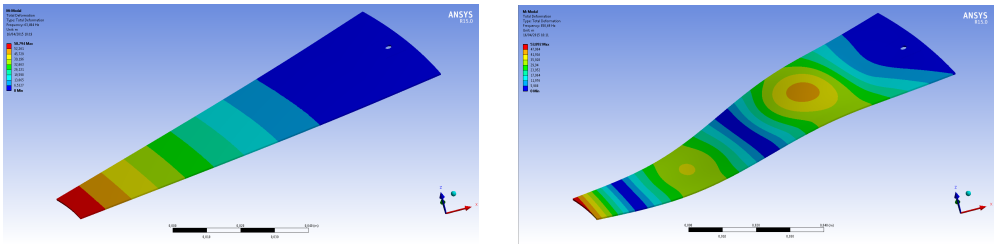

Figure 3.12: Graphical representations of the modal analysis from finite-element simulation. (a) 1^{st} vibrational mode. (b) 4^{th} vibrational mode

A mode of vibration is characterized by a modal frequency and a mode shape. Eigenmodes may produce maximum deformations at different points. In order to study the first order modes a mapping through the plane of the system must be done. For that purpose the amplitude of the out-of-plane vibrations is measured at different locations along the surface of the dummy petal. The picture in Figure 3.10(b) shows the spatial points in the (x, y)-plane where the sensor is focused.

The readings in the time domain are translated to the frequency domain using a Fast Fourier Transform (FFT). The spectral power density is plotted in Figure 3.11 for frequencies from a fraction of Hz to several kHz. The prominent peaks represent the first four eigenfrequencies of the petal. Results are given in Table 3.1. These eigenmodes correspond to the bending modes for a single-point support configuration of the petal. A finite-element (FE) simulation is used to predict the vibration modes of the petal. A graphical example of the deformations caused by the 1^{st} and 4^{th} eigenmodes is shown in Figure 3.12. The predicted eigenfrequencies agree well with the data.

Table 3.1: Eigenfrequencies of the first four vibration modes of the dummy petal in a single-point clamping configuration.

Eigenmodes	1^{st}	2^{nd}	3^{rd}	4^{th}
Data$[Hz]$	65.0	334.2	379.4	845
FE simulation $f[Hz]$	63.5	340	379	850,7

In more realistic conditions, petals are clamped in more than one point, at least two points to ensure the stiffness required for sensors of a few μm resolution. For that reason, a double-point support configuration of the petal was also studied. The eigenfrequency is four times higher. Results are shown in Table 3.2. The clamping of the petals on the support structure is therefore important for mechanical performance. Even if data and FE simulation are less consistent in this configuration, the FE simulation provides a qualitative description.

Table 3.2: Eigenfrequencies of the first three vibration modes of the dummy petal in a double-point clamping configuration.

Eigenmodes	1^{st}	2^{nd}	3^{rd}
Data$[Hz]$	253	502	740
FE simulation $f[Hz]$	290	454	597

3.4 Integrated cooling channels in silicon detectors

In this section the integration of cooling and active detector elements is taken one step further by monolithically integrating a micro-channel cooling circuit in a silicon sensor. A low-pressure, low-mass, mono-phase cooling solution for applications with a relatively modest power density and room-temperature operation are the chosen conditions for the experiment in combination with very strict requirements on the material budget. A production process that combines commercial micro-electronics processing with wafer thinning and the etching of a micro-cooling circuit is validated. Finally, the thermo-mechanical performance of prototypes is characterized. For this purpose, a custom connector was developed and a finite element simulation model was developed to allow rapid feed-back from laboratory measurement and simulation. Compared to previous low-mass proposals (in particular cooling via an air flow in the detector volume) micro-channel cooling is expected to provide a much tighter control over the local temperature.

3.4.1 Microchannel circuits

The integration of micro-channels is based on the silicon-on-insulator thinning concept [62] developed for DEPFET active pixel detectors. The process uses two silicon wafers: the top (sensor) wafer forms the active detector material, while the bottom (handle) wafer forms the supporting frame of the all-silicon ladder and, in this implementation, hosts the micro-channel cooling circuit.

The process is schematically represented and described in Figure 3.13, a more detailed explanation can be found in [56]. The manifold design is shown in Figure 3.14. The inlet and outlet are shown on the leftmost side of the design. Both have a length of 5 mm and an approximately rectangular cross-section of 340 $\times$ 380 μm^2. A manifold with multiple cooling lines in parallel is formed by fanning out the inlet in the triangular area. The single channel is divided into 11 separate channels.

The 11 cooling channels have a cross-section of 200 $\times$ 340 μm^2 (width $\times$ height). The lengths of the channels vary according to their location; the length of the inner loop is 20 mm, that of the outer loop 40 mm.

The manifolds are etched into a 450-525 μm thick silicon handle wafer. The photographs 3.15(a) and 3.15(b) of Figure 3.15 present two details of the circuit. The photograph on the left zooms in on the position where the inlet separates into several cooling channels. The circular structures are pillars that support the thin layers of

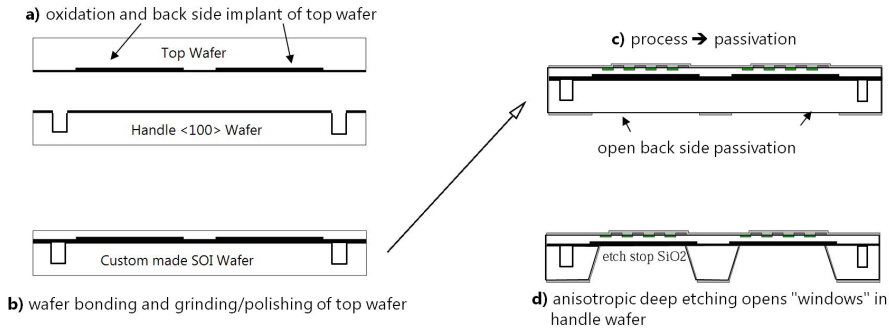

Figure 3.13: The process sequence for production of thin silicon sensors with electrically active back side implant and integrated cooling channels starts with the oxidation of the top and handle wafer and the back side implantation for the sensor devices; cooling channels are etched into the handle wafer before bonding (a). After direct wafer bonding, the top wafer is thinned and polished to the desired thickness (b). The processing of the devices on the top side of the wafer stack is done on conventional equipment; the openings in the back side passivation define the areas where the bulk of the handle wafer will be removed (c). The bulk of the handle wafer is removed by deep anisotropic wet etching. The etch process stops at the silicon oxide interface between the two wafers (d). The cooling channels are only accessible after dicing of the wafers.

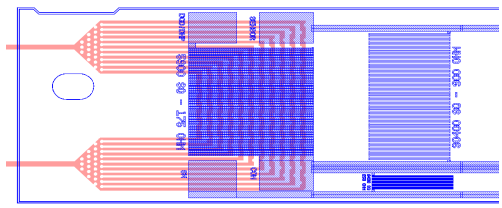

Figure 3.14: The cooling manifold is located exactly under the end-of-ladder heater circuit, where the greatest temperature gradients are expected.

silicon covering the triangular area. The photograph on the right shows a detail of the corner of four cooling channels. The X-ray images in Figure 3.15(c) and 3.15(d) present detailed X-ray views of the same areas of the circuit after sealing the circuit with the top wafer.

To deal with the connectivity problems and to evaluate the thermo-mechanical performance a small number of test structures was designed and produced for a characterization in the laboratory. For these first samples the handle wafer thinning step is not performed. Figure 3.16 presents a photograph of these mechanical samples. They are identical to the samples presented previously in Section 3.1.2, but with an integrated micro-channel circuit.

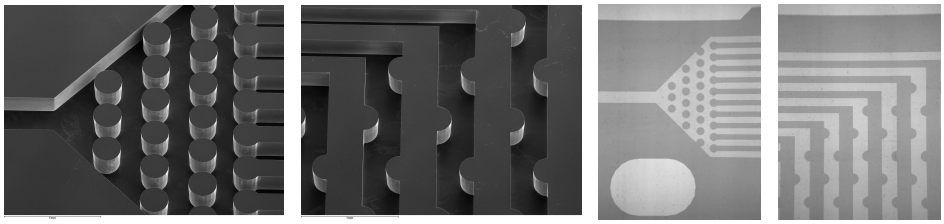

(a) (b) (c) (d)

Figure 3.15: Photographs of the micro-channel cooling manifold etched into the *support* wafer before bonding the *sensor* wafer that closes the circuit. The photograph (a) zooms in on the position where the inlet (on the left of the image) fans out into several cooling channels. The circular structures are pillars that support the thin layers of silicon covering the triangular area. The photograph (b) shows a detail of several of the cooling channel. X-ray images of the same structures in the micro-channel manifolds after sealing the circuit with the top (*sensor*) wafer are shown in (c) and (d).

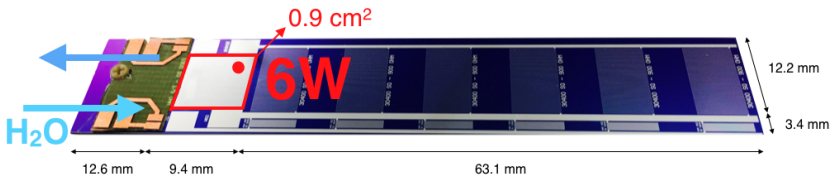

Figure 3.16: A 540 μm thick silicon ladder with an integrated micro-channel cooling circuit. The micro-manifold is located in the red box in the image. The arrows indicate the approximate locations of the inlet and outlet channels. The resistive circuit are visible as grey areas.

3.4.2 Connectors

To connect the micro-channel manifold to a laboratory cooling circuit a custom interface is used that connects the inlet and outlet to standard commercial high-pressure connectors. This connector consists of plastic piece that slides over the silicon sensor, as shown in Figure 3.17. The silicon joint is sealed with a glue layer (Araldite 2020/2011). On the opposite of the connector there are two threaded holes to connect the standard fittings of the 6 mm outer diameter tubes, visible in the upper left corner of Figure 3.17(a). The channel in the connector gradually reduces the circular cross section of the tube fittings to a square cross section of 400 $\times$ 400 μm.

The connectors were produced in a 3D printer using the Stereolithography (SLO) process offered by Sicnova. This technique offers a mechanical precision of 15-30 μm and with thin layers of less than 300 μm. The material *visijet FX clear* with a flexural (tensile) strength of 52 MPa (82 MPa). The low-Z material of the connector has a radiation length of approximately 40 cm. The full thickness of the connector in Figure 3.17(a) corresponds to 0.8% X_0 for a particle crossing under a 90° angle, clearly

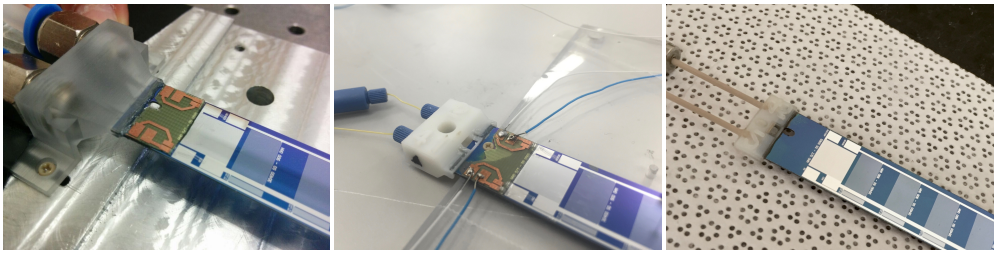

(a) (b) (c)

Figure 3.17: Photographs of the silicon ladder with the integrated cooling circuit and the 3D-printed connector to the cooling circuit. The three interface the micro-channel cooling circuit to commercial fittings (they are visible in the upper left corner of the three images).

prohibitive for applications inside the tracking volume of a particle physics experiment. A miniaturized version of the connector has been designed, that offers a reduction of the material by a factor four, while maintaining compatibility with a commercial fitting standard. The result is shown in Figure 3.17(b).

Even smaller connectors have been developed recently as Figure 3.17(c), that glue directly a 800 μm diameter PEEK micro-tube. These offer a solution with a full thickness equivalent to 0.05% X_0 and may be interesting for applications that require the connectors to be in the detector acceptance[4].

Several assemblies consisting of a connector glued onto a silicon sensor were tested for leaks in the CERN micro-channel cooling laboratory. No detectable increase of the Helium level was observed, which allows to put an upper bound on the leak rate. The maximum pressure that the connector shown in Figure 3.17(a) stand is 180 bar. For the other two designs, Figures 3.17(b) and 3.17(c), only lower limits (>80 and >30 bar) exist.

3.4.3 Finite Element Simulation

A finite-element simulation is used to predict the performance of the micro-channel cooling. The geometry of the manifold is implemented in the CFD software Ansys 17.0. The meshed geometry has a total of 4 million elements, which allows to observe local effects in detail. The cooling fluid in the simulation is pure water and the solid element is silicon. The physical properties of both materials assumed in the simulation are shown in Table 3.3. The boundary conditions in the simulations - the total power applied to the micro-channels and the mass flow - are given in the first two columns of Table 3.3. They are as close as possible to the laboratory set-up. The environment temperature is set to 25°C, similar to the ambient temperature in the laboratory. The convective heat transfer coefficient used between the sensor and the air is $h = 5W/m^2K$. The temperature of the liquid at the inlet is fixed to 25°C. A power of

[4]The development of a standard connector for micro-channel cooling is part of Work Package 9 of the AIDA2020 project.

6 W is dissipated on the silicon sensor surface immediately above the micro-channel cooling manifold.

Table 3.3: Physical and chemical properties of water and silicon used in the simulation: the density ρ, the constant pressure heat capacity C_p, the initial temperature T and the thermal conductivity κ.

Properties	**Water**	**Silicon**
ρ [kg/m^3]	997	2329
C_p [J kg^{-1}K^{-1}]	4181.3	713
T [K]	293	293
κ [W m^{-1}K^{-1}]	0.58	120

Results from a number of simulations with varying liquid flow are presented in Table 3.4. The liquid temperature at the outlet runs several degrees hotter than the inlet side. This reflects the heating of the liquid as it progresses through the manifold. The fourth column in Table 3.4 presents the simulated outlet temperatures. From these results one can calculate the heat absorbed by the cooling liquid:

$$\dot{Q}_a = \dot{m}\Delta C_p \Delta T, \tag{3.1}$$

where $\dot{Q}$ is the absorbed power, $\dot{m}$ the liquid mass flow, C_p is the constant pressure heat capacity of the liquid and ΔT is the water temperature difference between the inlet and the outlet. The efficiency ε of the simulated heat exchanger is obtained by comparing the absorbed power Q_a with the power absorbed by the liquid flow.

Table 3.4: The results of a number of simulations with different mass flow of cooling liquid. The first five parameters appear in Equation 3.1. The efficiency ε is defined as the ratio between the power $\dot{Q}$ absorbed by the coolant and the total applied power.

Dissipated power Q_d[W]	**Liquid mass flow $\dot{m}$[kg/s]**	**Inlet temp. T$_{in}$[K]**	**Outlet temp. T$_{out}$[K]**	**Absorbed power Q_a[W]**	**efficiency ε[%]**
5.82	6.98×10^{-5}	298	315.1	5.01	86
5.99	9.70×10^{-5}	298	312.0	5.69	95
6.12	1.29×10^{-4}	298	303.9	5.90	96
6.17	1.68×10^{-4}	298	306.5	5.96	97
6.19	2.06×10^{-4}	298	305.0	6.01	97
6.21	2.42×10^{-4}	298	304.0	6.07	98
6.23	2.72×10^{-4}	298	303.4	6.10	98
6.25	3.05×10^{-4}	298	302.8	6.14	98
6.25	3.45×10^{-4}	298	302.3	6.16	98
6.25	3.83×10^{-4}	298	301.9	6.18	99

Thanks to the simulation it is possible to rapidly evaluate the cooling performance

of different coolants. In Figure 3.18 the figure-of-merit[5] of several choices are compared. The lower, red curve in Figure 3.18 represent the situation of the laboratory measurement where water is used as a coolant. The upper, blue curve in the same figure is obtained when the water is replaced with an alcohol-water mixture (PWG6040).

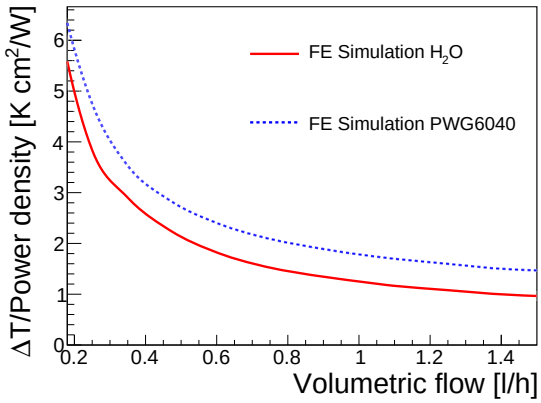

Figure 3.18: Finite element simulation results for the temperature gradient per unit power density as function of the volumetric flow of the coolant. The lower, red curve represent the situation of the laboratory measurement where water is used as a coolant. The upper, blue curve is obtained when the water is replaced with an alcohol-water mixture (PWG6040).

The cooling performance is somewhat degraded for most other choices for the coolant. The temperature gradient found in the simulation is in approximate agreement with a naive scaling by the ratio of heat capacities.

3.4.4 Thermo-mechanical performance

The prototype is tested in the lab to measure the temperature of the sensor surface as a function of the operational parameters, primarily the power consumption and liquid flow. The setup also monitors the position of the sensor with sub-μm precision.

The measurements are performed pure water as the cooling fluid. The measurements are representative for any mono-phase cooling system. The components to control and monitor the inputs, water flow, pressure and temperature at the inlet and outlet, are presented in Figure 3.19.

The water flow is established using a digital, variable-speed peristaltic pump (Stenner, SVP1). The flow can be regulated between a fraction of a litre per hour and several litres per hour. The maximum pressure the system can supply is 6 bars. To assure that there are no micro-particles which obstruct the micro-channels in the silicon ladder, a filter with a maximum particle size of 15 μm is inserted in the circuit. The liquid flow is measured using a flow meter and temperature sensors and pressure gauges are

[5]The figure-of-merit is defined as the temperature gradient divided by the power density dissipated in the sensor as a function of the volumetric flow of the coolant.

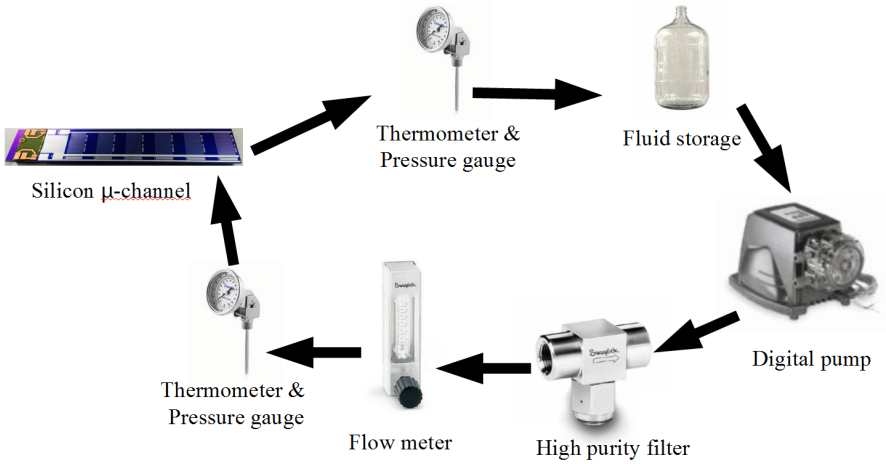

Figure 3.19: Schematic layout of the laboratory set up.

placed immediately before the inlet and after the outlet of the silicon ladder. All devices use standard SwageLock connectors. The only custom piece is the 3D printed connector to the micro-channel circuit.

The temperature profile of the sensor is monitored using a thermal infra-red camera with a field of view that includes the entire surface of the sensor. The temperature readings are calibrated to the readings of sensors in direct contact with the silicon (Pt100). The temperature calibration is applied as a global correction for the average emissitivity of the materials (silicon and aluminium). A more precise reading was obtained with the infra-red sensor focused to the hottest point of the silicon ladder.

Thermal performance

The cooling capacity of the micro-manifold integrated in the silicon is characterized in a series of measurements of the maximum temperature on the sensor surface. The measurement is repeated for a number of different settings of the pump speed, corresponding to a liquid flow ranging from a fraction of a litre/hour to 1.5 l/h, and for different values of the power dissipated in the end-of-ladder area. For all measurement the outlet of the cooling circuit is at atmospheric pressure and the ambient temperature between 23-25°C.

In Figure 3.20(a) the temperature gradient from the hottest point on the sensor to the coolant at the inlet of the micro-channel circuit is plotted as a function of liquid flow. The temperature difference is divided by the dissipated power because power is not exactly constant (as the resistance of the heaters on the silicon sensor depends on the temperature).

With a series of measurement at different power the maximum power for a given temperature gradient can be determined. An example is shown in Figure 3.20(b), where a maximum gradient of 10°C is allowed. At a liquid flow of 3 l/h, the integrated

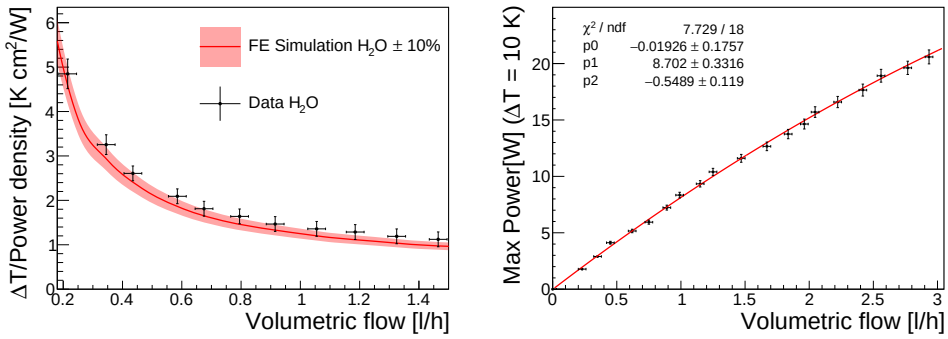

(a) (b)

Figure 3.20: (a) Temperature gradient of the hottest point on the sensor surface divided by the dissipated power density as a function of the water flow. The red curve corresponds to the values from a FE simulation and the shaded area shows a 10% error. Measured data are represented by the black dots with the error bars. (b) Dissipated power on the silicon ladder that yields a thermal gradient of 10°C for different liquid flow rates.

micro-channel circuit removes up to 20 W while maintaining the temperature gradient below 10°C. The curve is nearly linear over the interval of the measurements. While some sign of saturation is visible for the maximum flow rate, the derivative is still two thirds of that at the origin. This implies that the system is still not at its limit: a further increase of the liquid flow can provide further cooling power.

The pressure drop over the micro-channel cooling circuit is 1.5 bar when water flows at 3 l/h. The pressure drop is negligible (below 0.1 bar) at the smallest flow rate of 0.2 l/h.

In a more realistic situation also the sensor area itself dissipates power. For very long and thin sensors the heat transport towards the end-of-ladder area may lead to considerable temperature gradients. Apart from the 6 W at the end-of-ladder area a further 1.5 W is dissipated over the sensor area. Therefore now the micro-channel cooling is complemented with some air flow cooling, as Figure 3.21 shows.

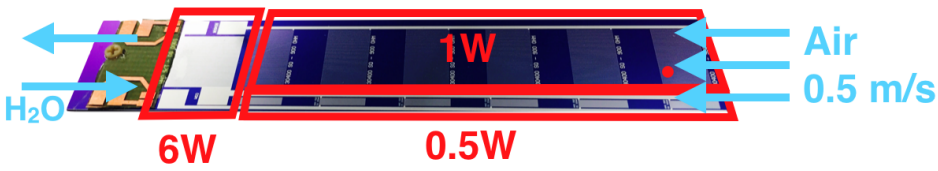

Figure 3.21: Schematic view of a fully powered silicon sensor. Red boxes indicate the regions where different powers are supplied. Blue arrows shown approximately the direction of the liquid (left) and air (right) flows.

Figure 3.22 shows the thermal performance as a function of the liquid flow. The two curves represent the temperature difference between the cooling liquid at the inlet and the hottest spot on the sensor surface. The hot spot is now found at the far end of the sensor. The blue curve, with liquid cooling only, shows how the temperature difference decreases by up to 25°C when the liquid flow is established. However, beyond a liquid flow of 0.5 l/h the cooling performance no longer improves significantly. A temperature gradient of 30°C remains.

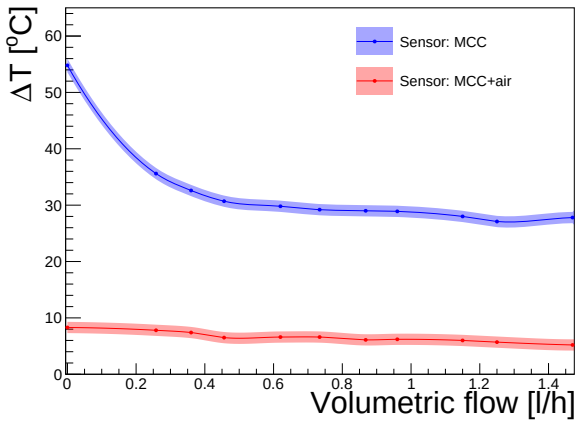

Figure 3.22: The temperature difference between the hottest spot on the sensor surface and the cooling liquid at the inlet of the micro-manifold. The blue, upper curve corresponds to the power dissipation as sketched in Figure 3.16, when cooling is through liquid flow only. The red, lower curve is obtained when a gentle air flow of 0.5 m/s is added, as shown in Figure 3.21.

The sensor area represents a much smaller power density than the end-of-ladder. Therefore, a gentle air flow is quite effective to remove the heat dissipated in the sensor. The red curve in Figure 3.22 shows the dramatic improvement in cooling performance when a gentle air flow of 0.5 m/s is established over the sensor surface. The maximum temperature difference with respect to the coolant at the inlet is 6-8°C, with a quite weak dependence on the liquid flow.

Mechanical impact

The mechanical impact of the micro-channel cooling is determined using the triangulating sensor mentioned in Section 3.3.2. To provide maximum sensitivity to deformations and vibrations, the sensor is supported only on one side, by the 3D printed connector. The distance sensor is placed close to the edge furthest away from the support, for the same reason. The sensor and support structure are placed on an optical table with pneumatic damping to isolate the system from external vibrations.

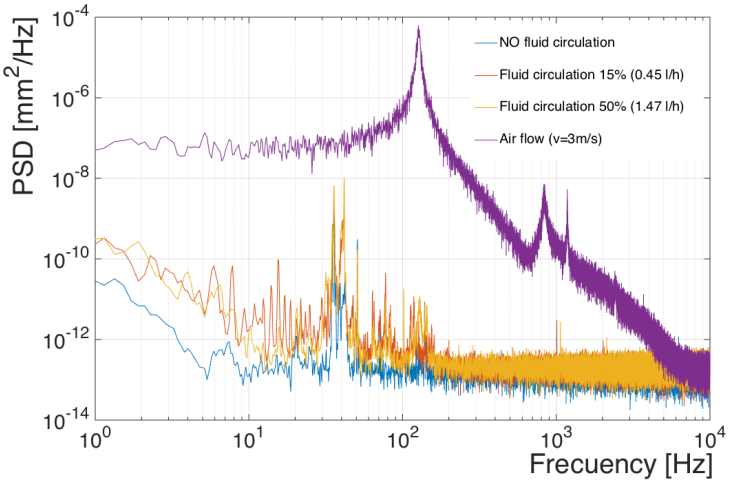

Figure 3.23: The spectral power density of four times series registered with the triangulating sensor: without any cooling (light blue), with a liquid flow of 0.45 l/h (red) and 1.47 l/h (yellow) and an air flow of 3 m/s (purple).

Several time series of the distance measurement are recorded under different conditions. The vibrations introduced by the background are measured without liquid flow. The peak-to-peak interval of all distance measurements for this null experiment is less than 0.7 μm. The RMS of the readings is 0.3 μm. When the measurement is repeated for the maximum liquid flow of 1.47 l/h the excursions increase only very slightly: the peak-to-peak interval is approximately 1 μm, the RMS increases to 0.4 μm. To check the sensitivity of the setup, the measurements were repeated with an air flow of 3 m/s. This induces very significant vibrations, with a peak-to-peak interval of 130 μm, demonstrating the sensitivity of the setup to vibrations.

The readings in the time domain were translated to the frequency domain using a FFT. The Power Spectral Density (PSD) is plotted in Figure 3.23 for frequencies ranging from a fraction of Hz to several kHZ. The eigenfrequency of the ladder (at 150Hz) is clearly visible in the spectrum corresponding to the air flow. The other spectra are quite close to the null spectrum, without air o liquid flow. The liquid flow induces very subtle vibrations, with sub-μm magnitude and frequencies in the 1-100 Hz domain.

3.5 Summary

Three key elements of the cooling strategy for low-mass silicon detectors are characterized.

Power pulsing

Power pulsing has been tested on silicon samples, both ladders and petals. The temperature gradient on the silicon surface is 1°C for an ILC duty cycle of 1 ms pulses separated by 200 ms. Less strict duty cycles can also offer a good cooling performance, the temperature gradients are under 10°C for 50/200 duty cycles and below. Due to the large thermal inertia of the own silicon, no rapid variations of temperature are observed, and an upper limit of 0.1°C is established.

Air flow cooling

Silicon samples have been characterized thermo-mechanically under the impact of an air flow. The cooling power of convective heat removal by an air flow has been demonstrated. An air speed of few m/s speed can dissipate approximately 85% of the heat of the petal. Mechanically the impact of the air flow starts to be significant for high velocities (6 m/s or higher) which produce amplitudes of vibrations bigger than 5 μm. The eigenfrequencies of a silicon petal in a single(double)-point clamping configuration have been extracted. A FE modal analysis reproduces accurately the measured values.

Integrated cooling channels

The cooling performance is measured by applying a power of up to 10 W on the surface of the silicon sensor immediately above the integrated cooling circuit. The absence of thermal barriers leads to very efficient removal of the dissipated heat. The temperature gradient from the hottest point on the sensor to the liquid can be kept below 2 K for a power density of 6 W/cm^2 and a liquid flow of 1 l/h, corresponding to a thermal figure-of-merit of close to 1. A finite-element simulation of the cooling circuit is able to reproduce the observed cooling performance, predicting the temperature gradient as a function of liquid flow and power dissipation to within 10%. The liquid flow has no significant impact on the mechanical stability of the sensor: the amplitude of vibrations is measured to be smaller than 1 μm, compatible with the null result when no liquid circulates. Recently, a cooling setup has been mounted at CERN to test the performance of a coolant known as C6F14. New measurements and simulations are on going.

These experiments show that the micro-channel cooling technique is the best locally, however the cooling power is degraded at far points from the channels manifold. Air cooling, as expected, dissipates the heat very efficiently but can lead to vibrations of several μm. Thus a combination of both cooling techniques might be a solution for a realistic detector. In areas with a large power density, where read-out chips and electronics are located, the integrated micro-channels offer the best solution. The remaining heat within the detector could be removed by a gentle air flow.

Chapter 4

Detector concepts, event generation, simulation and reconstruction

Detector simulations are needed for many reasons, to optimize full detector designs for physics performance on benchmark processes, to optimize the designs of subsystems and subdetectors, to compare proposed detector technologies with each other, to understand the effects of backgrounds on detector performance or establish a software infrastructure for the detector experiment(s). They are also used to study key benchmarks of the physics case in full detail, including subtle detector effects.

4.1 Detector concepts

4.1.1 ILC detectors

The ILC has been designed to host two experiments, the International Large Detector (ILD), presented in Section 2.4, and the Silicon Detector (SiD) [54]. The two detectors are shown in Figure 4.1. The ILC physics requires high-resolution jet energy reconstruction and di-jet mass performance. Event reconstruction techniques based on the Particle Flow Algorithm (PFA [67])[1] have been developed that can meet this challenge. Particle-flow reconstruction requires highly granular electromagnetic (ECAL) and hadron calorimeters (HCAL) and highly efficient tracking systems with a resolution of a few microns. Furthermore, flavour and quark-charge tagging will be available at an unprecedented level of performance as a result of the development of a new generation of high-resolution vertex detectors [57, 68]. Both detectors provide flexibility for operation at energies up to the TeV range. To preserve this unprecedented performance, the inner detectors must accommodate very low-mass detectors and supports, which is a significant challenge.

[1] A detailed explanation of the PFA technique is given in Section 4.2.3

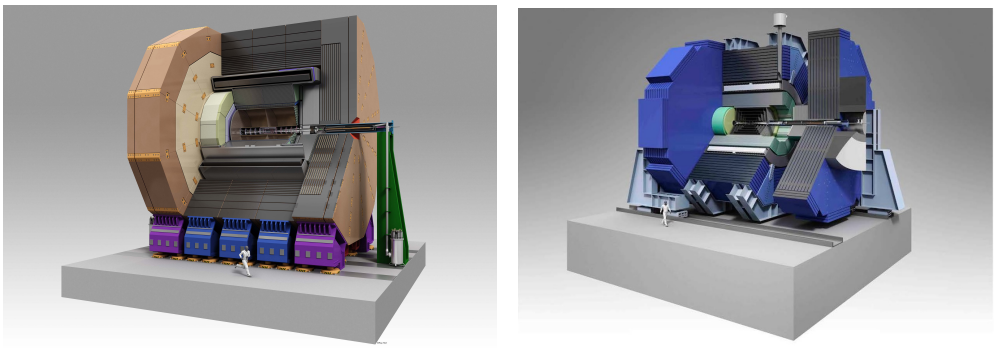

(a) (b)

Figure 4.1: Artistic views of the ILD (a) and SiD (b) detector concepts for ILC

Table 4.1 shows the main specifications of the baseline ILD and SiD detector concepts. Both detector designs are conceived as multi-purpose detectors, optimised for the broad range of physics opportunities at the ILC.

Table 4.1: Main specifications of the ILC detectors.

Experimental hall	Hall size	25 m x 142 m x 42 m (height)
Detectors	**The ILD detector in detail**	
	Height	~ 16 m
	Length	~ 14 m
	Weight	~ 14,000 tonnes
	Superconducting solenoid	3.5 teslas
	Vertex detector spatial resolution	3 μm
	Central tracker (TPC) spatial resolution	60 μm (220 layers)
	The SiD detector in detail	
	Height	~ 14 m
	Length	~ 11 m
	Weight	~ 10,100 tonnes
	Superconducting solenoid	5 teslas
	Vertex detector spatial resolution	< 5 μm
	Central semiconductor tracker spatial resolution	8 μm (5 layers)

SiD is a compact detector with a 5 T magnetic field and silicon tracking that provides spatial resolutions of the order of microns. The ILD is a larger detector with robust and stable performance over a wide range of energies. The concept is based on a tracking system formed by a TPC combined with silicon tracking for excellent efficiency and robust pattern-recognition performance. A granular calorimeter system provides very good particle-flow reconstruction in both concepts.

4.1.2 CLIC detectors

The general purpose ILD and SiD detector concepts [54], developed in the context of the 500 GeV ILC, form an excellent starting point for a detector design for CLIC. The modified versions of the ILD and SiD detector concepts were named CLIC_ILD and CLIC_SiD [53]. The main changes with respect to the ILC case are modifications of vertex detectors and very forward detector regions, to mitigate the impact of backgrounds, and increased hadron calorimeter depth.

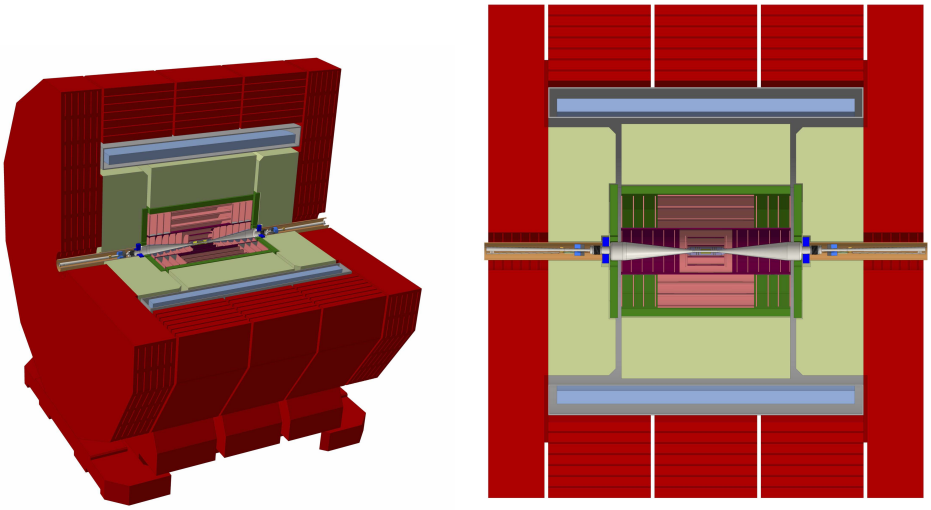

Figure 4.2: Artistic view (left) and transverse cross section (right) of the CLICdet.

Recently, a new model for the CLIC detector, shown in Figure 4.2, has been defined, based on the experience from various R&D activities linked to a future experiment at CLIC and lessons learnt after a series of simulation studies. The new detector model [69], called "CLICdet", has been designed for use in the next round of physics benchmark studies. An official technical document of the new CLIC detector is expected to be published soon.

The vertex detector has to reach a single point resolution of 3 μm and time stamping capabilities of better than 10 ns. The CLIC beam and background conditions are not favourable for a TPC+Silicon tracker, as planned in ILD. The vertex detector in CLICdet, similarly to the CDR detector models, consists of a cylindrical barrel detector closed off in forward direction by "disks". Transverse momentum resolution, angular track resolution and jet energy resolution using particle flow benefit from a larger tracker radius. Optimisation studies require an ECAL with finer longitudinal sampling. The magnet system of CLICdet consists of a superconducting solenoid producing a 4 T field in the centre of the detector, and a steel return yoke. Detector dimensions and weights are compared to the ILC concepts in Table 4.2.

Table 4.2: Key parameters of the CLIC detector concepts. CLIC_ILD and CLIC_SiD values are from the CDR [53].

Concept	CLICdet	CLIC_ILD	CLIC_SiD
Vertex inner radius [mm]	31	31	27
Tracker technology	Silicon	TPC/Silicon	Silicon
Tracker half length [m]	2.2	2.3	1.5
Tracker outer radius [m]	1.5	1.8	1.3
ECAL barrel r_{min} [m]	1.5	1.8	1.3
ECAL barrel Δr [mm]	202	172	139
ECAL endcap z_{min} [m]	2.31	2.45	1.66
ECAL endcap Δz [mm]	202	172	139
HCAL absorber barrel / endcap	Fe / Fe	W / Fe	W / Fe
HCAL λ_{I}	7.5	7.5	7.5
HCAL barrel r_{min} [m]	1.74	2.06	1.45
HCAL barrel Δr [mm]	1590	1238	1177
HCAL endcap z_{min} [m]	2.45	2.65	1.80
HCAL endcap Δz [mm]	1590	1590	1595
Solenoid field [T]	4	4	5
Solenoid bore radius [m]	3.5	3.4	2.7
Solenoid length [m]	8.3	8.3	6.5
Overall height [m]	12.9	14.0	14.0
Overall length [m]	11.4	12.8	12.8
Overall weight [t]	8100	10800	12500

4.2 Software

The detector concepts presented in Sections 4.1.1 and 4.1.2 use the `ILCSOFT` software framework which provides the core tools `LCIO` [70], `GEAR` [71], `MOKKA` [72] and `MARLIN` [73] as well as reconstruction and analysis tools for LC detector R&D. `LCIO` provides a hierarchical event data model and persistency and is used by all detector concepts for linear colliders, providing a basis for common software developments and the exchange of algorithms and tools. `GEAR` is an interface that provides the detector geometry information and material distribution at the reconstruction stage, including a detailed description of the sensitive and insensitive surfaces of tracking detectors. The `GEAR` software is going to be replaced in a near future by the `DD4HEP` toolkit [74] which provides a single source of detector information and an easier use. The `GEANT4` [75] package is used to provide a detailed simulation of the response of the detector. The `GEANT4` simulation of the ILD for ILC and the CLIC_ILD for CLIC use the `MOKKA` [72] program. `MOKKA` produces a list of generated particles and detector hits which are stored as SIO files [76] using the `LCIO` event data model. The use of a common data format enables the use of common particle flow and flavour tagging programs. `MARLIN` is the C++ application framework that is used for reconstruction algorithms of the simulated detector response and is based on `LCIO` and `GEAR`. `MARLIN` contains a plug-in mechanism that supports the modular development of user software packages. These packages are configured via an XML steering file with optional overwrite through command line arguments. A logging mechanism ensures that the actual configuration is stored for future reference and reproducibility.

This framework has been used for a massive Monte Carlo production for studies under realistic conditions at the ILC (TDR [48]) and CLIC (CDR [53]).

4.2.1 Event Generation

The Monte Carlo event samples are generated using the `WHIZARD` program [77]. Parton showering, hadronization and fragmentation is performed using the `PYTHIA` [78] program. The luminosity spectrum of ILC and CLIC is generated using `GUINEAPIG` [79], that is interfaced to `WHIZARD`. The effects of Initial State Radiation (ISR) are included in `WHIZARD`, with the ISR photons always being collinear with the incoming beam directions. `PYTHIA` is in charge of the Final State Radiation (FSR).

If unstable particles (e.g., W, Z, h, or t quarks) are present in the final state, `WHIZARD` assumes their natural width to be zero. Hence, processes like $e^+e^- \to W^+W^-$, $e^+e^- \to ZZ$, and $e^+e^- \to t\bar{t}$, are generated using a standalone version of `PYTHIA`. It is essential to include the background from $\gamma\gamma \to$ hadrons in order to study the detector performance under the most realistic conditions, as discussed in Section 4.2.4.

4.2.2 Full simulation of the ILD detector

The simulations of the ILD detector are based on the detector parameters presented in Sections 4.1.1 for ILC and 4.1.2 for CLIC. With a few relatively minor exceptions, the simulated detectors correspond closely to the global parameters of the engineering design. Physics studies of this thesis have been carried out with events subjected to a full simulation of the detector and subsequent event reconstruction using the detector model ILD_o1_v05 for ILC [54] and CLIC_ILD_CDR [53] for CLIC. All ILD (CLIC_ILD) sub-detectors in `MOKKA` have been implemented including a significant amount of engineering detail such as mechanical support structures, electronics and cabling as well as dead material and cracks. Where possible, sub-detectors have been implemented in a way that is agnostic to the actual readout technology, for others different implementations exist. Figure 4.3 shows a 3D view of the simulation model ILD_o1_v05.

4.2.3 Event Reconstruction

The `MARLIN` framework is used for the digitization, reconstruction, and analysis of events simulated with the ILD detector. The main steps in the reconstruction are: digitization of the simulated hits, TPC pattern recognition based on algorithms developed at LEP, track finding in the silicon detectors and merging of the silicon tracks with the TPC tracks. The tracking software is optimized to face the $\gamma\gamma \to$ hadrons background included for all generated events. The particle-flow reconstruction is performed using the PandoraPFA [67] event reconstruction package, producing a list of reconstructed Particle Flow Objects (PFOs).

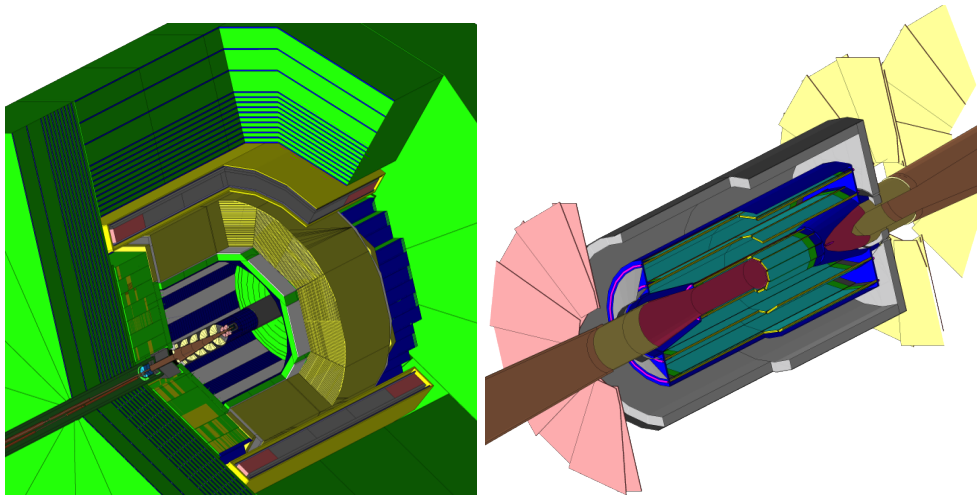

Figure 4.3: (Left) The ILD simulation model ILD_o1_v05 and (right) a zoom in on of the inner tracking detectors in the simulation model.

Digitization

The digitization of hits in the tracking detectors is performed by a parameterization of the point resolution as established by the R&D groups. In the case of the Si-Strip detectors inside the TPC and evolving in the Forward Tracking Disks, 1D TrackerHits are created at the digitization stage and then combined into 3D space points that are used for pattern recognition in order to correctly account for ghost hits. Calorimeter hits are scaled with a calibration factor according to the sampling fraction, where in the case of the semi-digital HCAL effects of cross talk between neighbouring cells are included.

Track reconstruction

The reconstruction of charged particles is done with a set of C++ packages. Clupatra is a TPC pattern recognition algorithm that combines topological clustering methods for seed finding with Kalman Filter based extrapolations for picking up hits [80]. Optionally the hit search can be extended inwards to include the Si-tracking detectors. FwdTracking is a newly developed pattern recognition for the FTD that is based on cellular automatons and Hopfield networks. The IMarlinTrK package provides the interface to the track fitter based on a Kalman Filter implemented using KalTest. SiliconTracking is a package for standalone tracking in VTX, SIT/SET and FTD. FullLDCTracking finally combines the track segments from all sub-detectors into a consistent final list of tracks which is then used as input to particle flow.

Particle Flow technique

Traditionally, jet energies have been measured by taking the sum of the energies deposited in the hadronic and electromagnetic calorimeters. The hadronic calorimeter, having a relatively poor energy resolution, was the limiting factor in the precision of the jet energy measurements. At the ILD, a highly granular calorimetry system will be used in conjunction with the tracking devices to measure the energy and momentum of every visible particle inside the detector. The energy of charged hadrons will be measured by the tracking detectors; the energy of photons will be measured by the electromagnetic calorimeter. The hadronic calorimeter is used only to measure the energy of neutral hadrons, as illustrated Figure 4.4(a). The reduced dependence on the hadronic calorimeter will lead to an unprecedented jet energy resolution at the ILD.

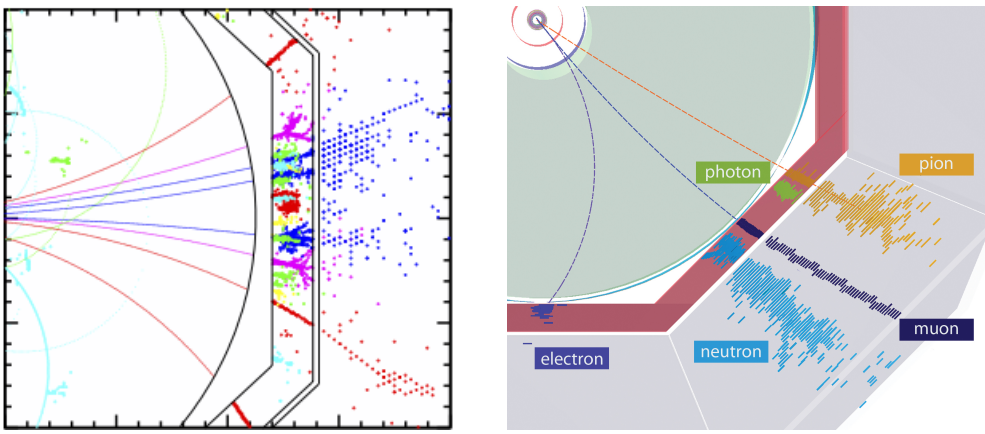

(a) (b)

Figure 4.4: (a) ILD: the highly granular calorimeters of ILD can identify the energy deposit of every visible particle. (b) Simulation of individual particles leaving the interaction region (top left) of a CLIC detector showing how different particles behave in the detector system.

On average, after the decay of short-lived particles, roughly 62% of the jet energy is carried by charged particles (mainly hadrons), around 27% by photons, only 10% of long-lived neutral hadrons and around 1.5% by neutrinos. Hence, approximately 90% of the jet energy is measured with the precision of the combined ECAL and tracker. Jet energy is typically $\gtrsim 55\%/\sqrt{\mathrm{E(GeV)}}$.

MarlinPandora is a `MARLIN` package that converts the calorimeter hit and track objects from `LCIO` objects into corresponding data structures used in PandoraPFA [81], augmented with relevant information from the detector geometry and with suitable track quality cuts applied, a visual example is shown in Figure 4.4(b). The resulting list of particle flow objects is then converted back into a list of ReconstructedParticles which is used for further analysis. PandoraPFANew (an implementation of PFA) uses sophisticated clustering algorithms and track-cluster matching as an initial step.

The application of re-clustering methods, based on cluster energy to track momentum comparisons, is crucial to eventually achieve the optimal jet energy resolution based on single particle reconstruction.

At the ILC, the di-jet mass reconstruction rely on the jet energy resolution of the detector. The goal for jet energy resolution at the ILC is that it is sufficient to cleanly separate W and Z hadronic decays. The resolution should then be comparable to their natural decay widths, around 3-4% over the entire jet energy range above 45 GeV.

The previous prescription of the jets composition leads to the following resolutions,

$$\Delta E_{\text{jet}}/E_{\text{jet}} \sim \frac{30\%}{\sqrt{E\ (\text{GeV})}} \oplus 3\% \tag{4.1}$$

and

$$\Delta E_{\text{lepton},\gamma}/E_{\text{lepton},\gamma} \sim \frac{18\%}{\sqrt{E\ (\text{GeV})}} \tag{4.2}$$

The use of a strong magnetic field and a large radius is favoured to separate depositions of charged particles from neutral ones. The calorimeters must be made of dense material to reduce the lateral size of the showers and thus minimize overlaps.

Vertex finding and jet flavour tagging

LCFIVertex [82] is a package for vertex finding and for jet flavour tagging. A complementary package, LCFIPlus, provides improved flavour tagging as well as new jet clustering algorithms for multi-jet final states (e.g. $t\bar{t}H \rightarrow 6$ or 8 jets). In Chapter 5, the performance of jet clustering algorithms in several benchmark studies is investigated. The secondary vertex finding is run centrally as part of the standard reconstruction, whereas jet finding and flavour tagging are run by the user, individually tuned according to the specific needs of the physics analysis.

4.2.4 Backgrounds

The main source of background are hits from e^+e^- pairs (incoherent pair production), resulting in considerable hit densities, predominantly in the VTX detector. However, fake tracks can be reduced very efficiently by requiring hits in the SIT, which provides an exact time stamp per bunch crossing (BX). Thus pair background is not overlaid for the Monte Carlo events.

The other source of background are multi-peripheral hadron events, coming from $\gamma\gamma \rightarrow$ hadrons processes. Figure 4.5(a) shows the polar angle distribution of this background, the distribution is clearly peaked in the most forward region of the detector, $|\cos\theta| \sim 1$. The pseudorapidity[2] distribution, shown in Figure 4.5(b), is roughly flat for the angular acceptance of the detector, $\eta < 3$ ($|\cos\theta| < 0.995$). This means that the particle density per unit rapidity is approximately constant. Therefore robust jet reconstruction algorithms are needed to deal with the $\gamma\gamma \rightarrow$ hadrons background

[2]Pseudorapidity or η is a parameter used in hadron colliders and is defined as $\eta = -ln\left(\tan\frac{\theta}{2}\right)$

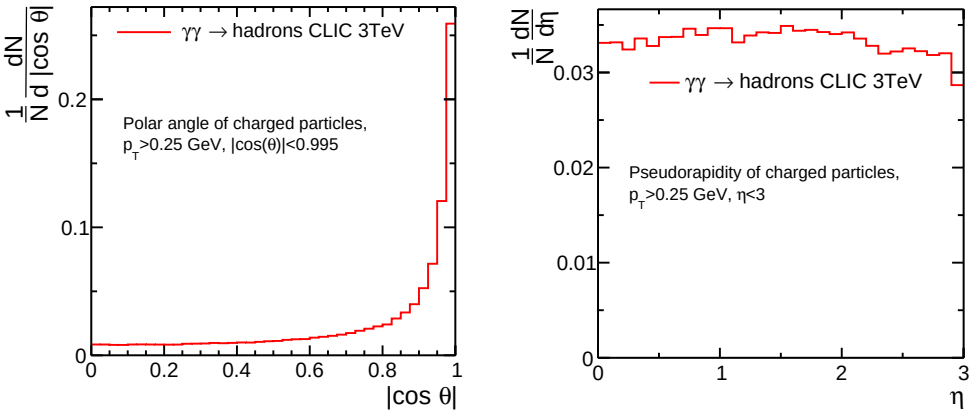

(a) Polar angle

(b) Pseudorapidity

Figure 4.5: (a) Polar angle distribution and (b) pseudorapidity of charged particles from $\gamma\gamma \rightarrow$ hadrons background in a CLIC 3 TeV environment, normalized to an integral of one event. Figures are based on the studies in Reference [83].

levels at future e^+e^- colliders. In Chapter 5 the performance of traditional e^+e^- jet algorithms is compared to more robust algorithms, as the longitudinally invariant k_t or the new VLC algorithm, in several benchmark analysis.

Background from $\gamma\gamma \rightarrow$ hadrons is included for most of the studies. The hits from simulated $\gamma\gamma \rightarrow$ hadrons events are added to those from the underlying simulated e^+e^- collision prior to digitization, track finding and particle flow reconstruction. In the case of ILC operating at 500 GeV, these give rise to a low occupancy, on average one expects 1.7 (4.1) $\gamma\gamma \rightarrow$ hadrons events per BX at nominal beam conditions for 500 GeV (1 TeV) [54]. The 554 ns bunch spacing at the ILC allows to distinguish single bunch crossings.

On the other hand, to mimic the 3 TeV CLIC train structure, the included background is restricted to 60 bunch crossings (BX) in a time window of -5 ns to $+25$ ns around the generated physics event, with a time of 0.5 ns in between two BX. For each BX, the number of $\gamma\gamma \rightarrow$ hadrons background events included is drawn from a Poisson distribution assuming a mean of 3.2 events per bunch crossing [53]. At 500 GeV and 1.4 TeV CLIC configurations, less background events per BX are expected. Table 4.3 summarizes the $\gamma\gamma \rightarrow$ hadrons background levels and the number BX overlaid to the signal.

Timing Requirements at CLIC

To operate with the 0.5 ns bunch spacing at CLIC, the subdetector systems must provide precise hit timing information in order to suppress the high levels of beam-induced background. The background suppression is based on time-stamping capabilities as-

Table 4.3: $\gamma\gamma \to$ hadrons background levels at ILC [54] and CLIC [84].

Collider@$\sqrt{s}$	**BX overlaid**	$\gamma\gamma \to$ hadrons / BX
ILC@500 GeV	1	1.7
ILC@1 TeV	1	4.1
CLIC@500 GeV	300	0.3
CLIC@1.4 TeV	60	1.3
CLIC@3 TeV	60	3.2

sumed to be 10 ns for all silicon tracking elements and a hit time resolution of 1 ns for all calorimeter hits.

However, simply imposing tight timing cuts at the hit level does not provide a viable solution. A two-stage approach is adopted. In the first stage, all raw detector hits in a 10 ns time window are used as input to the offline reconstruction. Here the combination of the high-granularity calorimeters and particle flow reconstruction allows hits from a single particle to be clustered together. The combined timing information of the calorimeter hits in a cluster allows a precise time to be assigned to each reconstructed particle.

Three levels of timing cuts are considered, *nominal*, *loose* and *tight* [85]. Figure 4.6 shows visually the impact on the reconstructed $\gamma\gamma \to$ hadrons background on a physics process, in this case 4.6(a) shows a $t\bar{t}H$, $H \to b\bar{b}$ event at 1.4 TeV where all particles are reconstructed whereas 4.6(b) shows the same event once tight cuts

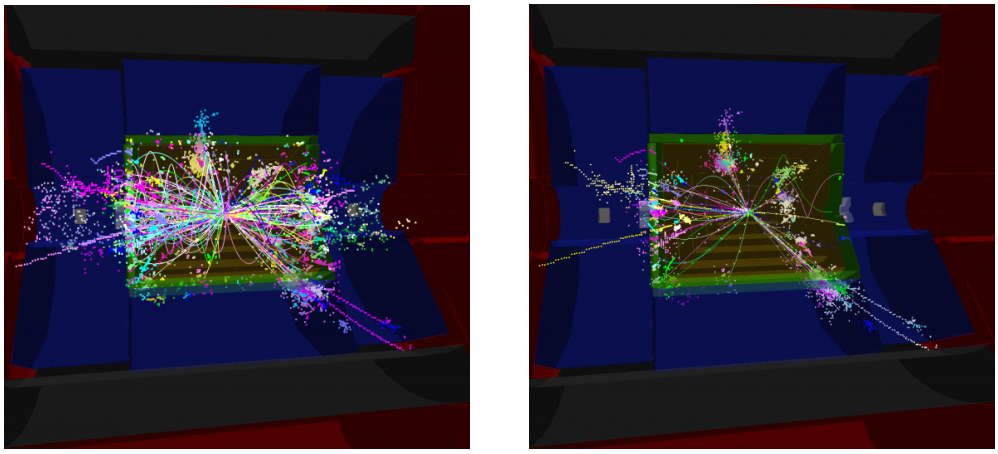

(a) All reconstructed particles

(b) Tight cuts

Figure 4.6: $e^+e^- \to t\bar{t}H$ event ($H \to b\bar{b}$ and semileptonic $t\bar{t}$ decay) at 1.4 TeV with $\gamma\gamma \to$ hadrons background overlaid. (a) All particles from the event are reconstructed. (b) A tight selection is applied for the background removal.

have been applied. This impressive level of background rejection is achieved without significantly impacting the detector performance.

4.3 Summary

The community involved in the linear collider projects ILC and CLIC has developed detailed detector designs. An extensive set of software packages exist that allow to generate, simulate and reconstruct events in full detail.

Chapter 5

Jet Reconstruction

Experiments at lepton and hadron colliders use jet algorithms to cluster the collimated sprays of particles that form in processes with asymptotically free quarks and gluons in the final state. The first modern jet algorithms (sequential recombination algorithms) were developed for e^+e^- colliders that operated at the Z-pole (a detailed historical account is found in Reference [86]). At the heart of the jet algorithm, and crucial to the definition of jets themselves, is a criterion to define the distance between two particles. In popular algorithms used at e^+e^- colliders the distance combines information on the angle between the particles and the energy of (the softest of the two) particles. Sequential recombination algorithm were adapted to the environment at hadron colliders in the early 1990s. At the LHC the large majority of analyses is based on inclusive jet reconstruction with the anti-k_t algorithm [87].

As mentioned in Chapter 2, future linear e^+e^- colliders can attain centre-of-mass energies from several 100 GeV to several TeV. Such machines present an environment that differs in several important respects from that encountered at the Z-pole and classical e^+e^- algorithms are no longer adequate.

In this chapter[1] the best known jet reconstruction algorithms are studied in order to explore which of them are most suitable for the e^+e^- colliders in several benchmark analyses with a centre-of-mass energy from 100 GeV to several TeV. A proposal of a new sequential jet reconstruction algorithm for future lepton colliders at the energy frontier is presented, the VLC algorithm [88, 90, 91]. It combines the natural distance criterion for lepton colliders with the greater robustness against backgrounds of algorithms adapted to hadron colliders.

5.1 Overview of jet reconstruction algorithms

The first modern clustering algorithm with a simple sequential recombination scheme algorithm is the JADE algorithm developed in the middle of the 1980's [92, 93]. The

[1] Results presented in this chapter are based on the studies by the author published in Reference [88]. These results were presented at international conferences, such as ICHEP 2014 [89]. A further publication [90] is in preparation in collaboration with the CERN CLICdp group.

distance y_{ij} assigned to any pair of particles i and j is given by:

$$y_{ij} = \frac{E_i^2 E_j^2}{Q^2}(1 - \cos\theta_{ij}) \tag{5.1}$$

where E_i and E_j denote the energy of the two particles, Q is the total energy of the event, and θ_{ij} is the angle between the two particles. At each step the algorithm merges the pair of particles with the smallest distance y_{ij}. This process continues until the smallest distance exceeds a value y_{cut} (*inclusive* clustering) or a previously defined number of jets is obtained (*exclusive* clustering).

In the Durham or e^+e^- k_t algorithm [94] used extensively at LEP and SLC the distance between particles i and j is modified to depend on the minimum of the energies E_i and E_j, rather than the product E_iE_j:

$$d_{ij} = 2min(E_i^2, E_j^2)(1 - \cos\theta_{ij}) \tag{5.2}$$

For sufficiently small angles the distance reduces to the transverse momentum squared of the softer particle relative to the harder one. The distance measure is thus proportional to the squared inverse of the splitting probability for one parton k into partons i and j in the soft and collinear limit.

Jet reconstruction at hadron colliders presents a number of additional difficulties. The incoming beams radiate gluons that can form jets. Only a fraction of the energy of the composite projectiles is transferred in the hard parton-parton process and a hadron remnant continues to travel down the beam pipe. An important consequence is that the system formed by the reaction products is typically not at rest in the laboratory frame[2]. Clustering algorithms were adapted to meet these challenges in the 1990s.

To cope with the boost along the beam direction, analyses at hadron colliders replace the particle energy E_i with its transverse momentum p_{Ti} and the angular distance between the particles $(1 - \cos\theta_{ij})$ with $\Delta R_{ij} = \sqrt{(\Delta\phi)^2 + (\Delta y)^2}$, where y denotes the rapidity. In the longitudinally invariant k_t algorithm [95, 96] the distance criterion is based on the same observables "to improve the factorization properties [of the algorithm] and [achieve] closer correspondence to experimental practice [...]" [95]. The generic inter-particle distance is rewritten as follows:

$$d_{ij} = min(p_{Ti}^{2n}, p_{Tj}^{2n})\frac{\Delta R_{ij}^2}{R^2} \tag{5.3}$$

where R is the radius parameter that determines the maximum area of the jet. Setting n in the exponent to 1 yields the longitudinally invariant k_t algorithm. Alternative choices of the exponent yield the Cambridge-Aachen algorithm (n =0), or the anti-k_t algorithm (n =-1), the default jet reconstruction algorithm at the LHC.

[2] For di-jet production at the LHC $\beta_z = v_z/c$ of the di-jet system is very close to 1 and even a massive system such as a top quark pair acquires a typical $\beta_z = 0.5$. In contrast, for processes such as $e^+e^- \to ZH(\gamma)$ (Higgsstrahlung) at $\sqrt{s} = 250$ GeV and $e^+e^- \to t\bar{t}(\gamma)$ at 500 GeV β_z is smaller than 0.1 in 95% and 90% of the events, respectively. The exception to the rule is the $2 \to 2$ process $e^+e^- \to f\bar{f}(\gamma)$, with f any fermion lighter than the Z-boson, where ISR (return-to-the-Z) plays an important role.

The second important modification of the algorithms is the addition of so-called *beam jets*, introduced in Reference [97]. Any particle with a beam distance $d_{iB} = p_{Ti}^{2n}$ smaller than any d_{ij} is not merged with any other particle, but is associated to the beam jet. These are not considered part of the visible final state. Thus, the soft, collinear radiation emitted by the incoming hadrons and the hadron remnant travelling in the very forward and backward direction is discarded.

Finally, one can add beam beam jets to the k_t algorithm for e^+e^- experiments. This yields an algorithm referred to as the generic e^+e^- k_t algorithm, with inter-particle distance:

$$d_{ij} = min(E_i^2, E_j^2)(1 - \cos\theta_{ij})/(1 - \cos R) \tag{5.4}$$

and beam distance given by $d_{iB} = E_i^2$.

5.2 The VLC algorithm

Background levels at hadron colliders form an important consideration in the design of jet algorithms. The *pile-up* of several tens of minimum bias events on each bunch crossing at the LHC is a serious challenge that has led to a large body of work on mitigation and correction methods. In comparison, previous lepton colliders, such as LEP or SLD, presented an environment with essentially negligible background. Future lepton colliders are in between these two extremes. While very far from the background levels of the LHC, detailed studies of the $\gamma\gamma \to hadrons$ background at the ILC or CLIC have shown a non-negligible impact on the jet reconstruction performance [53, 85]. Among several proposals to mitigate its effect, the use of the longitudinally invariant k_t algorithm, intended for hadron colliders, has led to the greatest improvement of the robustness [53].

The VLC jet algorithm maintains a Durham-like distance criterion based on energy and polar angle and can compete with the background resilience of the longitudinally invariant k_t algorithm. The algorithm has the following inter-particle distance:

$$d_{ij} = min(E_i^{2\beta}, E_j^{2\beta})(1 - \cos\theta_{ij})/R^2 \tag{5.5}$$

For β =1 the distance is given by the transverse momentum squared of the softer of the two particles relative to the harder one, as in the Durham algorithm. A distance based on energy and angle, as opposed to the transverse momentum and ΔR distance of hadron collider algorithms, remains the most natural choice for the e^+e^- colliders of the foreseeable future. Equation 5.5 provides a uniform inter-particle distance over the central and forward detectors and is in line with the natural choice of basis for the analyses at such a machine. Note that the meaning of the radius parameter R is redefined with respect to the generalized e^+e^- algorithm with beam jets. The R^2 in the numerator yields greater freedom than the $1-\cos R$, that is limited to the interval $[0, 2]$.

The beam distance of the VLC algorithm is:

$$d_{iB} = E^{2\beta} sin^{2\gamma}\theta_{iB}{}^{3} \tag{5.6}$$

where θ_{iB} is the angle with respect to the beam axis, i.e. the polar angle. In the default settings the two exponents β and γ are equal. For $\beta = \gamma = 1$ the expression simplifies to $d_{iB} = E^{2\beta} sin^{2\gamma}\theta_{iB} = p_{ti}^2$, i.e. the beam distance is given by the transverse momentum. The γ parameter governs the evolution of jet area with polar angle and is therefore a crucial parameter for the resilience to the forward-peaked $\gamma\gamma \to hadrons$ background (a more extensive discussion is found in Section 5.3). For application at the linear collider γ should be chosen equal to $|\beta|$. The β parameter allows to change the clustering order.

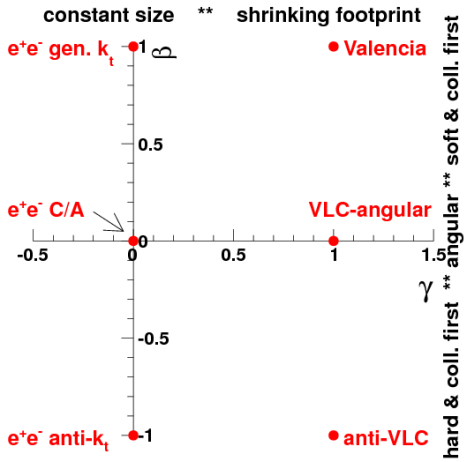

Figure 5.1: Diagram of the parameter space spanned by exponents β and γ of the VLC algorithm.

For $\beta = 1$ clustering starts with soft, collinear radiation. Choosing $\beta = 0$ yields purely angular clustering, while β = -1 corresponds to clustering starting from hard, collinear radiation. These integer choices of β correspond to k_t, Cambridge-Aachen and anti-k_t clustering. Non-integer values of β allow to interpolate smoothly between these three schemes. The exponent γ in the exponent of the beam distance of the VLC algorithm provides a handle to control the shrinking of the jet catchment area in the forward and backward regions of the experiment. We have seen that $\gamma = 1$ yields forward jets with a similar size of those of the longitudinally invariant algorithms for hadron colliders. Values of γ greater than 1 further enhance the rise of the d_{ij} ratio in the forward region, causing the jet footprint to shrink faster. Values between 0 and 1 yield a slower decrease of the area when the polar angle goes to 0 or π. For

[3] For $\beta = 1$ this combination of inter-particle and beam distance metrics is similar to that of the $k_\perp$ algorithm proposed in Reference [97], with the difference that $d_{iB} = p_{ti}^2 = E_i^2 \sin^2\theta_{iB}$, whereas in Reference [97] it was given by $2E_i^2(1 - \cos\theta_{iB})$.

$\gamma = 0$, $d_{iB} = \mathrm{E}^{2\beta}$, the generalized e^+e^- algorithms with constant angular opening are retrieved. A schematic overview of the algorithms in (β, γ) space is given in Figure 5.1.

The VLC algorithm is available as a plug-in for the FastJet [98, 99] package[4]. Recently, the VLC algorithm has been included as a jet algorithm in the MarlinFastjet package of the last ILCSOFT release v01-17-10[5].

5.3 Comparison of the distance criteria

The choice of distance criterion defines the essence of the jet algorithm and has profound implications on its performance in a given environment. The differences between the various algorithms are most easily visualized as follows. The distance between two test particles with an energy of 1 GeV emitted at a fixed relative angle of 100 mrad is calculated. The leftmost plot in Figure 5.2 shows how the distance between the two particles evolves as the system is scanned from the central detector ($\cos\theta = 0$) to the forward region ($\cos\theta = 1$).

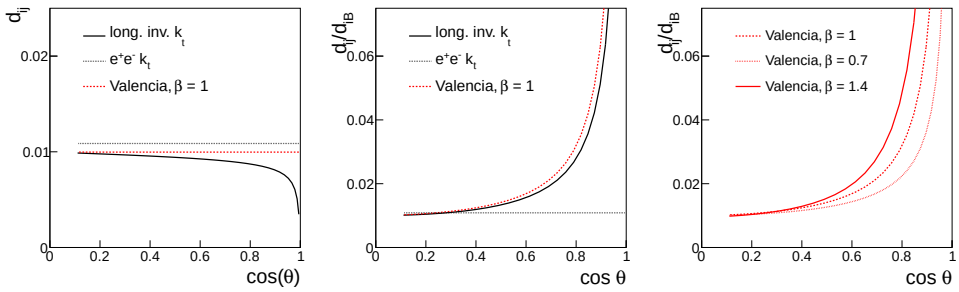

Figure 5.2: The dependence of the inter-particle distance d_{ij} of two test particles emitted at fixed angular distance and the ratio of d_{ij} to the beam distance d_{iB} with the polar angle θ. Results are presented for several clustering jet reconstruction algorithms discussed in the text.

The distance d_{ij} of the generic e^+e^- k_t algorithm is independent of polar angle, as shown in Figure 5.2. The same holds for the VLC algorithm proposed here, but generally not for algorithms used at hadron colliders. Two effects come into play. For two particles separated by a given polar angle, the pseudo-rapidity difference $\Delta\eta$ grows larger in the forward region. At the same time the distance between two particles with energy E decreases as p_T is reduced. The net effect for the k_t algorithm is a sharp decrease of the distance in the forward region.

The relation between the inter-particle distance d_{ij} and the beam distance d_{iB} governs the relative *attraction* of beam jets and final-state jets and is therefore a crucial property for the performance in environments with significant background. The ratio $\frac{d_{ij}}{d_{iB}}$ is shown as a function of polar angle in the central plot in Figure 5.2. As might be

[4]The code can be obtained from the "contrib" area under https://fastjet.hepforge.org/contrib/
[5]http://forum.linearcollider.org/index.php?t=treegoto=2393rid=6

expected from the functional form in Equation 5.4, the ratio is flat for e^+e^- algorithms (Durham). For the longitudinally invariant k_t algorithm, on the other hand, the ratio rises steeply in the forward region. For the VLC algorithm with $\beta = 1$ we obtain very similar behaviour to the longitudinally invariant k_t algorithm.

The steep rise in $\frac{d_{ij}}{d_{iB}}$ at $\cos\theta \sim 1$ penalizes relatively isolated particles in the forward and backward directions, that are likely due to background processes. The exponent β introduced in the VLC algorithm gives a handle to enhance or diminish the increase of the $\frac{d_{ij}}{d_{iB}}$ ratio in the forward region, as shown in Figure 5.2. Thus, we have a handle to *tune* the background rejection that is independent of the parameter R that governs the jet radius.

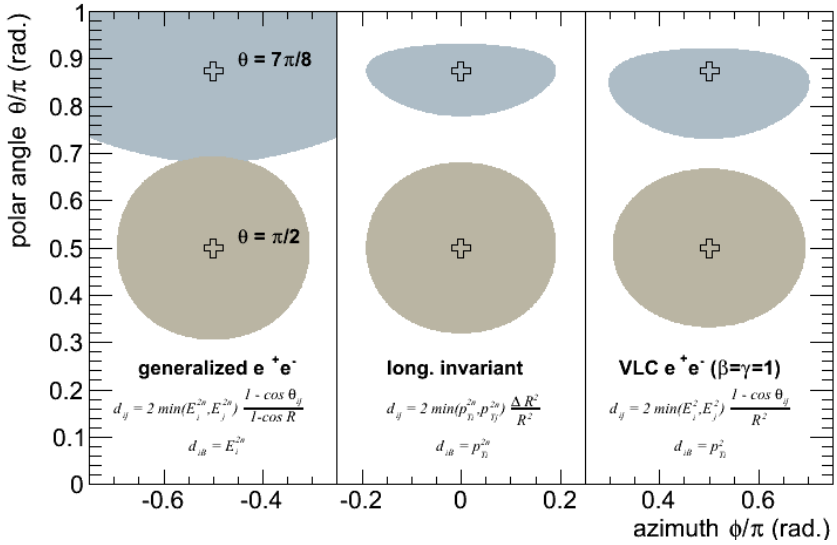

Figure 5.3: The area or footprint of jets reconstructed with $R = 0.5$ with the three major families of sequential recombination algorithms. The two shaded areas in each column correspond to a jet in the central detector ($\theta = \pi/2$) and to a forward jet ($\theta = 7\pi/8$).

The footprints of jets reconstructed with the most important families of sequential clustering algorithms are given in Figure 5.3. The leftmost column in Figure 5.3 generalizes the classical e^+e^- algorithms for lepton colliders, such as Durham ($n = 1$) and Cambridge-Aachen ($n = 0$), by adding a beam distance and radius parameter. The formula in the central column presents the longitudinally invariant algorithms discussed before. The third column corresponds to the VLC algorithm with $\beta = \gamma = 1$. For each of the algorithms the catchment areas of a central and forward jet with $n = 1$ and $R = 0.5$ are indicated in Figure 5.3. The footprint of the central jet (at $\theta = \pi/2$) is approximately circular for all algorithms. The area of the jet in the forward detector (at $\theta = 7\pi/8$) shrinks considerably for the longitudinally invariant algorithms and the VLC algorithm. The reduced exposure in this region where backgrounds are most pronounced is the crucial feature for the enhanced resilience of these algorithms.

A comparison of the shape of the footprint of the longitudinally invariant algorithms and the VLC algorithm show that, given identical jet axes, the former extend further into the forward region. This feature explains some of the differences in performance observed in the following Sections.

5.4 Monte Carlo simulation

The performance of the different algorithms is compared for a number of benchmark processes, such as $t\bar{t}$, ZZ or Higgs boson pair production at a linear e^+e^- collider with $\sqrt{s}$ = 500 GeV, 1.4 TeVand 3 TeV. Samples are generated with WHIZARD and the response of the ILD detector is simulated with GEANT4. More details about the event generation and full simulation of the detector can be found in Section 4.2.

The background considered in these studies is due to multi-peripheral $\gamma\gamma \rightarrow hadrons$ production. These background events are overlaid on the signal using a mechanism similar to that used for pile-up at the LHC, as explained in Section 4.2.4. In the CLIC studies particle flow objects are selected using the set of timing cuts corresponding to the *nominal*, *loose* and *tight* selection.

5.4.1 Top quark pair production at a 500 GeV ILC

The performance of several jet algorithms in the study of $t\bar{t}$ production at the ILC presented in Chapter 6 is evaluated in this section. The Monte Carlo sample includes all six-fermion processes that produce a "lepton + jets" final state: $e^+e^- \rightarrow b\bar{b}l^{\pm}\nu_l q\bar{q}'$.

Reconstruction of the event involves charged lepton reconstruction and removal of the corresponding energy, the reconstruction of exactly four jets (exclusive jet clustering with $N = 4$) and flavour tagging, described in detail in Reference [100]: The two jets with the poorest score in the b-tagging algorithm are combined to form the W-boson candidate. The hadronic top candidate is constructed by adding the remaining (b-)jet that minimizes a χ^2 based on the hadronic top quark candidate mass and energy, the b-jet energy in the top quark rest frame and the angle between W-boson and b-quark.

Four jet reconstruction algorithms are considered: the Durham algorithm, the generic e^+e^- k_t algorithm with beam jets with $R = 1$, the longitudinally invariant k_t algorithm with $R = 1.5$ and the VLC algorithm with R =1.2 and $\beta = 0.8$, $\gamma = 1$. The choice of parameters corresponds to the optimal setting determined in a scan over a broad range of parameters. The resolution of the measurements of the energy of the four jets, of the energy and mass of the hadronic W-boson and hadronic top quark candidate are given in Table 5.1.

The results show a clear advantage of the algorithms with a d_{ij}/d_{iB} ratio that increases in the forward and backward region of the experiment. Even with the rather modest background level at the ILC the longitudinally invariant k_t algorithm and the VLC algorithm achieve a 10-15% better resolution than the classical e^+e^- algorithms.

Table 5.1: The Root Mean Square of the central 90% of the events (RMS90) for five observables reconstructed in $t\bar{t}$ events at a 500 GeV ILC: the energy of the system formed by the four jets, the energy and mass of the hadronic W-boson and the energy and mass of the hadronic top quark.

ILC $\sqrt{s}$ = 500 GeV, $\gamma\gamma \to$ *hadrons* overlaid					
RMS$_{90}$ [GeV]	**E_{4j}**	**E_W**	**m_W**	**E_t**	**m_t**
Durham	23.2	19.6	20.3	19.5	21.4
e^+e^- k_t	25.6	20.8	21.6	20.5	22.8
long. inv. k_t	21.7	18.4	18.9	18.4	20.1
VLC	21.4	18.0	18.8	18.2	20.0

5.4.2 Di-boson production at CLIC at $\sqrt{s}$ = 500 GeV

The $e^+e^- \to ZZ$ process is studied in the CLIC environment at $\sqrt{s}$ = 500 GeV to enable comparison with the first detailed studies of the impact of background on jet reconstruction at CLIC in Reference [85] and the CLIC CDR [53].

Only $e^+e^- \to ZZ \to q\bar{q}q'\bar{q}'$ events are selected. Events with Z-bosons emitted in the very forward direction (with polar angle $|\cos\theta| > 0.99$), where the beam pipe may have a profound impact are discarded, as well as events where the Z-bosons are very far from their mass shell ($|m(q\bar{q}) - m_Z| > 30$ GeV. Exactly four jets are reconstructed and the di-jet combinations are selected that minimize the following χ^2:

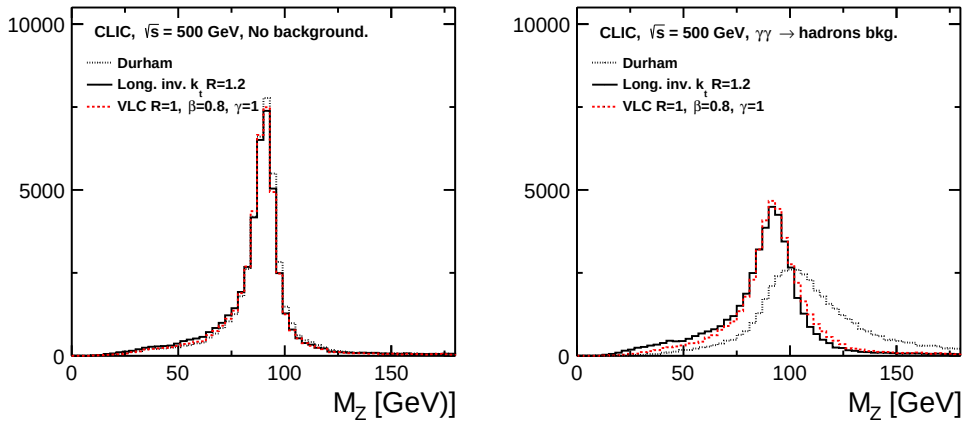

Figure 5.4: The reconstructed Z-boson mass distribution for $ZZ \to q\bar{q}q'\bar{q}'$ events at a 500 GeV CLIC. No backgrounds are added in the leftmost plot. The results on the rightmost plot correspond to the same events with the $\gamma\gamma \to$ *hadrons* background corresponding to 300 bunch crossings overlaid on the signal, where each bunch crossing contains approximately 0.3 $\gamma\gamma \to$ *hadrons* events. No PFO timing cuts are applied.

$$\chi^2 = \frac{(E_{Z1} - E_{Z2})^2}{(250\ \text{GeV})^2} + \frac{(m_{Z1} - m_{Z2})^2}{(91\ \text{GeV})^2} + \frac{\angle(Z_1, Z_2)}{(\pi)^2}.$$

The Z boson candidate mass distribution is shown in Figure 5.4 for the parameters that yield the best performance: $R = 1.2$ for longitudinally invariant k_t, $R = 1$, $\beta = 0.8$, $\gamma = 1$ for the VLC algorithm. Numerical results are given in Table 5.2.

Table 5.2: The centre and width - from a Gaussian fit - of the reconstructed Z-boson mass peak in ZZ events at a 500 GeV CLIC. The third column lists the RMS_{90}.

CLIC $\sqrt{s} = 500$ GeV, no background overlay			
[GeV]	$\mathbf{m_Z}$	$\sigma_\mathbf{Z}$	$\mathbf{RMS_{90}}$
Durham	90.6	5.4	13.8
long. inv. k_t	90.4	5.3	14.3
VLC	90.3	5.2	12.5
CLIC $\sqrt{s} = 500$ GeV, 0.3 $\gamma\gamma \to$ *hadrons* events/BX			
[GeV]	$\mathbf{m_Z}$	$\sigma_\mathbf{Z}$	$\mathbf{RMS_{90}}$
Durham	101.1	13.6	28.8
long. inv. k_t	92.0	9.0	17.2
VLC	92.5	9.2	16.2

In the background-free case all three algorithms achieve a narrow Z-boson mass peak. The impact of the overlaid background is rather pronounced for the Durham algorithm. The peak position shifts by approximately 10 GeV and broadens considerably. Both the longitudinally invariant k_t algorithm and the VLC algorithm show considerably better performance under these conditions.

5.4.3 Higgs pair production

The study of Higgs boson pair production is crucial to assess the strength of the Higgs self-coupling. The analysis is very challenging at both hadron and lepton colliders due to the very small cross section. At an e^+e^- collider the potential for this measurement is enhanced at large centre-of-mass energy, as the production rate (in the vector-boson-fusion channel $e^+e^- \to \nu\bar{\nu}hh$) grows strongly with centre-of-mass energy. In this section, events where both Higgs bosons decay to hadrons, through the dominant branching $h \to b\bar{b}$ of the SM Higgs boson are the focus. This final state can be isolated [101] provided the four jets are reconstructed with excellent energy resolution. The challenge of this measurement lies in the fact that both Higgs bosons are typically emitted at small polar angle [102]. The most frequently observed topology has both Higgs bosons emitted in opposite directions: one in the forward direction and the other in the backward direction. At 3 TeV (at least) one of the Higgs bosons is

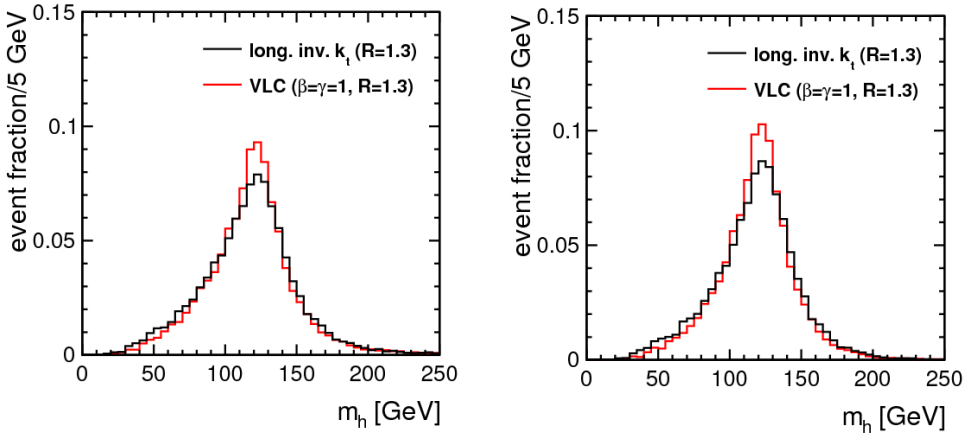

Figure 5.5: The reconstructed di-jet mass distribution for fully hadronic decays of $e^+e^- \to \nu\bar{\nu}hh$, $h \to b\bar{b}$ events at a 3 TeV CLIC. In the left panel all Higgs boson candidates are included, in the right panel only those that match onto exactly two b-quarks from Higgs boson decay. The nominal level of $\gamma\gamma \to hadrons$ background is overlaid on the signal. Particle flow objects are selected using the tight selection.

emitted with $|cos\theta| > 0.9$ in approximately 85% of events. In this area of the detector the background level due to $\gamma\gamma \to hadrons$ production is most prominent.

Despite the large centre-of-mass energy the Higgs bosons are produced with rather moderate energy: in 3 TeV collisions the most probable energy of the Higgs bosons is approximately 200 GeV, with a long, scarcely populated tail extending to 1.5 TeV. The modest Higgs boost is sufficient for the b-quarks to continue in the same hemisphere as their parent Higgs boson, but it is nearly almost insufficient to form the collimated final state observed for the top quark decays of next Section 5.4.4. Jet reconstruction is exclusive with $N_{jets} = 4$. Higgs boson candidates are reconstructed by pairing two out of the four jets. The combination is retained that yields the best di-jet masses

Table 5.3: Response and resolution of the di-jet mass distributions obtained with the k_t and VLC algorithms in the left panel of Figure 5.5. Results are presented for the median response and two estimates of the resolution: the 34% inter-quantile range (IQR_{34}) and the RMS of central 90% of jets.

CLIC $\sqrt{s} = 3$ TeV, tight PFO selection			
algorithm	**median [GeV]**	**IQR_{34} [GeV]**	**RMS_{90} [GeV]**
long. inv. k_t ($R = 1.3$)	118.5	30.1	24.3
VLC ($R = 1.3, \beta = \gamma = 1$)	118.9	27.1	22.0

(i.e. that minimizes $\chi^2 = (m_{ij} - m_h)^2 + (m_{kl} - m_h)^2$, where m_{ij} and m_{kl} are the the masses of the two di-jet systems and $m_h = 126$ GeV is the nominal Higgs boson mass). The reconstructed mass of both di-jet systems forming the Higgs boson candidates is histogrammed in Figure 11. The results of two algorithms are shown, both with the radius parameter R set to 1.3. The red line denotes the result of the VLC algorithm with $\beta = \gamma = 1$, the black line that of the longitudinally invariant k_t algorithm. Numerical results of the centre and width of the reconstructed di-jet mass distribution are presented in Table 5.3.

The response of both algorithms is found to agree to within 0.5%, for all methods to estimate the central value of the distribution. The Higgs mass resolution obtained with the VLC algorithm is significantly better with all figures of merit. The IQR_{34} divided by the median yields 22.6% for the VLC algorithm versus 25.4% for k_t.

5.4.4 Boosted top quarks at high-energy CLIC stages

The last benchmark analysed is pair production of boosted top quarks at a multi-TeV e^+e^- collider. At these energies, both 1.4 TeV and 3 TeV, the top quark decay products are so collimated that hadronic top quarks can be reconstructed as a single large-R top-jet ($R \sim 1$). Only the fully hadronic final state $e^+e^- \to t\bar{t} \to b\bar{b}q\bar{q}'q''\bar{q}'''$ is considered and events where either the top or anti-top quark is emitted in the most forward or backward direction are discarded.

Boosted top quark pairs at 3 TeV

To cope with the increased background at 3 TeV the tight PFO selection is applied. Jets are reconstructed with exclusive ($N = 2$) clustering with $R = 1.2$. In each case the same algorithm is also run on all stable Monte Carlo particles, including neutrinos, but excluding the $\gamma\gamma \to$ hadrons background.

The jet invariant mass distribution for the longitudinally invariant k_t and the VLC algorithm are presented in Figure 5.6. In the leftmost panel, that corresponds to $t\bar{t}$ events without background overlay, both algorithms are seen to reconstruct a narrow peak close to the top quark mass. The long tail toward large mass is due to radiation off the top quark and its decay products and is also present in the jets reconstructed on stable MC particles.

To measure the performance, a comparison between the jet reconstructed on particle flow objects and the jet found by the same algorithm on the stable particles from the signal event (i.e. excluding the $\gamma\gamma \to$ hadrons) is established.

The jet mass measurement is known to be very sensitive to background [103]. A quantitative summary is presented in the second part of Table 5.4. The bias on the jet mass without background is sub-% for most algorithms. The resolution of the VLC and longitudinally invariant k_t algorithms is significantly better than that of the classical e^+e^- algorithms. The 4.1% jet mass resolution is a testimony to the potential of highly granular calorimeters and particle flow reconstruction for jet substructure measurements. The $\gamma\gamma \to$ hadrons background has a profound effect on the performance. The performance of the classical algorithm is clearly inadequate, with a strong bias and a severe degradation even with the tight PFO selection. The

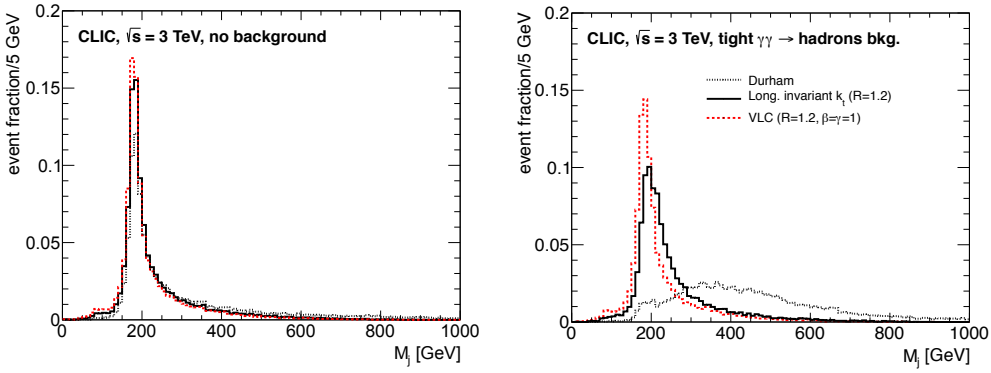

Figure 5.6: The reconstructed jet mass distribution for fully hadronic decays of $t\bar{t}$ events at a 3 TeV CLIC. No backgrounds are added in the left plot. In the righ plot 60 bunch crossings of $\gamma\gamma \to$ hadrons background are overlaid on the signal and particle flow objects are selected using the tight selection.

VLC and longitudinally invariant k_t algorithms are much less affected, as expected from the smaller exposed area. The VLC algorithm is found to be more resilient than longitudinally invariant k_t.

Table 5.4: The bias and resolution of the energy and mass measurements of reconstructed top jets. All results are obtained by comparing the jet energy reconstructed on particle flow objects to the jet of stable MC particles from the signal event. The performance of the classical e^+e^- algorithm is such that the figures-of-merit cannot be estimated reliably under nominal background conditions (indicated by "-" entries in the Table).

CLIC $\sqrt{s} = 3$ TeV, energy resolution (no bkg./tight/nominal)									
	median [GeV]			IQR_{34} [%]			RMS_{90} [%]		
Durham	-0.9	3.1	-	4.6	6.6	-	3.7	5.7	-
generic $e^+e^-k_t(R=1)$	-0.3	0.5	-	3.4	4.0	-	2.7	3.4	-
long. inv. $k_t(R=1.2)$	-0.2	0.4	1.8	3.1	3.2	3.4	2.5	2.7	2.8
VLC $(R=1.2)$	-0.2	-0.2	0.5	3.1	3.2	3.2	2.5	2.6	2.6
CLIC $\sqrt{s} = 3$ TeV, mass resolution (no bkg./tight/nominal)									
	median [GeV]			IQR_{34} [%]			RMS_{90} [%]		
Durham	-1.0	37.7	-	14.3	-	-	11.7	33.8	-
generic $e^+e^-k_t(R=1)$	0.5	4.7	-	5.1	23.2	-	4.6	17.0	-
long. inv. $k_t(R=1.2)$	1.1	8.0	21.2	4.1	12.0	20.6	3.5	9.9	16.3
VLC $(R=1.2)$	0.8	1.7	5.6	4.1	7.1	9.4	3.5	6.0	8.0

Trimming algorithm for boosted tops at 1.4 TeV

Boosted top quarks are distinguished from background (W, Z and Higgs jets in the case of a multi-TeV lepton collider) by revealing the substructure of jets [104]. A broad range of new techniques developed for the LHC have so far remained unexplored. This is particularly true for a set of of tools that has proven extremely powerful in pile-up mitigation and correction in ATLAS and CMS. Jet grooming (the collective name for (mass-drop) filtering [105], pruning [106] and trimming [107]) effectively reduces the exposed jet area to several small regions with large energy flow. This provides an effective means of capturing a large fraction of the jet energy while reducing the impact of soft contamination.

This work is based on the trimming technique Reference [107]. Instead of the standard "outside-in" procedure where a seed jet is reclustered using a subjet finding method, the "inside-out" procedure is used, where small subjets are found first and clustered into a larger jet. An example of the "inside-out" procedure is found in [108].

Porting jet trimming and jets-from-subjets strategies to the LC environment compared to LHC applications present a number of changes. As the centre-of-mass energy is well known, the threshold can be fixed to a number in the range 2-20 GeV, instead of using a threshold expressed a fraction of the jet p_T. Subjets accomplishing the energy cut must be small (with R values between 0.1-0.5). The algorithms use a distance criterion based on energy and angle, this can be either a robust algorithm (VLC) or the generalized e^+e^- algorithm. The large-R jet algorithm is run in exclusive mode to obtain a fixed number of jets, two jets in this particular case.

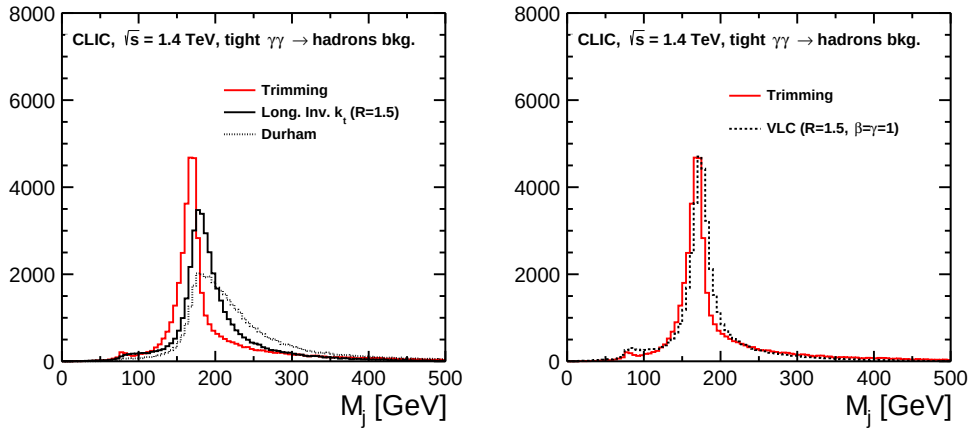

Figure 5.7: The reconstructed jet mass distribution for fully hadronic decays of $t\bar{t}$ events at a 1.4 TeV CLIC. $\gamma\gamma \rightarrow$ hadrons background are overlaid on the signal and particle flow objects are selected using the tight selection. The red continuous line corresponds to the jet mass distribution when the trimming technique is used.

Following, tests of the trimming algorithm in a 1.4 TeV CLIC environment are presented. First of all, a scan over a broad range of $R_{subjets}$ and E_{cut} parametres

is performed in order to determine the optimal setting. Additionally, different jet algorithms for e^+e^- colliders were tested. The best jet reconstruction performance resulted for the ee_genk_t algorithm with $R_{subjets} = 0.4$ and an energy threshold of $E_{cut} = 5$ GeV.

The reconstructed mass of the large-R jet for Durham, longitudinally invariant k_t and VLC algorithms is presented in Figure 5.7. Each plot compares the measured mass using the trimming technique versus the mass from a direct reconstruction of the jet. As expected, trimming reduces the background contamination and improves the resolution. The classical e^+e^- algorithm and longitudinally invariant k_t cannot deal with the background levels of a multi TeV collider, both measurements are degraded when the trimming technique is not run. On the other hand, the direct jet reconstruction with VLC algorithm gives a narrower peak distribution similar to the one obtained with the subjets strategy. Quantitative results are presented in Table 5.5. As before, the bias is measured as the median and the resolution is evaluated through the RMS_{90} and the IQR_{34}, comparing the jet energy reconstructed on particle flow objects to the jet of stable MC particles from the signal event.

Table 5.5: The bias and resolution of the energy and mass measurements of reconstructed top jets for two configurations: *direct* refers to the direct reconstruction of two jets while *trimming* corresponds to those cases where the trimming algorithm is used. All results are obtained by comparing the jet energy reconstructed on particle flow objects to the jet of stable MC particles from the signal event.

CLIC $\sqrt{s} = 1.4$ TeV, energy residual, tight selection (direct/trimming)			
	median [GeV]	IQR_{34} [%]	RMS_{90} [%]
Durham	-5.5 / -14.7	7.1 / 4.3	5.4 / 3.7
long. inv. $k_t(R = 1.5)$	-2.0 / -10.5	3.2 / 3.1	2.2 / 2.7
VLC ($R = 1.5$)	-6.4 / -10.1	3.1 / 3.1	2.2 / 2.3
CLIC $\sqrt{s} = 1.4$ TeV, mass residual, tight selection (direct/trimming) [%]			
	median [GeV]	IQR_{34} [%]	RMS_{90}
Durham	33.7 / -10.1	25.3 / 14.1	23.1 / 10.1
long. inv. $k_t(R = 1.5)$	6.7 / -6.3	8.3 / 6.6	6.7 / 6.2
VLC ($R = 1.5$)	-0.1 / -5.3	5.7 / 5.7	4.3 / 5.6

The bias and resolutions shown in Table 5.5 confirm that for a less robust algorithm like Durham, the trimming technique is required, particularly for the jet mass. On the opposite, the VLC and longitudinally invariant k_t algorithms are much less affected, particularly in the case of VLC the algorithm is sufficiently robust against the $\gamma\gamma \rightarrow$ hadrons background. The median yields a bias in the jet mass of 3% and the IQR_{34} a resolution of 4% for VLC algorithm, a 2% better than longitudinally invariant k_t.

5.5 Summary

In this work a new jet algorithm is proposed, which offers robust performance in the presence of the mild background levels expected at lepton colliders, while retaining the natural inter-particle distance criterion in the [energy, angle] basis (as opposed to the [transverse momentum, rapidity] basis of hadron collider algorithms). The algorithm is further generalised with a variable exponent that allows to tune the background rejection for the specific requirements of a given analysis.

The forward-peaked $\gamma\gamma \to$ hadrons background at future high-energy linear lepton colliders is one of the most important factors in the jet reconstruction performance. It has motivated ILC and CLIC to abandon classical, inclusive algorithms in favour of algorithms with a finite jet size. Algorithms that expose a reduced solid angle in the forward region of the detector, such as longitudinally invariant k_t or VLC are more robust. A particle-level study shows that these two algorithm have a different response, with VLC showing a slightly lower response, that is more stable versus polar angle. VLC is found to be less susceptible to background.

The jet reconstruction performance of several sequential reconstruction algorithms at high-energy lepton colliders has been studied. The study is based on detailed studies in full simulation of demanding benchmark channels, such as the ZZ, di-Higgs production and top quark pair production at a relatively harsh background level, high jet multiplicity and forward jets. In all cases the classical e^+e^- algorithms offers an inadequate performance. The same is true for the generalized version with beam jets. VLC provides significantly better mass resolution for the Higgs and top studies and considerably better jet reconstruction than the longitudinally invariant k_t algorithm.

Chapter 6

The Top Physics potential of Future Linear Colliders

The electro-weak symmetry breaking can be generated by the existence of a new strong sector, inspired by QCD, that may manifest itself at energies around 1 TeV. In many theories of the new strong sector, for example Randall-Sundrum models [109] or composite Higgs models [110], the strength of the coupling to this new sector of the Standard Model fields are expected to increase with their mass. For this and other reasons, the heavy top quark or t quark with a mass of approximately $m_t = 173$ GeV [3] is expected to be a window to new physics at the TeV energy scale.

A precise measurement of top quark interactions with the photon or Z-boson may reveal hints of new physics. In this chapter[1] the precision with which $\mathcal{CP}$-conserving and $\mathcal{CP}$-violating form factors of the $t\bar{t}Z$ and $t\bar{t}\gamma$ vertices can be determined is studied. A full simulation study of the reaction $e^+e^- \to t\bar{t}$ at $\sqrt{s} = 500$ GeV with 80% (longitudinally) polarized electron beams and 30% polarized positron beams for ILC is performed. The same study is repeated in the CLIC environment at $\sqrt{s} = 380$ GeV with 80% polarized electron beams to evaluate the top physics potential of both colliders.

6.1 Top quark production at e^+e^- colliders

The dominant source of top quarks through the exchange of neutral EW gauge bosons at an e^+e^- collider is top quark pair production ($e^+e^- \to \gamma, Z \to t\bar{t}$). A non-negligible source is single top production ($e^+e^- \to W^-t\bar{b}, W^+\bar{t}b$), already introduced in Section

[1] The top quark couplings studies at ILC with $\sqrt{s} = 500$ GeV, presented in this chapter, are published in my Master thesis [111], in a paper by the IFIC future colliders group [112] and the References [100, 33], which are the result of a collaboration between IFIC and LAL. This result is part of the ILCTDR and physics case. This work was presented at the international conference, ICHEP 2014 [113]. Results presented for CLIC at $\sqrt{s} = 380$ GeV have been included in the new "Staging baseline document of CLIC" [45]. A paper on the $\mathcal{CP}$-violating top quark couplings is in preparation.

1.3.3. The decay of the top quarks proceeds predominantly through $t \to W^{\pm}b$. The subsequent decays of the $W^{\pm}$ bosons to a charged lepton and a neutrino or a quark-anti-quark pair lead to a six-fermion final state. The study presented in the following focuses on the 'lepton+jets' final state $l^{\pm}\nu b\bar{b}q'\bar{q}$ representing about 43.4% on all $t\bar{t}$ pair decays. Single t quark production through the process $e^+e^- \to WW^* \to Wt\bar{b} \to l^{\pm}\nu b\bar{b}q'\bar{q}$ gives rise to the same six-fermion final state. Another relevant source is ZW^+W^- production. Experimentally, ZWW production can be distinguished rather efficiently from top quark pair production.

The cross sections at the Born level of the signal process $e^+e^- \to t\bar{t}$ and the main Standard Model background processes at a centre-of-mass energy of 500 GeV are summarised in Table 6.1.

Table 6.1: Unpolarized cross-sections and cross-sections at tree level for 100% beam polarization for signal and background processes.

Channel	$\sigma_{unpol.}$ [fb]	$\sigma_{-,+}$ [fb]	$\sigma_{+,-}$ [fb]
$t\bar{t}$	572	1564	724
$\mu^+\mu^-$	456	969	854
$\sum_{q=u,d,s,c} q\bar{q}$	2208	6032	2793
$b\bar{b}$	372	1212	276
γZ	11185	25500	19126
W^+W^-	6603	26000	150
ZZ	422	1106	582
ZW^+W^-	40	151	8.7
ZZZ	1.1	3.2	1.22
Single t for $e^+e^- \to e^-\bar{\nu_e}t\bar{b}$ [114]	3.1	10.0	1.7

As top quark pair production and single top quark production give rise to the same six-fermion final state, the question arises as to how one can distinguish both sources. At a fundamental level the single top and top quark pair production processes are entangled by interference between the different diagrams. No algorithm can ever separate them fully. However, one could hope to use some of the marked features of the $e^+e^- \to t\bar{t}$ process to make it stand out among the other processes that give rise to the $W^+bW^-\bar{b}$ final state. One could then hope to isolate samples that are enriched in top quark pairs or single top quark events. The invariant mass of the W^+b and $W^-\bar{b}$ combinations at parton level using $e^+e^- \to t\bar{t} \to W^+bW^-\bar{b}$ events generated with `WHIZARD` [77] at $\sqrt{s} = 500$ GeV is shown in Figure 6.1(a). The effect of initial state radiation and the beam energy spread expected at the ILC are included. The majority of events is found around $m_{W^+b} \sim m_{W^-b} \sim m_t$. However, in a significant fraction of events one of the Wb pairs has an invariant far from the top quark mass. The cross is populated by a mixture of $t\bar{t}$ events with an off-shell top quark and genuine single-top

production.

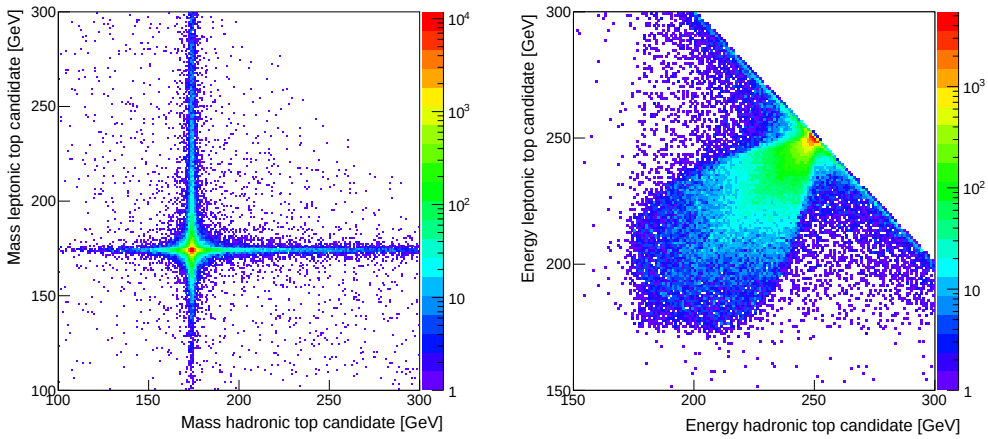

(a) (b)

Figure 6.1: (a) Reconstructed invariant mass at thruth level of the hadronic versus the leptonic side of $t\bar{t} \to W^+bW^-\bar{b}$ events. The events cluster around the input top mass value, but one can observe a significant amount of off-shell events. (b) Reconstructed beam energy at thruth level of the hadronic versus the leptonic side of $W^+bW^-\bar{b}$ events. The center-of-mass energy is 500 GeV, so double-top events cluster at beam energies of 250 GeV. In single-top events, the beam energy follows the diagonal $E_{lep} + E_{had} = 500$ GeV

The reconstructed beam energy of the Wb system decaying semi-leptonically versus the Wb system decaying hadronically is shown in Figure 6.1(b). The energy of the Wb pair tends to cluster at about half the center-of-mass energy, as expected for double-top events. Nevertheless, a significant fraction of events along the diagonal $E_{lep} + E_{had} = \sqrt{s}$ is observed. Those are mostly single top events.

These figures suggest an (ad-hoc) parton-level categorisation of events according to the number of on-shell top quark candidates, that is used to estimate the non-$t\bar{t}$ contribution to $e^+e^- \to W^+bW^-\bar{b}$ production. The following window for the top quark mass is considered:

$$|m_{Wb} - m_t^{MC}| < 15\ GeV \tag{6.1}$$

In on-shell top quark pair production the W^+b and W^-b system both satisfy this condition. Events that meet this criterion only for one of the Wb pairs are labeled as single top quark events, and the remaining events are considered as non-top events. With this criterion at $\sqrt{s} = 500$ GeV typically 90% of $e^+e^- \to W^+bW^-\bar{b}$ events is formed by top quark pairs, 9% corresponds to single top production and only 1% stems from processes that do not involve top quarks. These fractions depend strongly on the center-of-mass energy of the collider and on the beam polarization. Over a broad range of energies and operating scenarios the fraction of single-tops is far from negligible

and may have a significant impact on the measurement of top quark properties and the search for signs of new physics in $t\bar{t}$ production at lepton colliders. A realistic experimental strategy must therefore consider the $W^+bW^-\bar{b}$ inclusively and not only $e^+e^- \to t\bar{t}$ [112].

6.2 A general Lagrangian

New physics can modify the electro-weak $t\bar{t}X$ vertex described in the Standard Model by *V*ector and *A*xial vector couplings V and A to the vector bosons $X = \gamma, Z$. A lepton collider allows to probe these vertices directly. Contrarily to the situation at hadron colliders, the leading-order pair production process $e^+e^- \to t\bar{t}$ goes directly through the $t\bar{t}Z$ and $t\bar{t}\gamma$ vertices. There is no concurrent QCD production of t quark pairs, which increases greatly the potential for a clean measurement. A parametrisation of the $t\bar{t}X$ vertex valid to all orders of perturbation theory may be written as [2]:

$$\Gamma_\mu^{t\bar{t}X}(k^2, q, \bar{q}) = ie\left\{\gamma_\mu\left(F_{1V}^X(k^2) + \gamma_5 F_{1A}^X(k^2)\right) - \frac{\sigma_{\mu\nu}}{2m_t}(q+\bar{q})^\nu\left(iF_{2V}^X(k^2) + \gamma_5 F_{2A}^X(k^2)\right)\right\}, \quad (6.2)$$

with e being the electrical charge of the electron, $k^2 = (q+\bar{q})^2$ being the squared four-momentum of the exchanged boson and q and $\bar{q}$ being the four-vectors of the t and $\bar{t}$ quark, respectively. Furthermore, γ_μ are the Dirac matrices leading to vector currents of fermions and γ_5 is the Dirac matrix allowing to introduce an axial-vector current into the theory. Finally, $\sigma_{\mu\nu} = \frac{i}{2}(\gamma_\mu\gamma_\nu - \gamma_\nu\gamma_\mu)$ allows to describe the scattering of a particle with spin $1/2$ and a given magnetic moment.

Within the Standard Model the F_1 form factors have the following values at tree level:

$$F_{1V}^{\gamma,SM} = \frac{2}{3},\ F_{1A}^{\gamma,SM} = 0,\ F_{1V}^{Z,SM} = \frac{1}{4s_w c_w}\left(1 - \frac{8}{3}s_w^2\right),\ F_{1A}^{Z,SM} = -\frac{1}{4s_w c_w}, \quad (6.3)$$

while all the F_2 are zero. In Equation 6.3 s_w and c_w are the sine and the cosine of the Weinberg angle θ_W. The scale dependence of the form factors is a consequence of higher order corrections. The corrections of the vector currents lead to the anomalous electro-magnetic and weak-magnetic moments represented by F_{2V}^X that correct the gyromagnetic ratio g_t of the t quark. Typical values for these corrections are in the range $\mathcal{O}(10^{-3} - 10^{-2})$ [116]. Corrections to the axial-vector current result in the Form Factors F_{2A}^X that are related to the dipole moment $d_t^X = (e/2m_t)F_{2A}^X(0)$. These violate the combined $\mathcal{C}$harge and $\mathcal{P}$arity symmetry $\mathcal{CP}$. All couplings but $F_{2A}^X(k^2)$ conserve $\mathcal{CP}$. The Form Factors $F_{1V,A}^Z$ are related to couplings of t quarks with left and right-handed helicity to the Z:

$$g_L^Z = F_{1V}^Z - F_{1A}^Z, \qquad g_R^Z = F_{1V}^Z + F_{1A}^Z \quad (6.4)$$

Trivially, the same equations apply to the photon coupling g_L^γ.

[2] A dependence on an additional term $(q+\bar{q})_\mu \cdot F_3$ can be neglected in the limit of a vanishing electron mass [115].

$\mathcal{CP}$-violating effects in $e^+e^- \to t\bar{t}$ manifest themselves in top spin-momentum correlations [117, 118, 119]. In the literature there are quite a number of different proposals on how top quarks can be sensitive to $\mathcal{CP}$-violating interactions beyond the Kobayashi-Maskawa (KM) mechanism. Particularly for two SM extensions, (2Doublet Higgs Model (2DHM) and Minimal Supersymmetric Standard Model (MSSM)), it has been shown that they lead to electric and weak dipole form factors $d_t^{\gamma,Z}(s)$ of the top generated in the production vertex. $\mathcal{CP}$-violating effects in t (and $\bar{t}$) decay are ignored because their expected contribution are smaller.

6.3 Observables

Linear e^+e^- colliders allow for polarized electron and positron beams. With the use of polarized beams, t and $\bar{t}$ quarks oriented toward different angular regions in the detector are enriched in left-handed or right-handed t quark helicity [120]. This means that the experiments can independently access the couplings of left- and right-handed chiral parts of the t quark wave function to the Z boson and the photon. In case of polarized beams, Reference [121] suggests to express the form factors, introduced in previous Section 6.2, in terms of the helicity of the incoming electrons,

$$\begin{aligned} \mathcal{F}_{ij}^{L} &= -F_{ij}^{\gamma} + \Big(\frac{-\frac{1}{2} + s_w^2}{s_w c_w}\Big)\Big(\frac{s}{s - m_Z^2}\Big)F_{ij}^{Z} \\ \mathcal{F}_{ij}^{R} &= -F_{ij}^{\gamma} + \Big(\frac{s_w^2}{s_w c_w}\Big)\Big(\frac{s}{s - m_Z^2}\Big)F_{ij}^{Z} \end{aligned} \tag{6.5}$$

with $i = 1, 2$ and $j = V, A$ and m_Z being the mass of the Z boson.

6.3.1 Cross section and forward-backward asymmetry A_{FB}^t

The measurement of the cross section and forward-backward asymmetry A_{FB}^t for two different polarization settings allows to extract the photon and Z couplings of the t quark for each helicity state. Both observables are suited to monitor carefully experimental systematics that may occur in the extraction of form factors and couplings. The tree level cross section for $t\bar{t}$ quark pair production for an electron beam polarization $I = L, R$ reads:

$$\sigma_I = 2\mathcal{A}N_c\beta\left[(1 + 0.5\gamma^{-2})(\mathcal{F}_{1V}^I)^2 + (\mathcal{F}_{1A}^{I'})^2 + 3\mathcal{F}_{1V}^I\mathcal{F}_{2V}^I + (1 + 0.5\gamma^2)(\mathcal{F}_{2V}^I)^2\right], \tag{6.6}$$

where $\mathcal{A} = \frac{4\pi\alpha^2}{3s}$ with the running electromagnetic coupling $\alpha(s)$ and N_c is the number of quark colours. The factors γ and β are the Lorentz factor and the velocity of the t quark, respectively. The term $\mathcal{F}_{1A}^{I'} = \beta\mathcal{F}_{1A}^I$ predicts a reduced sensitivity to axial vector couplings near the $t\bar{t}$ production threshold.

The forward-backward asymmetry A_{FB}^t can be expressed as

$$(A_{FB}^t)_I = \mp\,\mathcal{A}N_c\beta \cdot \frac{3\mathcal{F}_{1A}^{I'}(\mathcal{F}_{1V}^I + \mathcal{F}_{2V}^I)}{\sigma_I}. \tag{6.7}$$

The '-' sign applies in case of an initial left-handed polarized electron beam, i.e. $I = L$, and the '+' applies correspondingly in case of an initial right-handed polarized electron beam, i.e. $I = R$. In the Standard Model the forward-backward asymmetry takes the values $(A^t_{FB})_L = 0.37(0.21)$ and $(A^t_{FB})_R = 0.45(0.26)$ at tree level assuming a center-of-mass energy of 500(380) GeV. Experimentally the forward-backward asymmetry A^t_{FB} has the well known definition:

$$A^t_{FB} = \frac{N(\cos\theta_{top} > 0) - N(\cos\theta_{top} < 0)}{N(\cos\theta_{top} > 0) + N(\cos\theta_{top} < 0)}, \tag{6.8}$$

where N is the number of events in the two detector hemispheres whit respect to the polar angle θ_{top} of the top quark.

With the introduced observables the six $\mathcal{CP}$-conserving form factors defined for the Z and the photon can in principle be extracted simultaneously. However, close to the $t\bar{t}$ threshold the observables depend always on the sum $F_{1V} + F_{2V}$. Therefore, a full disentangling of the form factors will be imprecise for energies below about 1 TeV. Hence, in the present study either the precision on the Form Factors $F^X_{1V,A}$, or equivalently on the Couplings $g^X_{L,R}$, are determined simultaneously, while the two F_{2V} are kept at their Standard Model values or vice versa. Due to these considerations the study will only make use of the cross section and A^t_{FB} since these are either the most precise observable in case of the cross section or the one that is most sensitive to axial couplings in case of A^t_{FB}. Other observables, such as the top quark polarization used in [100], can provide information of the fraction of right-handed t quarks to a precision of about 2%. This redundancy forms a powerful handle on the experimental systematic uncertainties of the measurement.

6.3.2 Optimal $\mathcal{CP}$-violating observables

The term $F^{\gamma,Z}_{2A}$ in Equation 6.2 represents the axial form factors that violate $\mathcal{CP}$. They are related to the electric and weak dipole form factors $d^\gamma_t(s)$ and $d^Z_t(s)$ which may be represented by the effective interaction (Equation 94 from [122]):

$$\mathcal{L} = -\frac{i}{2} d^\gamma_t \bar{t}\sigma_{\mu\nu}\gamma_5 t F^{\mu\nu} - \frac{i}{2} d^Z_t \bar{t}\sigma_{\mu\nu}\gamma_5 t Z^{\mu\nu} \tag{6.9}$$

These form factors $d^{\gamma,Z}_t(s)$ can have imaginary (i.e., absorptive) parts. The real parts $\mathrm{Re}[d^{\gamma,Z}_t(s)]$ induce a difference in the t and $\bar{t}$ polarizations orthogonal to the scattering plane of reaction. Non-zero absorptive parts, $\mathrm{Im}[d^{\gamma,Z}_t(s)]$, lead to a difference in the t and $\bar{t}$ polarizations along the top direction of flight. Therefore, in the following we consider the production of a top quark pair via the collision of an unpolarized positron beam and a polarized electron beam:

$$e^+(\mathbf{e}_+) + e^-(\mathbf{e}_-, p) \quad \rightarrow \quad t(\mathbf{k}_t) + \bar{t}(\mathbf{k}_{\bar{t}}), \tag{6.10}$$

where p is the polarization of the electron beam (p = -1 refers to left-handed electrons as before). For this purpose the most interesting final states are those from

semi-leptonic t decay and hadronic $\bar{t}$ decay and vice versa:

$$t\ \bar{t} \quad \rightarrow \quad \ell^+(\mathbf{q}_+) + \nu_\ell + b + \overline{X}_{\mathrm{had}}(\mathbf{q}_{\bar{X}}), \tag{6.11}$$

$$t\ \bar{t} \quad \rightarrow \quad X_{\mathrm{had}}(\mathbf{q}_X) + \ell^-(\mathbf{q}_-) + \bar{\nu}_\ell + \bar{b}\ , \tag{6.12}$$

where the 3-momenta in Equations 6.10 - 6.12 refers to the e^+e^- center-of-mass frame.

The observables must be chosen to be functions of the available four momenta at $t\bar{t}$ events, as the directions of the hadronic system from top decay, the charged lepton momentum, of the e^+ beam direction and the center-of-mass $\sqrt{s}$, taking the following form:

$$\mathcal{O}_+^{Re} = (\hat{q}_+^* \times \hat{q}_{\bar{X}}) \cdot \hat{e}_+ \tag{6.13}$$

$$\mathcal{O}_+^{Im} = -[1 + (\frac{\sqrt{s}}{2m_t} - 1)(\hat{q}_{\bar{X}} \cdot \hat{e}_+)^2]\hat{q}_+^* \cdot \hat{q}_{\bar{X}} + \frac{\sqrt{s}}{2m_t}\hat{q}_{\bar{X}} \cdot \hat{e}_+ \hat{q}_+^* \cdot \hat{e}_+ \tag{6.14}$$

where m_t is the top mass. $\mathcal{O}_-$ observables are defined to be the $\mathcal{CP}$ image of $\mathcal{O}_+$ and are obtained by the substitutions $\hat{q}_{\bar{X}} \rightarrow -\hat{q}_X$, $\hat{q}_+^* \rightarrow -\hat{q}_-^*$, $\hat{e}_+ \rightarrow \hat{e}_+$ from $\mathcal{O}_+$.

The way to extract $F_{2A}^{\gamma,Z}$ form factors is to construct asymmetries. An example is the asymmetry of the lepton with respect to the production plane [118] which is the difference of the expectation values:

$$\mathcal{A} = \langle \mathcal{O}_+(s, \hat{q}_+^*, \hat{q}_{\bar{X}}, \hat{e}_+) \rangle - \langle \mathcal{O}_-(s, \hat{q}_-^*, \hat{q}_X, \hat{e}_+) \rangle \tag{6.15}$$

The resulting asymmetries $\mathcal{A}^{Re}, \mathcal{A}^{Im}$ are sensitive to $\mathcal{CP}$-violation effects in the $t\bar{t}$ production amplitude through the contributions of $Re[F_{2A}^{\gamma,Z}]$ and $Im[F_{2A}^{\gamma,Z}]$ respectively. Equations 6.16 and 6.17 are a reasonable approximation to write these relations [123].

$$\mathcal{A}_{\gamma,Z}^{Re} = \langle \mathcal{O}_+^{Re} \rangle - \langle \mathcal{O}_-^{Re} \rangle = c_\gamma [pRe(F_{2A}^\gamma) + KZRe(F_{2A}^Z)] \tag{6.16}$$

$$\mathcal{A}_{\gamma,Z}^{Im} = \langle \mathcal{O}_+^{Im} \rangle - \langle \mathcal{O}_-^{Im} \rangle = d_\gamma [Im(F_{2A}^\gamma) + pKZIm(F_{2A}^Z)] \tag{6.17}$$

The coefficients d_γ and c_γ depend on the specific decay channel and the energy of the process[3]. Measuring these asymmetries for both incoming beam polarizations one can double the number of observables from two to four and can very easily isolate each $F_{2A}^{\gamma,Z}$ term by solving a trivial system of linear equations.

[3]For $t\bar{t}$ semi-leptonic decays and a center-of-mass energy of 500 GeV, the coefficients take the values: $c_\gamma = 0.35$, $KZ = -0.6$ and considering $d_\gamma \sim c_\gamma = 0.35$ [123].

6.4 Monte Carlo simulation study

This study is carried out on a full simulation of the ILD detector for ILC [100, 33] and on the CLIC_ILD detector for CLIC. Signal and background events are generated with version 1.95 of `WHIZARD` interfaced to `PYTHIA` for the parton shower. Technical details about the event generation and the full simulation of the detector are discussed in Chapter 4.

The main parameters of the Monte Carlo samples used for this analysis are summarized in Table 6.2. A luminosity of $250\,\text{fb}^{-1}$ for each polarization is considered for both environments ILC at $\sqrt{s} = 500$ GeV and CLIC at $\sqrt{s} = 380$ GeV. Beams are fully polarized for ILC $(P(e^-), P(e^+) = \mp 1, \pm 1)$ and only the e^- beam is polarized for CLIC $(P(e^-), P(e^+) = \mp 0.8, 0)$. For all generated events, the luminosity spectrum of the 500 GeV ILC and 380 GeV CLIC machines is considered respectively. At both colliders about 60% of the particles are expected to have 99% or more of the nominal energy [124, 45]. The multi-peripheral $\gamma\gamma \to$ hadrons background expected for each collider is overlaid on the signal.

Table 6.2: Main parameters and information of the Monte Carlo samples generated for the analysis at ILC (second column) and CLIC (third column).

Collider	**ILC**	**CLIC**
Sample	$e^+e^- \to l^\pm\nu b\bar{b}q'\bar{q}$	$e^+e^- \to 6f (t\bar{t}$ compatible)
$\sqrt{s}$ [GeV]	500	380
Luminosity [fb^{-1}]	500	500
$P(e^-), P(e^+)$	$\mp 1, \pm 1$	$\mp 0.8, 0$
Detector model	ILD_o1_v05 [54]	CLIC_ILD_CDR [53]
Number of BX	1	300
Background	1.7 $\gamma\gamma \to$ hadrons / BX	0.0464 $\gamma\gamma \to$ hadrons / BX

Samples generated for ILC correspond to the semi-leptonic final state $l^\pm\nu b\bar{b}q'\bar{q}$ of the $t\bar{t}$ pair decay. On the other hand, samples for CLIC are a six-fermion final state which includes also the fully-hadronic and fully-leptonic $t\bar{t}$ pair decays, thus a selection of the "lepton+jets" $t\bar{t}$ final state is required. The $\gamma\gamma \to$ hadrons background overlaid at 380 GeV CLIC samples is less than encountered at multi-TeV stages discussed in Section 4.2.4, and less restrictive timing cuts are required. Particle flow objects are selected using a set of timing cuts, corresponding to the "loose" selection of Reference [85].

6.4.1 Event selection

The entire selection procedure including lepton and b-jet identification, top quark reconstruction and suppression of multi-peripheral $\gamma\gamma \to$ hadrons background for ILC samples is explained in detail in References [111, 125, 126].

The basic selection requires an isolated charged lepton (e or μ) and two b-tagged jets. In general leptons are identified using typical selection criteria. The lepton from the W boson decay is either the most energetic particle in a jet or has a sizable transverse momentum with respect to neighbouring jets. More specifically, the following criteria are applied:

$$x_T = p_{T,lepton}/M_{jet} > 0.25 \quad \text{and} \quad z = E_{lepton}/E_{jet} > 0.6, \tag{6.18}$$

where E_{lepton} is the energy and $p_{T,lepton}$ the transverse momentum of the lepton within a jet with energy E_{jet} and mass M_{jet}. The decay lepton in case of e and μ can be identified with an efficiency of about 85%, where the selection has a tendency to reject low momentum leptons. Part of the τ leptons decay to e or μ, which are collinear with the produced τ but have lower momentum than primary decay leptons. Taking into account the τ leptons, the efficiency to identify the decay lepton is about 70%.

The identified lepton is removed from the list of reconstructed particles and the remaining final state is again clustered into four jets. Two of these must be identified as being produced by the b-quarks of the t quark decay. The b-likeness or *b-tag* is determined with the `LCFIPlus` package, which uses information of the tracking system as input. Secondary vertices in the event are analysed by means of the jet mass, the decay length and the particle multiplicity. As shown in Figure C.2 in Appendix C.1, the higher b-tag value is typically 0.92 while the smaller one is still around 0.65. Both values are clearly distinct from those obtained for jets from light quarks. Their b-tag value is around 0.14. The b-tagging requirement suppresses about 97% of the dominant W^+W^- background.

Additional selection criteria comprise cuts on the top quark and $W^\pm$ boson masses and of the invariant mass of the total hadronic final state. These include cuts on jet thrust $T < 0.9$ and on the invariant mass of the hadronic final state $180 < m_{had.} < 420$ GeV. In addition the mass windows for the reconstructed W-boson and t-quark are chosen to $50 < m_W < 250\,\text{GeV}$ and $120 < m_t < 270\,\text{GeV}$. Background processes can be very efficiently removed down to a negligible level.

The total selection efficiency for ILC is about 56% for both beam polarizations, including events with a τ lepton in the final state. In the CLIC analysis at 380 GeV, the same selection criteria have been used. The selection efficiency for semi-leptonic events for CLIC samples results 59% for left-handed polarized e^- and 54% for right-handed e^-.

6.4.2 Event reconstruction

Particles from $\gamma\gamma \to$ hadrons background, that is produced in the same BX as the signal, can reach the outer layers of the detector and affect the overall detector performance, in particular jet reconstruction. Classical e^+e^- algorithms such as Durham are quite strongly affected. Better results are obtained with the longitudinally invariant k_t algorithm [95, 96]. However, the VLC algorithm, with a Durham-like distance criterion, is found to offer even better jet reconstruction performance than longitudinally invariant k_t, as shown in Section 5.4.1.

One top quark candidate is reconstructed from the hadronically decaying W which is combined with one of the b-quark jets. The two remaining jets are associated with the decay products of the W boson. The charged lepton allows for the determination of the top quark charge. As there are two b-tagged jets and two W-boson candidates there is a two-fold ambiguity in the reconstruction. The $t\bar{t}$ system is reconstructed by choosing the combination of b quark jet and W boson that minimises the following equation:

$$d^2 = \left(\frac{m_{cand.} - m_t}{\sigma_{m_t}}\right)^2 + \left(\frac{E_{cand.} - E_{beam}}{\sigma_{E_{cand.}}}\right)^2 + \left(\frac{p_b^* - 68}{\sigma_{p_b^*}}\right)^2 + \left(\frac{cos\theta_{bW} - 0.23}{\sigma_{cos\theta_{bW}}}\right)^2 \quad (6.19)$$

In this equation $m_{cand.}$ and $E_{cand.}$ are invariant mass and energy of the top quark candidate decaying hadronically, respectively, and m_t and E_{beam} are input top quark mass and the beam energy of 250 GeV. Beyond that, it introduces the momentum of the b quark jet in the centre-of-mass frame of the top quark, p_b^* and the angle between the b quark and the W boson. The measured values are compared with the expected ones and the denominator is the width of the measured distributions.

The direction measurement depends very strongly on the correct association of the b quarks to the jets of the hadronic W boson decays. The ILC analysis is carried out separately for a left-handed polarized electron beam and for a right-handed polarized beam. In case of a right-handed electron beam the direction of the top quark can be precisely reconstructed. In case of a left-handed electron beam the final state features two hard jets from the b quarks and soft jets from the hadronically decaying W boson. This configuration leads to migrations in the polar angle distribution of the t quark as visible in Figure 6.2(a).

The migration motivates to restrict the determination of A_{FB}^t in case of left-handed initial electron beams to cleanly reconstructed events. For this, a second χ^2 is defined that compares the measured values of the Lorentz factor γ of the top, the momentum of the b quark in the rest frame of the top and the angle $\cos\theta_{bW}$ between the b quark and the W boson. The correct association of the of jets from b quarks to that from W bosons is checked with the MC truth information. Events in which this association went wrong, labelled as *bad combination* in Figure C.3 from Appendix C.1, lead to a distorted distribution in these observables.

The quality of the reconstructed events is estimated by the following quantity:

$$\chi^2 = \left(\frac{\gamma_t - 1.435}{\sigma_{\gamma_t}}\right)^2 + \left(\frac{E_b^* - 68}{\sigma_{E_b^*}}\right)^2 + \left(\frac{cos\theta_{bW} - 0.23}{\sigma_{cos\theta_{bW}}}\right)^2 \quad (6.20)$$

The reconstructed polar angle distribution of the top quark is compared with the generated one for different cuts on χ^2. For a value of $\chi^2 < 15$ an excellent agreement between the generated and reconstructed polar angle distributions is obtained, see Figure 6.2(b). The tight selection however reduces the efficiency in case of $P(e^-), P(e^+) = -1, +1$ from 55% to 28%.

The migration on the top quark polar angle distributions is also observed for CLIC samples. However this effect appears for both beam polarizations as shown in Figure

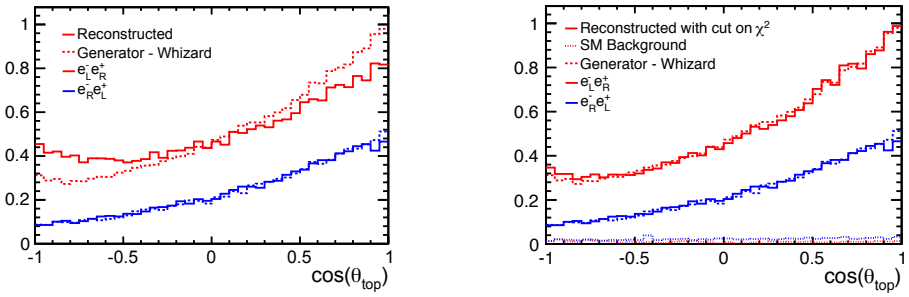

(a) (b)

Figure 6.2: (a) Reconstructed forward-backward asymmetry compared with the prediction by the event generator WHIZARD [77] for two configurations of the beam polarizations at ILC 500 GeV. (b) The same but after the application of a cut on $\chi^2 < 15$ for the beam polarizations $P(e^-), P(e^+) = -1, +1$ as explained in the text. Note, that in both figures no correction is applied for the beam polarizations $P(e^-), P(e^+) = +1, -1$. The figure on the right hand side shows also the residual Standard Model background.

6.3(a). A^t_{FB} values from generated events differ notably from those from reconstructed events. In order to cure these migrations the previous χ^2 strategy is carried out [with the E_{beam} = 190 GeV and $< \cos\theta_{bW} >$ = -0.67]. Polar angle distributions after the cut on χ^2 are shown in Figure 6.3(b). A tighter cut is needed this time, $\chi^2 < 1$ for both polarizations, giving rise to a selection efficiency around 17%.

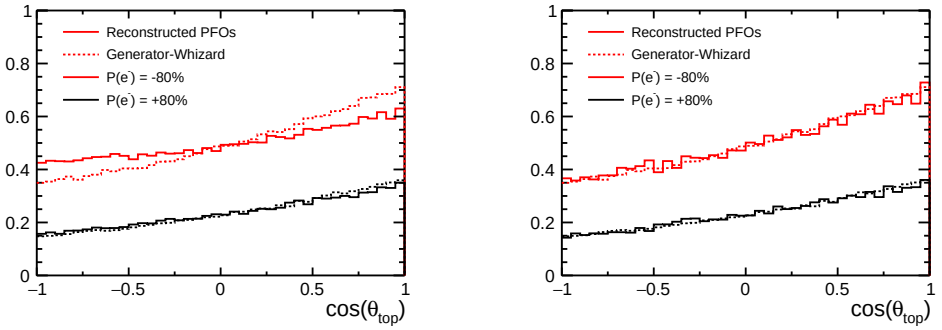

(a) (b)

Figure 6.3: (a) Reconstructed forward-backward asymmetry compared with the prediction by the event generator for two configurations of the beam polarizations at CLIC 380 GeV. (b) The same but after the application of a cut on $\chi^2 < 1$ for both beam polarizations $P(e^-), P(e^+) = \pm 0.8, 0$.

6.4.3 Statistical uncertainties

The determined efficiencies after the event selection and reconstruction, presented in previous sections, are used to estimate the statistical uncertainties on the observables. The samples used in the ILC study have 100% polarized beams. The cross section scales with the polarization in a well defined way according to [127]

$$\sigma_{P(e^-),P(e^+)}=\frac{1}{4}\left[(1-P(e^-)P(e^+))(\sigma_{-,+}+\sigma_{+,-})+(P(e^-)-P(e^+))(\sigma_{+,-}-\sigma_{-,+})\right] \quad (6.21)$$

where $\sigma_{-,+}$ and $\sigma_{+,-}$ takes the values, shown in Table 6.1, of $t\bar{t}$ pair production cross sections for ILC at 500 GeV. The cross sections for CLIC at 380 GeV are calculated with Equation 6.6. The realistic beam polarizations $[P(e^-), P(e^+) = \pm 0.8, \mp 0.3$ for ILC and $P(e^-),\ P(e^+)\ = \pm 0.8,\ 0$ for CLIC] are taken into account by combining MC samples according to Equation 6.21. With the determined efficiencies a statistical uncertainty of the cross section $e^+e^- \to t\bar{t}$ of 0.47% in case $P(e^-), P(e^+) = -0.8, +0.3$ and 0.63% in case $P(e^-), P(e^+) = +0.8, -0.3$ can be derived for ILC samples. At CLIC the statistical uncertainties take similar values, 0.45% and 0.66% for $P(e^-) = -0.8$ and $P(e^-) = +0.8$ respectively, assuming an integrated luminosity of 500 fb^{-1}.

Table 6.3: Statistical precisions expected for the cross sections and A^t_{FB} for both beam polarizations at ILC $\sqrt{s} = 500$ GeV and CLIC $\sqrt{s} = 380$ GeV

ILC $\sqrt{s} = 500$ GeV, 500fb^{-1} [%]		
$P(e^-), P(e^+)$	$(\delta\sigma/\sigma)_{stat.}$	$(\delta A^t_{FB}/A^t_{FB})_{stat.}$
$-0.8, +0.3$	0.47	1.8
$+0.8, -0.3$	0.63	1.3
CLIC $\sqrt{s} = 380$ GeV, 500fb^{-1} [%]		
$P(e^-), P(e^+)$	$(\delta\sigma/\sigma)_{stat.}$	$(\delta A^t_{FB}/A^t_{FB})_{stat.}$
$-0.8, 0$	0.45	3.8
$+0.8, 0$	0.66	4.5

The forward backward asymmetry can be determined at ILC to a statistical precision of better than 2%. The lower efficiency at CLIC has an impact in the statistical uncertainty of A^t_{FB} which is of the order of 4%. The precise results corrected to the beam polarizations $P(e^-), P(e^+) = \pm 0.8, \mp 0.3$ at ILC at $\sqrt{s} = 500$ GeV, together with those for CLIC at $\sqrt{s} = 380$ GeV and $P(e^-), P(e^+) = \pm 0.8, 0$, are given in Table 6.3.

6.4.4 $\mathcal{CP}$-violating asymmetries

The observables with sensitivity to $\mathcal{CP}$-violation of Equations 6.16 and 6.17 are reconstructed on simulated events. The generated events are restricted to the tree-level physics of the SM, hence $F^{\gamma,Z}_{2A}$ couplings and asymmetries are expected to be zero.

The impact of non-zero $F_{2A}^{\gamma,Z}$ couplings is investigated in Appendix C.3. As shown in Figure 6.4, the reconstructed $\mathcal{O}_{\pm}^{Re}$ distributions are mainly centred at zero, however $\mathcal{O}_{\pm}^{Im}$ distributions exhibit an asymmetry due to the polarization p. As both $\mathcal{O}_{+}^{Im}$ and $\mathcal{O}_{-}^{Im}$ are affected equally, the effect vanishes when $\mathcal{A}_{\gamma,Z}^{Im}$ is calculated. In the same way, differences observed between reconstructed and generated quantities tend to disappear when asymmetries are calculated.

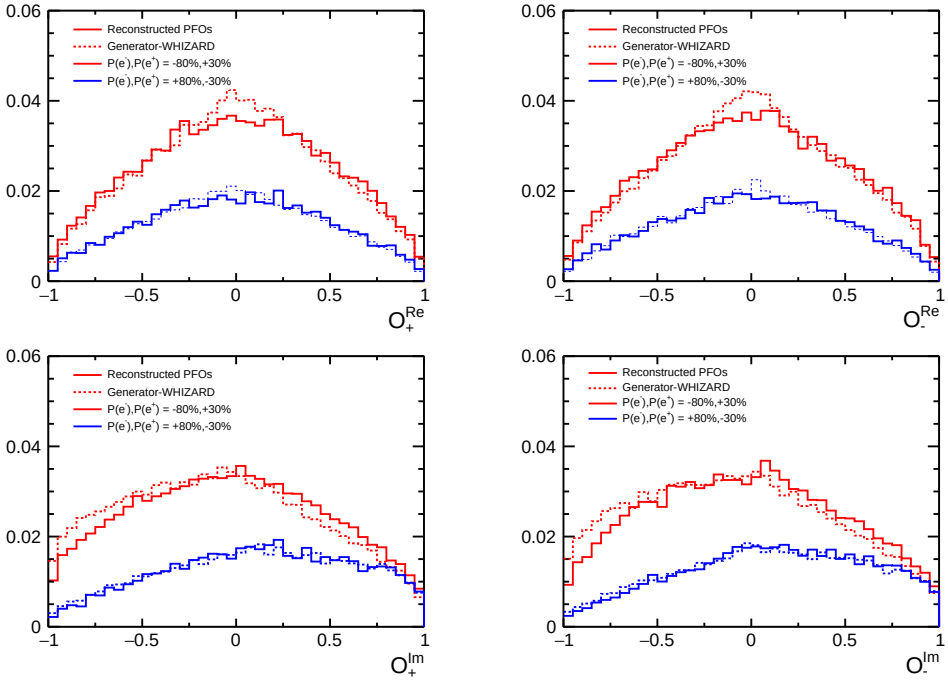

Figure 6.4: Distributions of the optimal observables, $\mathcal{O}_{\pm}^{Re,Im}$, for ILC at $\sqrt{s} = 500$ GeV. Distributions in red colour correspond to the beam polarizations $P(e^-), P(e^+) = -0.8, +0.3$ and the black ones to $P(e^-), P(e^+) = +0.8, -0.3$.

The mean value and the statistical uncertainty of these observables are given in Table 6.4 for ILC at 500 GeV and left-handed polarized e^- beams[4]. The statistical uncertainty is determined as $\delta_{stat} = RMS/\sqrt{N}$ with the number of events $N = \mathcal{L} \times \sigma_{tt} \times \varepsilon_{sel} \times BR_{SL}$ where $\mathcal{L}$: Luminosity, $\sigma_{\mathbf{tt}}$: total $t\bar{t}$ cross-section, ε_{sel}: efficiency of selection after quality cuts and BR_{SL}: Branching ratio of the $t\bar{t}$ semi-leptonic decay (43,4%). The luminosity considered is 500 fb^{-1} and the total $t\bar{t}$ cross-section, using Equation 6.21, gives 419 fb for the semi-leptonic decay channel with $P(e^-), P(e^+) = -0.8, +0.3$. As migration effects do not occur, no extra cuts are needed and the selection efficiency is values around 55% in all cases. As expected, the mean $\langle \mathcal{O}_{\pm}^{Im} \rangle$ are found to be incompatible with zero. In the case of CLIC events at 380 GeV the

[4]In Appendix C.2 the results for right-handed polarized e^- beams at ILC are shown in Table C.1. CLIC results for both polarizations are listed in Tables C.2 and C.3.

Table 6.4: Mean values and statistical uncertainties of the optimal observables, $\mathcal{O}_{\pm}^{Re,Im}$, for ILC 500 GeV and $P(e^-), P(e^+) = -0.8, +0.3$.

ILC $\sqrt{s}$ = 500 GeV, 500fb^{-1}, $P(e^-), P(e^+) = -0.8, +0.3$				
$\mathcal{CP}$ **obs.**	**Generated**	$\delta_{\mathbf{stat}}$	**Reconstructed**	$\delta_{\mathbf{stat}}$
$\langle \mathcal{O}_{+}^{Re} \rangle_L$	0.0032	0.002	0.0045	0.002
$\langle \mathcal{O}_{-}^{Re} \rangle_L$	-0.0021	0.002	-0.0022	0.002
$\langle \mathcal{O}_{+}^{Im} \rangle_L$	-0.0837	0.002	-0.031	0.002
$\langle \mathcal{O}_{-}^{Im} \rangle_L$	-0.0815	0.002	-0.029	0.002

optimal observables are less affected by polarization. All distributions are centred at zero and differences between reconstructed and generated events are not so remarkable, as shown in Figure 6.5.

The asymmetries for generated events and reconstructed events shown in Table 6.5 are compatible with zero, as expected. Small deviations are due to statistical

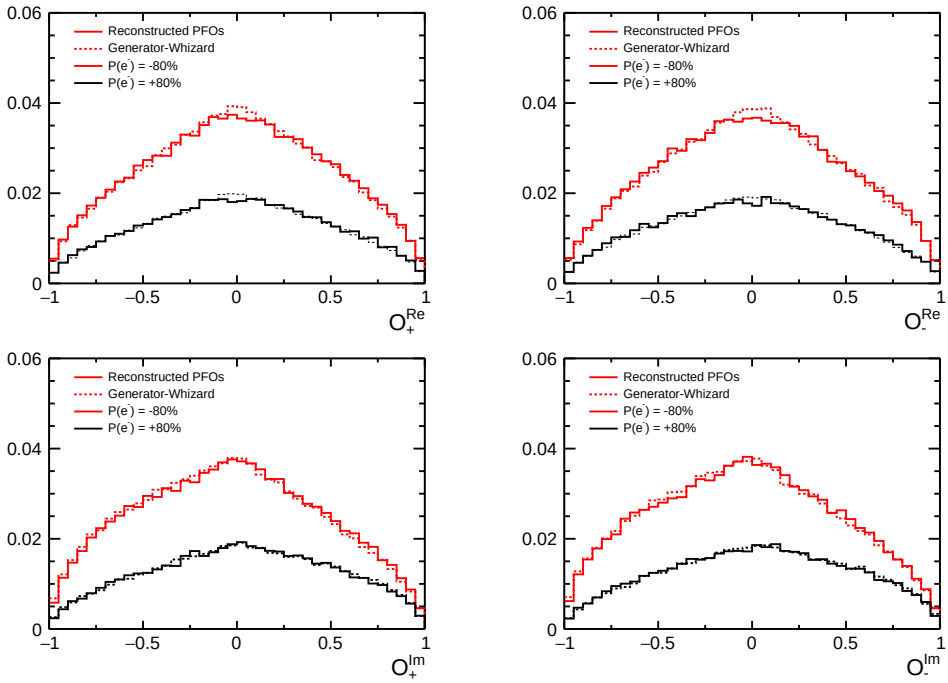

Figure 6.5: Distributions of the optimal observables, $\mathcal{O}_{\pm}^{Re,Im}$, for CLIC at $\sqrt{s} = 380$ GeV. Distributions in red colour correspond to the beam polarizations $P(e^-), P(e^+) = -0.8, 0$ and the black ones to $P(e^-), P(e^+) = +0.8, 0$.

fluctuations as pointed out in the Appendix B of [128].

Table 6.5: Reconstructed $\mathcal{CP}$-violating asymmetries and statistical uncertainties for ILC at $\sqrt{s} = 500$ GeV and CLIC at $\sqrt{s} = 380$ GeV.

ILC $\sqrt{s} =$ 500 GeV, 500fb^{-1} [%]		
$P(e^-), P(e^+)$	$\mathcal{A}^{Re}_{\gamma,Z}$	$\mathcal{A}^{Im}_{\gamma,Z}$
-0.8, +0.3	0.0053 ± 0.003	-0.0022 ± 0.003
+0.8, -0.3	0.0025 ± 0.004	-0.007 ± 0.004
CLIC $\sqrt{s} =$ 380 GeV, 500fb^{-1} [%]		
$P(e^-), P(e^+)$	$\mathcal{A}^{Re}_{\gamma,Z}$	$\mathcal{A}^{Im}_{\gamma,Z}$
-0.8, 0	-0.00006 ± 0.003	0.0004 ± 0.003
+0.8, 0	0.007 ± 0.004	-0.0019 ± 0.004

6.5 Theory and systematic uncertainties

The extraction of the form factors requires precise predictions of several quantities, such as the top pair production rate or the forward-backward asymmetry. Theoretical uncertainties can significantly contribute to the precision of the the form factors extraction. QCD and electro-weak corrections are reviewed in Reference [33]. Uncertainties from QCD corrections are under relatively good control at N^3LO level. However the one-loop electro-weak corrections are still large and NNLO calculations are needed to perform this measurement.

Additionally, there are several machine parameters that can be a source of systematic uncertainties, for instance the luminosity, the polarization or the beamstrahlung must be controlled under half per cent level. The beam energy, luminosity and polarization can be controlled to well beyond the required level. The luminosity spectrum can be determined in situ to good precision using Bhabha events [129]. Reference [33] summarizes the impact of these parameters as follows [...it can be concluded that the total systematic uncertainties will not exceed the statistical uncertainties]. This analysis furthermore requires an excellent control over experimental uncertainties such as that on b-tagging, efficiency and the uncertainty due to $t\bar{t}$ modelling. While several handles to control such uncertainties are available, a quantitative analysis has not yet been performed.

6.6 Limits on form factors

$\mathcal{CP}$-conserving form factors

The measured cross sections and A_{FB}^t lead, for two polarization configurations, to a set of four observables. By means of Equations 6.6 and 6.7 the uncertainties on these observables are used to build up a system of linear equations to determine the variances of up to four variables[5]. The variances are equivalent to the square of the standard deviations of the variables under study. The strategy chosen in this study is to determine the following quantities separately:

1. Form Factors F_{1V}^{γ}, F_{1V}^{Z}, F_{1A}^{Z}, assuming no variation of the Form Factors F_{2j}^{X};
2. Form Factors F_{2V}^{γ}, F_{2V}^{Z} assuming no variation of the Form Factors F_{1j}^{X} ;
3. Couplings $g_L^{\gamma}, g_R^{\gamma}, g_L^{Z}, g_R^{Z}$.

Note, that the Form Factor F_{1A}^{γ} is fixed to be 0 in order to respect QED gauge invariance. On the other hand all four Couplings g_I^X are allowed to vary freely. The complete covariance matrices, for ILC at 500 GeV and CLIC at 380 GeV, are given in Appendix C.4. The resulting standard deviations are listed in Table 6.6. At ILC, a %-level precision is reached for all form factors. CLIC is similar to ILC, except for F_{1A}^{Z}, due to the smaller value of β.

Table 6.6: Standard deviations and resulting relative precisions of form factors and couplings derived from the statistical precisions on the observables cross section and A_{FB}^t as listed in Table 6.3.

ILC $\sqrt{s}$ = 500 GeV, 500fb^{-1}									
	$\mathbf{F_{1V}^{\gamma}}$	$\mathbf{F_{1V}^{Z}}$	$\mathbf{F_{1A}^{Z}}$	$\mathbf{F_{2V}^{\gamma}}$	$\mathbf{F_{2V}^{Z}}$	$\mathbf{g_L^{\gamma}}$	$\mathbf{g_R^{\gamma}}$	$\mathbf{g_L^{Z}}$	$\mathbf{g_R^{Z}}$
SM Value	2/3	0.230	-0.595	0	0	2/3	2/3	0.824	-0.364
σ	0.002	0.003	0.007	0.001	0.002	0.005	0.005	0.008	0.009
σ_{rel} [%]	0.3	0.9	1.2	-	-	0.8	0.8	1.0	2.5
CLIC $\sqrt{s}$ = 380 GeV, 500fb^{-1}									
	$\mathbf{F_{1V}^{\gamma}}$	$\mathbf{F_{1V}^{Z}}$	$\mathbf{F_{1A}^{Z}}$	$\mathbf{F_{2V}^{\gamma}}$	$\mathbf{F_{2V}^{Z}}$	$\mathbf{g_L^{\gamma}}$	$\mathbf{g_R^{\gamma}}$	$\mathbf{g_L^{Z}}$	$\mathbf{g_R^{Z}}$
σ	0.002	0.003	0.019	0.002	0.004	0.015	0.014	0.02	0.019
σ_{rel} [%]	0.3	0.9	3.2	-	-	2.2	2.2	2.4	5.2

Electro-weak couplings can be measured at the LHC in associated $\bar{t}t\gamma$ and $\bar{t}tZ$ production. A comprehensive compilation of the statistical precisions on the form factors that can be expected at the end of the HL-LHC is given in [131]. Reference [19]

[5]For the Linear Algebra the software package `Eigen` [130] version 3.2.2 has been used.

presents an update on $\bar{t}tZ$ form factors. The expectations from [131] are compared with the results presented in this study in Figure 6.6.

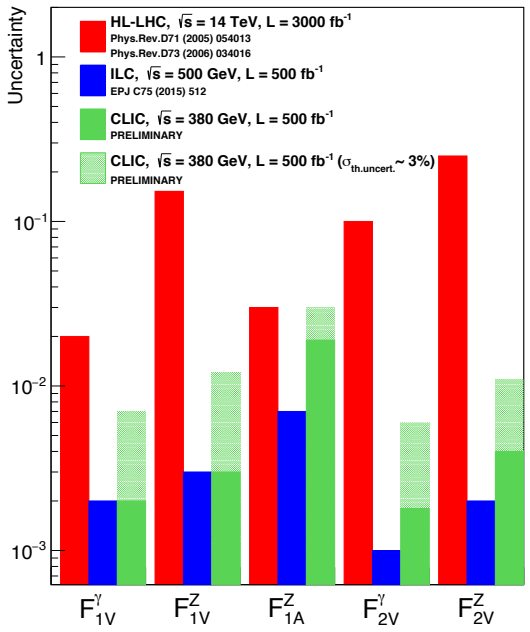

Figure 6.6: Uncertainties of the top quark form factors compared between estimations for HL-LHC [131, 19], ILC at 500 GeV and L= 500 fb^{-1} [100] and CLIC at 380 GeV and L= 500 fb^{-1} [45]. The form factors are extracted from the measured forward backward asymmetry and cross-section. For the ILC, $\mp$80% e− polarization and $\mp$30% e+ polarization are considered and $\mp$80% e^- polarization for CLIC.

All but one form factor will be measured at least 10 times better at the ILC and CLIC for the scenarios discussed in this study than at the LHC. The exception is F_{1A}^Z where [19] quotes a possible statistical precision of $\delta F_{1A}^Z \approx 0.031$. Note that the interference between the γ and the Z in case of $e^+e^- \to t\bar{t}$ will allow for measuring flips of the signs of the form factors that will be unnoticed in associated $\bar{t}tZ$ production at the LHC.

The linear e^+e^- colliders results are well beyond the projections of the HL-LHC accuracies. Due to the fact that the theory uncertainties are not yet calculated for 380 GeV, the CLIC uncertainties contain a theory uncertainty of 3% corresponding to the maximal theory uncertainty at the threshold [132], which is a very conservative upper limit. As all couplings between top quarks and the electroweak gauge bosons are predicted to high precision by the SM, a stringent comparison between the observed and the predicted couplings can be performed. In many BSM models the top couplings to the electroweak interaction are substantially modified, for example in the case of composite Higgs models or extra dimension models with coupling modifications of several 10%, resulting in a large discovery potential for future e^+e^- colliders [32].

$\mathcal{CP}$-violating form factors

The statistical uncertainties of $\mathcal{A}_{\gamma,Z}^{Re/Im}$, presented in Table 6.5, are used to determine the statistical uncertainty of the real and imaginary parts of the $F_{2A}^{\gamma/Z}$ form factors by solving a system of linear equations formed by Equations 6.16 and 6.17. In the particular case of ILC, both beams are polarized, but one can calculate the effective polarization p from Equations 6.16 and 6.17, as follows:

$$P_{eff} = \frac{P_{e^-} - P_{e^+}}{1 - P_{e^-} P_{e^+}} \tag{6.22}$$

For the ILC at 500 GeV, $p = P_{eff} = \mp 0.887$. In the case of CLIC the effective polarization is just the polarization of the e^- beam, $p = P_{e^-} = \mp 0,8$.

The statistical uncertainties of the real and imaginary parts of $\mathcal{CP}$-violating form factors are given in Table 6.7. The precision at e^+e^- colliders is better than LHC by an order of magnitude, as shown in Figure 6.7. The 68% CL limits are typically of the order of 0.08.

The results of the full simulation are in agreement with the parton-level study performed for the TESLA TDR [133].

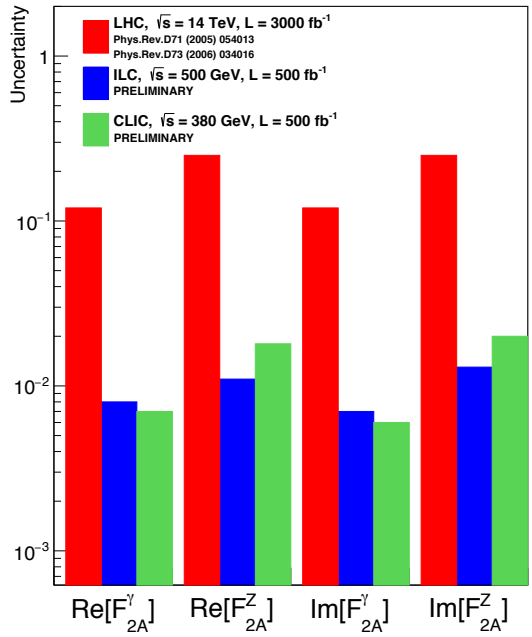

Figure 6.7: Graphical comparison of statistical precisions on $\mathcal{CP}$-violating form factors expected at the LHC from [131] and [19], and at the ILC and CLIC. The LHC results assume an integrated luminosity of $\mathcal{L} = 3000 fb^{-1}$ at 14 TeV. The results for ILC assume $\mathcal{L} = 500 fb^{-1}$ at 500 GeV and a beam polaristaion $P_{e^-} = \pm 0.8, P_{e^+} = \mp 0.3$. The results for CLIC assume $\mathcal{L} = 500 fb^{-1}$ at 380 GeV and a beam polaristaion $P_{e^-} = \pm 0.8, P_{e^+} = 0$

Table 6.7: Standard deviations of $\mathcal{CP}$-violating form factors derived from the statistical precisions on the $\mathcal{O}_{\pm}^{Re,Im}$ observables.

Form factor	**Re**$[F_{2A}^{\gamma}]$	**Re**$[F_{2A}^{Z}]$	**Im**$[F_{2A}^{\gamma}]$	**Im**$[F_{2A}^{Z}]$
SM value	0	0	0	0
LHC $\sqrt{s} = 14$ TeV, 3000fb^{-1}	0.12	0.25	0.12	0.25
TESLA TDR	0.007	0.008	0.008	0.010
ILC $\sqrt{s} = 500$ GeV, 500fb^{-1}	0.008	0.011	0.007	0.013
CLIC $\sqrt{s} = 380$ GeV, 500fb^{-1}	0.007	0.018	0.006	0.02

6.7 Summary and outlook

Top quark electro-weak couplings can be measured with high precision at future Linear Colliders. The prospects for ILC and CLIC are considerably better than those at the LHC even with an integrated luminosity of $\mathcal{L} = 3000\,\text{fb}^{-1}$ [131, 19]. The precision as obtained in the present study would allow to test a large number of models for physics beyond the Standard Model, in particular models with strong new physics such as RS or composite Higgs models.

The $\mathcal{CP}$-odd observables presented in [122, 118] allow to constrain the $\mathcal{CP}$-violating form factors of the interaction between top quarks and electroweak gauge bosons, yielding limits $\text{Re(Im)}[F_{2A}^{\gamma/Z}] \sim 0.01$.

To evaluate the prospects of the ILC luminosity upgrade scenario, with an integrated luminosity of 4000 fb^{-1} [44], the study of systematic errors, only partially addressed in this study, will become very important. Already from the achieved precision it is mandatory that systematics are controlled to the 1% level or better in particular for the measurement of the cross section. More sophisticated methods to extract the form factors may improve the sensitivity. The study presented in [134, 135] based on generated events suggests that by exploiting the polarization of the final state top quarks a simultaneous extraction of all ten form factors of Equation 6.2 to a precision below the percent level is feasible.

Conclusions

In this thesis several cooling options for future vertex detectors are explored. The combination of power pulsing, integrated micro-channels and air cooling may yield a cooling strategy with sufficient cooling perfomance and minimal impact on the material budget. The impact on the mechanical stability of ultra-thin, all-silicon DEPFET ladders is shown to be negligible.

A new jet reconstruction algorithm, the VLC algorithm, is presented that combines the positive features of classical e^+e^- algorithms, with the greater robustness of hadron collider algorithms. Comparative studies of its performance in realistic simulations of key benchmark channels show that it performs better than the classical algorithms and longitudinally invariant k_t.

Top quark electroweak couplings can be measured to % level precision at the ILC or CLIC, improving existing limits by two orders of magnitude and the HL-LHC expectations by one order. These measurements are very sensitive to new physics at scales well above the centre-of-mass energy of the collider, in particular for extensions of the SM with a new, strongly-coupled sector.

Appendices

Appendix A

Glossary

A.1 Acronyms

Acronyms

AIDA Advanced European Infrastructures for Detectors at Accelerators

ASIC Application-Specific Integrated Circuit

BSM Beyond Standard Model

CDR Conceptual Design Report

CERN The European Organization for Nuclear Research

CKM Cabibbo-Kobayashi-Maskawa

CLIC Compact Linear Collider

DBD Detailed Baseline Design

DEPFET DEPleted Field Effect Transistor

ECAL Electromagnetic Calorimeter

FE Finite-element

FFT Fast Fourier Transform

FSR Final State Radiation

FTD Forward Tracking Disk

HCAL Hadronic Calorimeter

IFIC Instituto de Física Corpuscular

ILC International Linear Collider

ILD International Large Detector

ISR Initial State Radiation

LEP Large Electron-Positron Collider

LHC Large Hadron Collider

MCC Micro-Channel Cooling

PCB Printed Circuit Board

PFA Particle Flow Algorithm

PFO Particle Flow Object

PSD Power Spectral Density

QCD Quantum Chromodynamics

QED Quantum Electrodynamics

RMS Root Mean Square

SiD Silicon Detector

SIT Strip Inner Tracking Detector

SM Standard Model

SSB Spontaneous Symmetry Breaking

TDR Technichal Design Report

TPC time-projection chamber

VTX Vertex Detector

A.2 Contributions

The studies presented in this thesis were performed in the framework of several large collaborations: the DEPFET detector R&D collaboration that develops active pixel detectors for future colliders, the Linear Collider Collaboration, that oversees the ILC and CLIC projects, the ILD detector concept group and the AIDA and AIDA2020 project financed by the European Union. All results build on R&D, detector design and simulation software and reconstruction software developed by a large group of people. Many of the results were obtained in close collaboration with others. In this section I indicate the most important collaborations.

A.2.1 Detector R&D

I am the main responsible for the characterization of the thermo-mechanical performance of thin silicon ladders reported Chapter 3. Apart from tests in the future collider laboratory at IFIC I report results that I obtained during stays at DESY and at CERN. The power pulsing system, presented in Section 3.2, was developed by José Manuel Deltoro as part of his final degree work in Electronic Engineering. The FE simulations in the MCC studies, the procurement of the MCC setup and the design and construction of the Carbon Fiber support disk are the work of Miguel Angel Villarejo. All mechanical samples were produced by Ladislav Andricek at MPG-HLL in Munich. The pressure tests were performed at CERN with help from Jerome Noel and Alessandor Mapelli at CERN. This work was funded partially by the FP7 project AIDA (grant agreement no. 262025.) and the H2020 project AIDA2020 (grant agreement no. 654168). I presented results from these studies at the 16^{th} DEPFET workshop (Kloster Seeon, 2014), at the tracker mechanics forum (Amsterdam, 2015), at the ALCW15 (KEK, 2015) and at the CLIC workshop (CERN, 2016). I am also the main author of the paper on integrated cooling in silicon detectors [56].

A.2.2 Jet Reconstruction

The results presented in this chapter are based on my work, published in Reference [88]. I developed the VLC algorithm together with my supervisors. Gavin Salam of CERN and Jesse Thaler of MIT have suggested modifications to the algorithm. The FASTJET implementation was done in collaboration with the authors of that package. I presented the results of this study at a number of international conferences, such as the Linear Collider Forum (Bonn, 2014) or the CLIC workshop (CERN, 2015), among which a poster presentation at ICHEP (Valencia, 2014) [89]. A further publication [90] is in preparation in collaboration with Rosa Simonnielo and Philipp Roloff of the CERN CLICdp group.

A.2.3 Top Physics

I started to study the top quark at ILC with $\sqrt{s} = 500$ GeV during my Master degree [111], in collaboration with my supervisors and François Richard, who enjoyed a sabbatical year at IFIC. In this time I acquired the knowledge and skills required

to perform a complex analysis on the full simulation of the detector. I carried out the entire analysis chain, together with Jeremy Rouene of LAL, of the the top quark couplings studies at ILC with $\sqrt{s} = 500$ GeV. It gave rise to an internal note [33] and a formal publication [100]. This result is part of the ILCTDR and physics case. I also was the main analyser in the results published by the IFIC future colliders group [112].

Later, I adapted the ILC analysis for CLIC $t\bar{t}$ events at $\sqrt{s} = 380$ GeV with help from Philipp Roloff of CLICdp group at CERN. These results have been included in the new "Staging baseline document of CLIC" [45]. A paper on the $\mathcal{CP}$-violating top quark couplings is in preparation with the collaboration of the LAL group and theorists. I presented these results at several international conferences and workshops, such as the ECFA (DESY, 2013), the LC Top Workshop (Paris, 2014) or ICHEP (Valencia, 2014) [113].

Plenary talks

- *Top Physics at CLIC*, on behalf of the CLICdp collaboration, at the CLIC workshop 2016 at CERN.
- *Overview of CLIC Physics and Detectors*, on behalf of the CLICdp collaboration, at the ECFA international conference 2016 in Santander.

Appendix B

Standard Model formalism

B.1 Local Gauge Symmetries

B.1.1 Quantum Electrodynamcis

The Lagrangian that describes a free Dirac fermion $\psi(x)$ and the electromagnetic photon field A_μ is:

$$\mathcal{L}_{em} = \bar{\psi}(x)(i\gamma^\mu D_\mu - m)\psi(x) - \frac{1}{4}F_{\mu\nu}F^{\mu\nu}, \tag{B.1}$$

where $D_\mu = \partial_\mu + iQeA_\mu(x)$ is the covariant derivative, Qe is the electric charge of $\psi(x)$ and $F_{\mu\nu} \equiv \partial_\mu A_\nu - \partial_\nu A_\mu$ is the strength tensor of the photon field [4].

This Lagrangian B.1 is invariant under local $U(1)_{em}$ transformations, $\psi(x) \rightarrow e^{iQ\theta}\psi(x)$, however is no longer invariant if one allows the phase transformation to depend on the space-time coordinate, i.e. under *local* phase redefinition $\theta = \theta(x)$, because a new term $\partial_\mu\theta(x)$ appears. The gauge principle requires an extra piece to the Lagrangian, transforming in such a way as to cancel that term. The gauge principle generates interaction between the Dirac fermion and the photon gauge field A_μ, which corresponds to the vertex of QED. A mass term for the photon field, $\mathcal{L}_m = \frac{1}{2}m^2A^\mu A_\mu$, is forbidden because it would violate the local $U(1)_{em}$ gauge invariance; therefore the photon is predicted to be massless.

$$A_\mu(x) \rightarrow A_\mu(x) - \frac{1}{e}\partial_\mu\theta(x) \tag{B.2}$$

B.1.2 Quantum Chromodynamics

The theory known as QCD is represented by the group $SU(3)_c$, the gauge group of the colour triplets. If one denotes q_f^α a quark field of colour α and flavour f. The free Lagrangian of a quark is given by:

$$\mathcal{L}_0 = \bar{q_f}(i\gamma^\mu D_\mu - m_f)q_f \tag{B.3}$$

Where $D_\mu = \partial_\mu - ig_s \frac{\lambda^a}{2} G_a^\mu(x)$ and g_s is the coupling constant[1]. Since we have now eight independent gauge parameters, eight different gauge bosons $G_a^\mu(x)$ appear, the so-called gluons.

The $SU(3)_c$ is a non-abelian gauge symmetry so the gauge transformation of the gluon fields is more complicated than the one obtained in QED for the photon. The matrices λ_a, called Gell-Mann matrices, are non-commutative, therefore all colour-triplet quark flavours couple to the gluon fields with exactly the same interaction strength. To build a gauge-invariant kinetic term for the gluon fields, the corresponding field strengths should be:

$$G_{\mu\nu}^a = \partial_\mu G_\nu^a - \partial_\nu G_\mu^a - g f_{abc} G_\mu^b G_\nu^c \tag{B.4}$$

where f_{abc} are the structure constants of $SU(3)_C$. This way the kinetic term proportional to $G_{\mu\nu}^a G_a^{\mu\nu}$ is invariant and the QCD Lagrangian can be written as follows:

$$\mathcal{L}_{QCD} = \sum_f \bar{q}_f (i\gamma^\mu D_\mu - m_f) q_f - \frac{1}{4} G_{\mu\nu}^a G_a^{\mu\nu} \tag{B.5}$$

The $SU(3)_C$ gauge symmetry forbids to add a mass term for the gluon fields, $\frac{1}{2} m_G^2 G_a^\mu G_\mu^a$, because it is not invariant under the local transformation. The gauge bosons are, therefore, massless spin-1 particles.

B.2 Electroweak theory

Analogous to the QED and QCD cases, the Lagrangian of a fermion $\psi_j(x)$

$$\mathcal{L}_0 = \sum_{j=1}^{3} i\bar{\psi}_j(x) \gamma^\mu D_\mu \psi_j(x) \tag{B.6}$$

must now be invariant under local $SU(2)_L \otimes U(1)_Y$ phase transformations. It gives rise to four gauge bosons and the covariant derivative is defined as follows:

$$\begin{aligned} D_\mu \psi_L(x) &\equiv \left[\partial_\mu - ig\widetilde{W}_\mu(x) + ig' Y B_\mu(x)\right] \psi_L(x) \\ D_\mu \psi_R(x) &\equiv \left[\partial_\mu + ig' Y B_\mu(x)\right] \psi_R(x) \end{aligned} \tag{B.7}$$

where $\widetilde{W}_\mu(x) \equiv \frac{\sigma_i}{2} W_\mu^i(x) (i = 1, 2, 3)$ denotes the $SU(2)_L$ matrix field and B_μ the scalar field of $U(1)_Y$. Thus we have exactly 4 gauge fields to describe the $W^\pm$, Z and γ. Notice that the multiplets $\psi_{L,R}$ couplings to the B_μ are completely free as in QED, i.e., the hypercharges Y can be arbitrary. However this freedom does not exist for the W_μ^i because there is only a unique $SU(2)_L$ coupling g. Now in order to build the gauge-invariant kinetic term of the Lagrangian, the corresponding field strengths will be:

[1] In a SU(N) group the index a takes the values: $a = 1, 2, ..., N^2 - 1$. For $N = 3$, $a = 1, 2, ..., 8$

$$B_{\mu\nu} \equiv \quad \partial_\mu B_\nu - \partial_\nu B_\mu \tag{B.8}$$

$$\widetilde{W}_{\mu\nu} \equiv \quad \partial_\mu \widetilde{W}_\nu - \partial_\nu \widetilde{W}_\mu \quad + ig\left[\widetilde{W}_\mu, \widetilde{W}_\nu\right] \tag{B.9}$$

Therefore, the properly normalized kinetic Lagrangian taken from [4] is

$$\mathcal{L}_{kin} = -\frac{1}{4} B_{\mu\nu} B^{\mu\nu} - \frac{1}{4} W^i_{\mu\nu} W_i^{\mu\nu} \tag{B.10}$$

The quadratic piece of $W^i_{\mu\nu}$ gives rise to cubic and quartic self-interactions among the gauge boson fields. A mass term for the bosons is forbidden by the gauge symmetry. Fermionic masses are not permitted either, because they would mix the left- and right-handed fields and would therefore produce an explicit breaking of the gauge symmetry.

B.2.1 Charged and neutral currents

The Lagrangian B.6 contains interactions of the fermion fields (quarks and leptons) with the gauge bosons,

$$-g\psi_1 \gamma^\mu \widetilde{W}_\mu - g' B_\mu \sum_{j=1}^{3} y_j \bar{\psi}_j(x) \gamma^\mu \psi_j(x) \tag{B.11}$$

The $SU(2)_L$ matrix leads to charged-current interactions with the boson fields $W^\pm_\mu = W^1_\mu \mp i W^2_\mu/\sqrt{2}$ obtained from Pauli matrices $\sigma_\pm = \frac{1}{2}(\sigma_1 + i\sigma_2)$, thus the charged part can be identified with a $g/\sqrt{2}$ coupling and the Lagrangian term of charged currents is

$$\mathcal{L}_{CC} = -\frac{g}{2\sqrt{2}} \{W_\mu [\bar{u}\gamma^\mu(1-\gamma_5)d + \bar{\nu_e}\gamma^\mu(1-\gamma_5)e] + h.c.\} \tag{B.12}$$

where $(1-\gamma_5)/2$ denotes the left-handed character type of the interacting fermions.

On the other hand the right term of B.11 contains interactions with the neutral fields W^3_μ and B_μ. In order to identify these bosons with Z and γ one can adopt the following parametrization

$$\begin{aligned} A_\mu &= \sin\theta_W W^3_\mu + \cos\theta_W B_\mu \\ Z_\mu &= \cos\theta_W W^3_\mu - \sin\theta_W B_\mu \end{aligned} \tag{B.13}$$

where A_μ and Z_μ are now the physical states of the γ and Z boson. θ_W is the Weinberg or weak mixing angle.

Using the relation 1.6, the neutral-current Lagrangian can be written in terms of the more usual fermion fields[4]

$$\mathcal{L}^Z_{NC} = -\frac{e}{2\sin\theta_W \cos\theta_W} Z_\mu \sum_f \bar{f}\gamma^\mu(v_f - a_f\gamma_5) f \tag{B.14}$$

where $a_f = I_3^f$ and $v_f = I_3^f(1 - 4|Q_f|\sin^2\theta_W)$ are the neutral-current couplings of a fermion f to Z and γ.

Additionally, the Lagrangian of the Electroweak theory also generates cubic and quartic self-interactions among the gauge bosons

$$\begin{array}{c} \gamma, Z \to W^+W^- \\ W^+W^- \to W^+W^- \\ W^+W^- \to \gamma\gamma, ZZ \end{array} \tag{B.15}$$

B.2.2 Spontaneous Symmetry Breaking

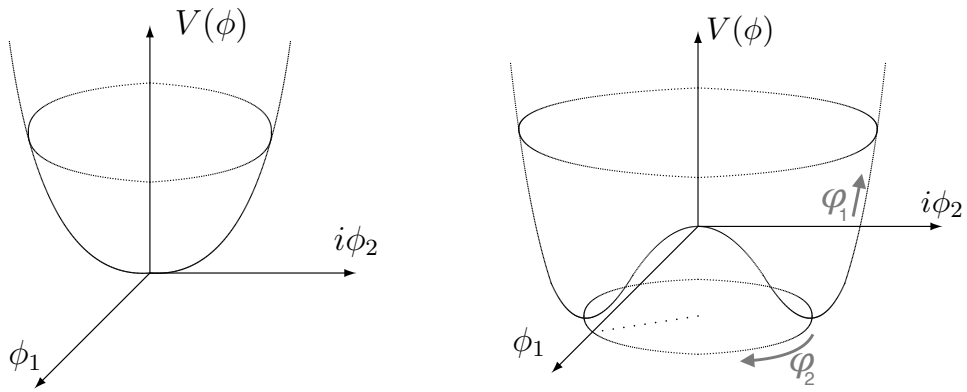

(a) For $\mu^2 > 0$ there is a unique ground state at $\phi = 0$.

(b) For $\mu^2 < 0$ the ground state is degenerate.

Figure B.1: Shape of the scalar potential $V(\phi)$ of the complex field $\phi = \frac{1}{\sqrt{2}}(\phi_1 + i\phi_2)$

Let us consider the following Lagrangian of a complex scalar field $\phi(x)$ under a quartic potential $V(\phi)$:

$$\mathcal{L} = \partial_\mu\phi^\dagger\partial^\mu\phi - V(\phi), \qquad V(\phi) = \mu^2\phi^\dagger\phi + h\left(\phi^\dagger\phi\right)^2 \tag{B.16}$$

In order to obtain a ground state the potential should be bounded from below, i.e., $h > 0$. Thus for the quadratic term $\mu^2\phi^\dagger\phi$ there are two solutions, shown in Figure B.1. In the case where $\mu^2 > 0$, the Lagrangian describes a scalar particle of mass μ with a quartic self-coupling h. However for $\mu^2 < 0$ the minimum is obtained satisfying

$$|\phi_0| = \sqrt{\frac{-\mu^2}{2h}} \equiv \frac{v}{\sqrt{2}} > 0, \qquad V(\phi_0) = -\frac{h}{4}v^4 \tag{B.17}$$

Let us now consider the invariance of the Lagrangian under $U(1)$ phase transformations. There is an infinite number of degenerate states of minimum energy $\phi_0(x) = \frac{v}{\sqrt{2}}\exp\{i\theta\}$. If one choose a particular solution, for instance $\theta = 0$ as ground

state, the symmetry gets spontaneously broken. The excitations over the ground state can be decomposed as

$$\phi(x) = \frac{1}{\sqrt{2}} \left[v + \varphi_1(x) + i\varphi_2(x) \right] \tag{B.18}$$

Being $\varphi_1(x)$ and $\varphi_2(x)$ are real fields, the Lagrangian takes the form [4]

$$\begin{array}{l} \mathcal{L} = \frac{1}{2}(\partial_\mu \varphi_1)^2 + \frac{1}{2}(\partial_\mu \varphi_2)^2 - V(\phi) \\ V(\phi) = -\frac{h}{4} v^4 - \mu^2 \varphi_1^2 + hv\varphi_1(\varphi_1^2 + \varphi_2^2) + \frac{h}{4}(\varphi_1^2 + \varphi_2^2)^2 \end{array} \tag{B.19}$$

where φ_1 describes a massive state of mass $m_{\varphi_1} = -2\mu^2$ and corresponds to radial excitations of the original field. On the other hand φ_2 is massless and describes excitations around a flat direction in the potential, i.e., into states with the same energy as the chosen ground state.

B.2.3 Higgs mechanism

Let's consider the Higgs field as an $SU(2)_L$ doublet of complex scalar fields

$$\phi(x) \equiv \begin{pmatrix} \phi^{(+)}(x) \\ \phi^{(0)}(x) \end{pmatrix} \tag{B.20}$$

This field has weak isospin $I_\phi = 1/2$ and weak hypercharge $Y_\phi = 1$. The upper component $\phi^{(+)}$ has $I_3^{(+)} = +1/2$, $Y_{(+)} = 1$ and therefore charge $Q_{(+)} = +1$, whereas the lower component $\phi^{(0)}$ has $I_3^{(0)} = -1/2$, $Y_{(0)} = 1$ and charge $Q_{(0)} = 0$.

The covariant derivative of the Higgs field and the gauged Lagrangian are

$$\begin{array}{ll} \mathcal{L} = (D_\mu \phi)^\dagger D^\mu \phi - \mu^2 \phi^\dagger \phi + h \left(\phi^\dagger \phi \right)^2 & (h > 0, \mu^2 < 0) \\ D^\mu \phi = \left[\partial^\mu + ig\widetilde{W}^\mu + ig' Y_\phi B^\mu \right] & \end{array} \tag{B.21}$$

which is invariant under local $SU(2)_L \otimes U(1)_Y$ transformations. As in the Goldstone model the potential has an infinite set of degenerate states with minimum energy, the vacuum state is chosen to be:

$$\phi_0 = \frac{1}{\sqrt{2}} \begin{pmatrix} 0 \\ v \end{pmatrix}, \qquad v^2 = -\frac{\mu^2}{h} \tag{B.22}$$

The charge of ϕ_0 is 0. This guarantees that the electromagnetic gauge group $U(1)_{em}$, which is generated by Q, is unaffected by the Higgs mechanism, so that the photon remains massless. According to the Goldstone theorem three massless states $\theta^i(x)$ should then appear and a massive Higgs field $H(x)$.

Now, the parametrization of the scalar doublet in the general form is

$$\phi(x) = \exp\left\{ i \frac{\sigma_i}{2} \theta^i(x) \right\} \frac{1}{\sqrt{2}} \begin{pmatrix} 0 \\ v + H(x) \end{pmatrix}, \tag{B.23}$$

If one takes the physical (unitary) gauge $\theta^i(x) = 0$, the kinetic part of the Lagrangian in equation B.21 becomes [4]

$$\mathcal{L} \to \frac{1}{2}(\partial_\mu H)^2 + (v+H)^2 \left\{ \frac{g^2}{4} W_\mu^\dagger W^\mu + \frac{g^2}{8\cos^2\theta_W} Z_\mu Z^\mu \right\} \tag{B.24}$$

In order to create the masses m_W and m_Z, the Higgs mechanism is applied to the gauge group $SU(2)_L \otimes U(1)_Y$ of the electroweak interactions. Those, W and Z, gauge bosons belonging to the fields W_μ and Z_μ have acquired masses:

$$M_Z \cos\theta_W = M_W = \frac{1}{2} v g \tag{B.25}$$

whereas the mass associated to the photon A_μ field is $M_\gamma = 0$.

Decomposing the kinetic term of Lagrangian B.21 for the Higgs field, it takes the form

$$\mathcal{L}_{Higgs} \to \frac{1}{2}(\partial_\mu H)^2 - \frac{1}{2} M_H^2 H^2 - \frac{M_H^2}{2v} H^3 - \frac{M_H^2}{8v^2} H^4 \tag{B.26}$$

and the Higgs mass is given by

$$M_H = \sqrt{-2\mu^2} = \sqrt{2h}v \tag{B.27}$$

as a function of the vacuum expectation value v.

Since left-handed fermions are incorporated in an $SU(2)_L$ doublet and right-handed fermions form a singlet under this group, a fermionic mass term $\mathcal{L}_m = -m\bar{\psi}\psi = -m(\bar{\psi}_L\psi_R + \bar{\psi}_R\psi_L)$ is not allowed since it breaks the gauge symmetry of $SU(2)_L$.

The Higgs field is a doublet of $SU(2)_L$, and can thus be used to write a gauge-invariant fermion-scalar Yukawa coupling. Let's consider only the first family of fermions in equation 1.5

$$\mathcal{L}_{fermions} = -\lambda_d(\bar{u}, \bar{d})_L \phi d_R - \lambda_u(\bar{u}, \bar{d})_L \phi^c u_R - \lambda_e(\bar{\nu}_e, \bar{e})_L \phi e_R + \text{h.c.} \tag{B.28}$$

where ϕ is the higgs field B.20 and $\phi^c \equiv i\sigma_2\phi^*$ is the $\mathcal{C}$-conjugate.

This Yukawa-type Lagrangian could be written in a simpler form taking the unitary gauge

$$\mathcal{L}_{fermions} = -\frac{1}{\sqrt{2}}(v+H)\left\{\lambda_d \bar{d}d + \lambda_u \bar{u}u + \lambda_e \bar{e}e\right\} \tag{B.29}$$

Now the identification of the fermion masses is trivial being:

$$m_d = \lambda_d \frac{v}{\sqrt{2}}, \qquad m_u = \lambda_u \frac{v}{\sqrt{2}}, \qquad m_e = \lambda_e \frac{v}{\sqrt{2}} \tag{B.30}$$

The mass of the second and third families of quarks and fermions can be deduced through the same procedure. Therefore, the SSB generates also fermion masses.

Appendix C

Analysis of $e^+e^- \to t\bar{t}$ and top quark form factors

C.1 Selection of $t\bar{t}$ events at 500 GeV

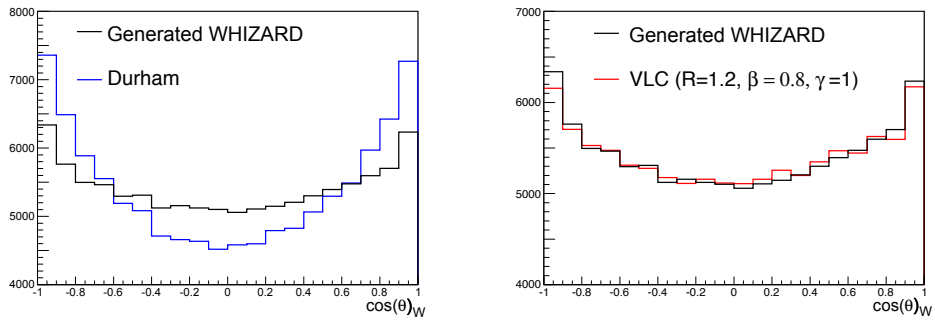

(a) Durham

(b) VLC, $R = 1.2, \beta = 0.8, \gamma = 1$

Figure C.1: The polar angle distribution of the hadronically decaying W for a classical e^+e^- algorithm (Durham) and a robust algorithm (VLC).

Figure C.1 shows the reconstructed polar angle distribution of the hadronically decaying W boson from $t\bar{t}$ pairs compared with the generated distribution. The result is shown for the "traditional" Durham [136] algorithm and for the VLC algorithm with a jet radius of $R = 1.2$ and $\beta = 0.8$, $\gamma = 1$. The improvement achieved by the VLC algorithm is obvious. Further beam induced background such as electron-positron pairs have been studied with more detail in [88].

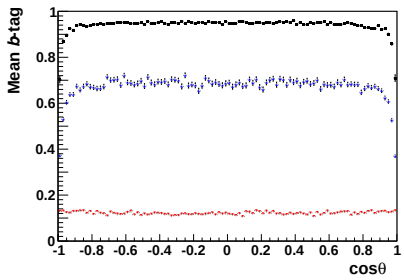

Figure C.2: The b-tag values as a function of the polar angle of the jets. The two highest b-tag values (black and blue dots) are associated to b quark jets. The third set of values (red dots) is obtained for jets from light quarks.

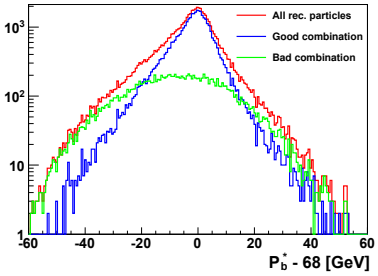

(a) Momentum of b jet at top rest frame.

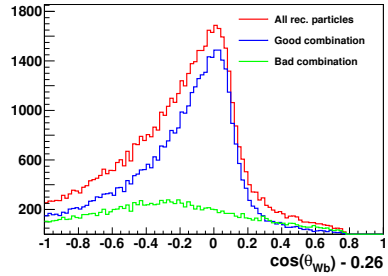

(b) Angle between b-jet and W.

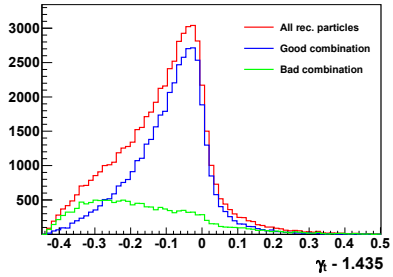

(c) Lorentz factor of the top quark.

Figure C.3: Distributions of the momentum of the b quark jet in the centre-of-mass frame of the t quark, p_b^*, cosine of the angle θ_{bW} between the b quark and the W boson and Lorentz factor of the top quark to define the quantity χ^2, see Equation 6.20, for the selection of well reconstructed events in case of $P(e^-), P(e^+) = -1, +1$ beam polarisation.

C.2 Optimal observables $\mathcal{O}_{\pm}^{Re,Im}$ and $\mathcal{CP}$-violating asymmetries

Table C.1: Mean values and statistical uncertainties of the optimal observables, $\mathcal{O}_{\pm}^{Re,Im}$, for ILC 500 GeV and $P(e^-), P(e^+) = +0.8, -0.3$

ILC $\sqrt{s}$ = 500 GeV, 500fb^{-1}, $P(e^-), P(e^+) = +0.8, -0.3$				
$\mathcal{CP}$ obs.	**Generated**	**δ_{stat}**	**Reconstructed**	**δ_{stat}**
$\langle \mathcal{O}_{+}^{Re} \rangle_R$	-0.0037	0.002	0.0031	0.003
$\langle \mathcal{O}_{-}^{Re} \rangle_R$	-0.0016	0.002	0.00057	0.003
$\langle \mathcal{O}_{+}^{Im} \rangle_R$	0.094	0.002	0.107	0.003
$\langle \mathcal{O}_{-}^{Im} \rangle_R$	0.094	0.002	0.114	0.003

Table C.2: Mean values and statistical uncertainties of the optimal observables, $\mathcal{O}_{\pm}^{Re,Im}$, for CLIC 380 GeV and $P(e^-), P(e^+) = -0.8, 0$

CLIC $\sqrt{s}$ = 380 GeV, 500fb^{-1}, $P(e^-), P(e^+) = -0.8, 0$				
$\mathcal{CP}$ obs.	**Generated**	**δ_{stat}**	**Reconstructed**	**δ_{stat}**
$\langle \mathcal{O}_{+}^{Re} \rangle_L$	0.00004	0.002	0.0013	0.002
$\langle \mathcal{O}_{-}^{Re} \rangle_L$	0.0033	0.002	0.0014	0.002
$\langle \mathcal{O}_{+}^{Im} \rangle_L$	-0.041	0.002	-0.032	0.002
$\langle \mathcal{O}_{-}^{Im} \rangle_L$	-0.032	0.002	-0.032	0.002

Table C.3: Mean values and statistical uncertainties of the optimal observables, $\mathcal{O}_{\pm}^{Re,Im}$, for CLIC 380 GeV and $P(e^-), P(e^+) = +0.8, 0$

CLIC $\sqrt{s}$ = 380 GeV, 500fb^{-1}, $P(e^-), P(e^+) = +0.8, 0$				
$\mathcal{CP}$ obs.	**Generated**	**δ_{stat}**	**Reconstructed**	**δ_{stat}**
$\langle \mathcal{O}_{+}^{Re} \rangle_R$	0.0005	0.002	0.0036	0.003
$\langle \mathcal{O}_{-}^{Re} \rangle_R$	-0.0024	0.002	-0.0036	0.003
$\langle \mathcal{O}_{+}^{Im} \rangle_R$	0.026	0.002	0.023	0.003
$\langle \mathcal{O}_{-}^{Im} \rangle_R$	0.032	0.002	0.025	0.003

C.3 Generation of non-zero $\mathcal{CP}$-violating couplings in MADGRAPH

A tool developed by Gupta and Valencia [128] allows to generate non-zero $\mathcal{CP}$-violating terms in a SM environment in MADGRAPH [137]. The real part of the top quark couplings $\mathrm{Re}[d_{\gamma,Z}(s)]$, from Equation 6.9, can be tuned freely and independently. In order to evaluate the impact of non-zero terms in the $\mathcal{CP}$-violating asymmetries, $\mathcal{A}^{Re}_{\gamma,Z}$, two cases are considered, ($\mathrm{Re}[d_\gamma] = 0$, $\mathrm{Re}[d_Z] \neq 0$) and ($\mathrm{Re}[d_Z] = 0$, $\mathrm{Re}[d_\gamma] \neq 0$).

That gives rise to the expressions in Equations C.1 and C.2 for the asymmetries associated to Z and γ couplings.

$$\mathcal{A}^{Re}_{Z} = s_Z Re[d_Z] \tag{C.1}$$

$$\mathcal{A}^{Re}_{\gamma} = s_\gamma Re[d_\gamma] \tag{C.2}$$

where $s_{\gamma/Z}$ are the proportionality factors which govern the sensitivity of the asymmetries to non-zero couplings. According to Equation (6.16), $\mathcal{A}^{Re}_{Z,\gamma}$ is directly proportional to $Re(F^{Z\gamma}_{2A})$. Hence the $s_{\gamma,Z}$ factors are related to c_γ and KZ constants as shown in following equations.

$$\begin{aligned} \mathcal{A}^{Re}_{Z} &= c_\gamma KZ Re(F^{Z}_{2A}) \rightarrow s_Z \propto c_\gamma KZ \\ \mathcal{A}^{Re}_{\gamma} &= c_\gamma p Re(F^{\gamma}_{2A}) \rightarrow s_\gamma \propto c_\gamma p, \end{aligned} \tag{C.3}$$

giving rise to:

$$\frac{s_Z}{s_\gamma} = \frac{KZ}{p} = \frac{-0.6}{\pm 1} = \mp 0.6 \tag{C.4}$$

Following Tables C.4 and C.5 show the values for $\mathcal{A}^{Re}_{\gamma,Z}$ in a scan over different values of the top quark couplings $Re[d_{\gamma,Z}]$. The statistical uncertainty[1] of $\mathcal{A}^{Re}_{\gamma,Z}$ for $N_{events} = 10000$ results $\sim 7 \cdot 10^{-3}$.

Table C.4: $\mathcal{A}^{Re}_{Z}$ for non-zero values of $\mathrm{Re}[d_Z]$ and $\mathrm{Re}[d_\gamma] = 0$.

Re[d_Z] $\times 10^{-4}$ **(GeV^{-1})**	**1**	**2.5**	**5**	**7.5**	**10**
$\mathcal{A}^{Re}_{Z}(p=-1)$	-0.042	-0.108	-0.224	-0.292	-0.369
$\mathcal{A}^{Re}_{Z}(p=+1)$	-0.095	-0.128	-0.250	-0.343	-0.396

Values from previous tables are graphically represented in Figure C.4. The asymmetries depend linearly on the couplings in such a way that $s_{\gamma,Z}$ factors can be interpreted as the slope of the linear fit of these values. Results are compared to the prediction of Equation C.4 in Table C.6.

Table C.5: $\mathcal{A}_\gamma^{Re}$ for non-zero values of Re$[d_\gamma]$ and Re$[d_Z] = 0$.

Re$[d_\gamma]$ $\times 10^{-4}$ **(GeV**$^{-1}$**)**	**1**	**1.5**	**2.5**	**3.75**	**5**
$\mathcal{A}_\gamma^{Re}(p=-1)$	-0.053	-0.096	-0.194	-0.249	-0.302
$\mathcal{A}_\gamma^{Re}(p=+1)$	0.121	0.163	0.246	0.307	0.370

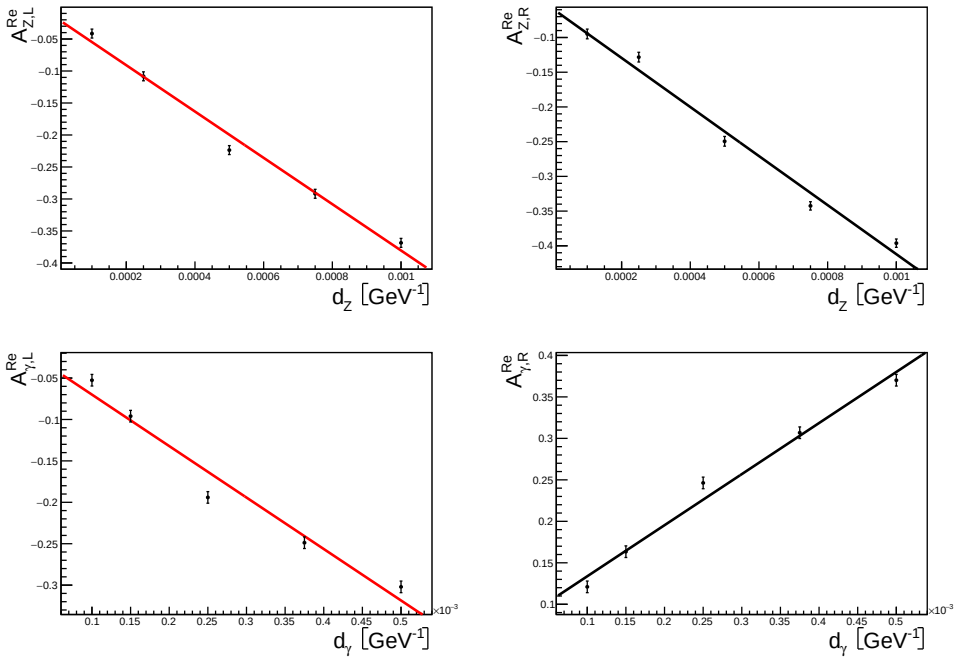

Figure C.4: Linear fit of $\mathcal{A}_{Z,\gamma}^{Re}$ for left-handed electron beam (left plots) and right-handed electron beam (right plots).

Table C.6: Measurement of the KZ parameter through linear fits

p	KZ/p	s_Z/s_γ
-1	0.6	0.58 ± 0.03
1	-0.6	-0.57 ± 0.02

The ratio of the measured slopes (s_Z/s_γ) is in good agreement with the values of KZ assumed in Section 6.3.2. The sign dependence due to the polarisation is also

[1]The statistical uncertainty of $\mathcal{O}_\pm^{Re}$ distributions is calculated as $\delta_{stat} = RMS/\sqrt{N_{events}}$. The δ_{stat} of $\mathcal{A}_{\gamma,Z}^{Re}$ is obtained by common error propagation.

confirmed.

The form factors defined in [128], $Re[d_{\gamma,Z}](s)$, are expressed in units of GeV^{-1} while electric and weak dipole moments, $\hat{d}_{\gamma,Z}(s)$, in [122] are dimensionless. In order to get consistency between both definitions, they must satisfy the following relation.

$$\hat{d}_{\gamma,Z}(s) = \frac{\sqrt{s}}{e} Re[d_{\gamma,Z}(s)] \tag{C.5}$$

On the other hand, a third definition of the F_{2A} form factors appears in Equations 6.16 and 6.17. Reference [100] connects this definition with $Re[d_{\gamma,Z}](s)$ as follows:

$$F_{2A}^{\gamma,Z}(s) = \frac{2m_t}{e} Re[d_{\gamma,Z}(s)] \tag{C.6}$$

Therefore to be consistent, both definitions must satisfy the relation:

$$\hat{d}_{\gamma,Z} = \frac{\sqrt{s}}{2m_t} F_{2A}^{\gamma,Z} \tag{C.7}$$

The factor $\sqrt{s}/2m_t$ must be taken into account to compare results from MADGRAPH studies and values predicted by theory. Thus the experimental slopes (s_Z/s_γ) can be as a function of the theoretical constants c_γ and KZ.

$$s_Z = \left(\frac{\sqrt{s}}{2m_t}\right) \frac{2m_t}{e} \cdot c_\gamma KZ = \frac{\sqrt{s}}{e} \cdot c_\gamma KZ \tag{C.8}$$

$$s_\gamma = \left(\frac{\sqrt{s}}{2m_t}\right) \frac{2m_t}{e} \cdot c_\gamma P = \frac{\sqrt{s}}{e} \cdot c_\gamma P \tag{C.9}$$

where $e = 0.302$ and $\sqrt{s} = 500$ GeV.

With this conversion a good agreement for small values of the couplings between the results in Figure C.4 and expectations presented in Reference [123] is found, as shown in Table C.7

Table C.7: Values of $s_{\gamma,Z}$ from the fit and expectation values from theory.

p	s_Z(fit)	s_Z(C.8)	s_γ(fit)	s_γ(C.9)
-1	-362 ± 10	-348	-621 ± 21	-579
1	-353± 9	-348	616 ± 21	579

With this second check, the value of $c_\gamma \sim 0.35$, assumed in 6.3.2, is roughly validated.

C.4 Covariance matrices

For completeness the underlying covariance matrices of the results presented in Section 6.6 are given in this appendix.

ILC $\sqrt{s} = 500$ GeV

- The covariance matrix resulting from the system of linear equations built for the Form Factors F_{1V}^{γ}, F_{1V}^{Z}, F_{1A}^{Z} reads:

$$\begin{bmatrix} var(F_{1V}^{\gamma}) & cov(F_{1V}^{\gamma}, F_{1V}^{Z}) & cov(F_{1V}^{\gamma}, F_{1A}^{Z}) \\ & var(F_{1V}^{Z}) & cov(F_{1V}^{Z}, F_{1A}^{Z}) \\ & & var(F_{1A}^{Z}) \end{bmatrix} = \begin{bmatrix} 0.260 & -0.043 & 0.506 \\ & 0.791 & 0.118 \\ & & 5.460 \end{bmatrix} \times 10^{-5}. \tag{C.10}$$

- The covariance matrix resulting from the system of linear equations built for the Form Factors F_{2V}^{γ}, F_{2V}^{Z} reads:

$$\begin{bmatrix} var(F_{2V}^{\gamma}) & cov(F_{2V}^{\gamma}, F_{2V}^{Z}) \\ & var(F_{2V}^{Z}) \end{bmatrix} = \begin{bmatrix} 0.160 & -0.046 \\ & 0.473 \end{bmatrix} \times 10^{-5}. \tag{C.11}$$

- The covariance matrix resulting from the system of linear equations built for the Couplings $g_L^{\gamma}, g_R^{\gamma}, g_L^{Z}, g_R^{Z}$ reads:

$$\begin{bmatrix} var(g_L^{\gamma}) & cov(g_L^{\gamma}, g_R^{\gamma}) & cov(g_L^{\gamma}, g_L^{Z}) & cov(g_L^{\gamma}, g_R^{Z}) \\ & var(g_R^{\gamma}) & cov(g_R^{\gamma}, g_L^{Z}) & cov(g_R^{\gamma}, g_R^{Z}) \\ & & var(g_L^{Z}) & cov(g_L^{Z}, g_R^{Z}) \\ & & & var(g_R^{Z}) \end{bmatrix} = \begin{bmatrix} 2.801 & -2.357 & -0.339 & -1.234 \\ & 2.949 & -0.780 & 2.247 \\ & & 5.988 & -4.691 \\ & & & 7.306 \end{bmatrix} \times 10^{-5}. \tag{C.12}$$

CLIC $\sqrt{s} = 380$ GeV

- The covariance matrix resulting from the system of linear equations built for the Form Factors F_{1V}^{γ}, F_{1V}^{Z}, F_{1A}^{Z} reads:

$$\begin{bmatrix} var(F_{1V}^{\gamma}) & cov(F_{1V}^{\gamma}, F_{1V}^{Z}) & cov(F_{1V}^{\gamma}, F_{1A}^{Z}) \\ & var(F_{1V}^{Z}) & cov(F_{1V}^{Z}, F_{1A}^{Z}) \\ & & var(F_{1A}^{Z}) \end{bmatrix} = \begin{bmatrix} 0.254 & -0.164 & 1.441 \\ & 1.077 & -0.846 \\ & & 38.083 \end{bmatrix} \times 10^{-5}. \tag{C.13}$$

- The covariance matrix resulting from the system of linear equations built for the Form Factors F_{2V}^{γ}, F_{2V}^{Z} reads:

$$\begin{bmatrix} var(F_{2V}^{\gamma}) & cov(F_{2V}^{\gamma}, F_{2V}^{Z}) \\ & var(F_{2V}^{Z}) \end{bmatrix} = \begin{bmatrix} 0.325 & -0.460 \\ & 1.710 \end{bmatrix} \times 10^{-5}. \tag{C.14}$$

- The covariance matrix resulting from the system of linear equations built for the Couplings $g_L^{\gamma}, g_R^{\gamma}, g_L^{Z}, g_R^{Z}$ reads:

$$\begin{bmatrix} var(g_L^{\gamma}) & cov(g_L^{\gamma}, g_R^{\gamma}) & cov(g_L^{\gamma}, g_L^{Z}) & cov(g_L^{\gamma}, g_R^{Z}) \\ & var(g_R^{\gamma}) & cov(g_R^{\gamma}, g_L^{Z}) & cov(g_R^{\gamma}, g_R^{Z}) \\ & & var(g_L^{Z}) & cov(g_L^{Z}, g_R^{Z}) \\ & & & var(g_R^{Z}) \end{bmatrix} = \begin{bmatrix} 2.297 & -2.142 & -1.042 & 0.562 \\ & 2.088 & 0.721 & -0.306 \\ & & 4.086 & -3.700 \\ & & & 3.746 \end{bmatrix} \times 10^{-4}. \tag{C.15}$$

Resumen

El concepto de partículas elementales o entidades elementales fue propuesto por primera vez por los antiguos griegos bajo el nombre de átomos. Sin embargo este concepto de componentes indivisibles de la materia evolucionó con el paso del tiempo. En la segunda mitad del siglo XIX, el estudio de los espectros atómicos de los materiales dio lugar a la formulación de la tabla periódica de los elementos por Mendeleiev. En los últimos años de este siglo diversos estudios pioneros con tubos de rayos catódicos, materiales radioactivos y placas fotográficas revolucionaron la física atómica. En 1895 W. C. Röentgen descubrió los conocidos rayos-X, mientras que Bequerel estudió la radiación emitida por materiales como el uranio. Poco tiempo después, J. J. Thomson descubrió el electrón y propuso el primer modelo atómico, que consistía en un nube de electrones y un elemento de carga positiva que neutralizaba la carga del átomo.

El nacimiento del átomo moderno

El inicio del nuevo siglo estuvo marcado por el descubrimiento de la ley de la radiación del cuerpo negro por Planck. La interpretación física de este fenómeno dio lugar a postular que la energía estaba cuantizada. En 1905 Einstein usó la constante de Planck h para explicar el efecto fotoeléctrico observado por Herz en 1887. Este efecto refiere a la emisión de electrones emitida por metales iluminados con luz. La energía de esos electrones depende de la frecuencia de la luz, no de su intensidad. La explicación de Einstein postula que una luz de frecuencia ν es compuesta de *cuantos* individuales -ahora conocidos como fotones- de energía $h\nu$.

Las investigaciones sobre radioactividad llevadas a cabo por Geiger, Marsden y Rutherford en 1911, que consistían en bombardear con partículas alfa (α)[2] una lámina fina de metal, demostraron que el átomo tiene un pequeño núcleo con una carga positiva de valor $Z|e|$. Dos años más tarde, el modelo atómico de Niels Bohr reprodujo los niveles de energía de los electrones y obtuvo el radio del átomo de hidrógeno, combinando la masa de electrones m_e y la carga de electrones e con la constante de Planck h. Posteriormente, el mismo Rutherford demostró que el núcleo de hidrógeno era un constituyente fundamental de todos los demás núcleos. Rompió un núcleo de nitrógeno con partículas α y extrajo núcleos de hidrógeno que más tarde se llamaron "protones".

[2]La partícula α es un átomo de Helio doblemente ionizado, es decir, con carga $+2$ y también se puede indicar como He^{2+}.

Durante los años 1924-1927, la mecánica cuántica se desarrolló rápidamente, desde las ondas de de Broglie hasta la mecánica de la matriz de Heisenberg expresada en la ecuación de Schrödinger y la formulación de Dirac de las amplitudes de transición. El problema de la estructura electrónica del átomo se redujo a un conjunto de ecuaciones diferenciales, aproximaciones que explicaban no sólo el hidrógeno, sino todos los átomos. A pesar del progreso, la estructura del núcleo siguió siendo un misterio. Hacia 1926 los físicos se dieron cuenta de que todas las partículas se dividían en dos clases según su momento angular intrínseco, conocido como "espín". Aquellas con espín de semientero (en unidades de $\hbar = h/2\pi$) se llaman fermiones, mientras que aquellas con espín de número entero se llaman bosones. Estos hechos fundamentales sobre el espín no podían conciliarse con la imagen predominante del núcleo de nitrógeno N_{14}, compuesto por 14 protones y 7 electrones. Como estas partículas son ambas fermiones, el núcleo debía ser un fermión con un espín semientero, pero se demostró que tenía espín 1. La incoherencia del espín del nitrógeno y el enigma de la composición del núcleo se resolvieron con el descubrimiento del neutrón por Chadwick en 1932. El experimento consistía en el bombardeo de berilio con partículas α. Mostró que la radiación eléctricamente neutra que se produce en el proceso consistía en partículas neutras con aproximadamente la misma masa que el protón, más tarde llamadas "neutrones". El átomo moderno estaba completo. Un núcleo con carga Z y un número de masa A está compuesto por Z protones y $A - Z$ neutrones rodeados por Z electrones.

El Modelo Estándar de la Física de Partículas

Durante el siglo XX, los descubrimientos de nuevas partículas y las medidas realizadas en los colisionadores, junto con el progreso de la física teórica, nos permitieron formular el Modelo Estándar (SM) de las interacciones entre los constituyentes de la materia.

El Modelo Estándar constituye uno de los mayores logros de la física moderna. Proporciona un marco teórico elegante, que es capaz de describir los hechos experimentales conocidos en la física de partículas con alta precisión. Es una teoría cuántica de campos relativista basada en el grupo de simetría $SU(3)_C \otimes SU(2)_L \otimes U(1)_Y$, que describe interacciones fuertes, débiles y electromagnéticas, a través del intercambio de campos *gauge* con espín 1. El desarrollo del SM fue impulsado por la interacción entre la teoría y el experimento. A pesar del impresionante éxito fenomenológico, el SM deja demasiadas preguntas sin respuesta para ser considerada como una descripción completa de las fuerzas fundamentales. No incorpora la teoría de la gravitación descrita por la relatividad general y no contiene ninguna partícula de materia oscura viable que posea todas las propiedades requeridas deducidas de la cosmología observacional. Tampoco incorpora oscilaciones de neutrinos y masas de neutrinos que no sean cero. Por esta razón el SM es a veces considerado como "la teoría de casi todo".

Toda la materia ordinaria que nos rodea está formada por partículas elementales. Estas partículas se producen en dos tipos básicos llamados quarks y leptones. Cada grupo consta de seis partículas, que están relacionadas en pares o "generaciones". Las partículas más ligeras y más estables constituyen la primera generación, mientras que las partículas más pesadas y menos estables pertenecen a la segunda y tercera generación. Toda la materia estable en el universo está formada por partículas que

pertenecen a la primera generación. Cualquier partícula más pesada decae rápidamente al siguiente nivel más estable. Los seis quarks se emparejan en las tres generaciones, los quarks up (u) y down (d) forman la primera generación, seguido por el charm (c) y los quarks strange (s), luego los quarks top (t) y bottom (b o beauty). Además, los quarks vienen en tres diferentes "colores" y sólo se mezclan de tal manera que forman objetos incoloros. Los seis leptones están dispuestos de manera similar en tres generaciones, el electrón, el muón, el tau y sus respectivos neutrinos, como se muestra en la Figura 6.5. El electrón, el muón y el tau tienen una carga eléctrica y una masa no despreciable, mientras que los neutrinos son eléctricamente neutros y tienen muy poca masa.

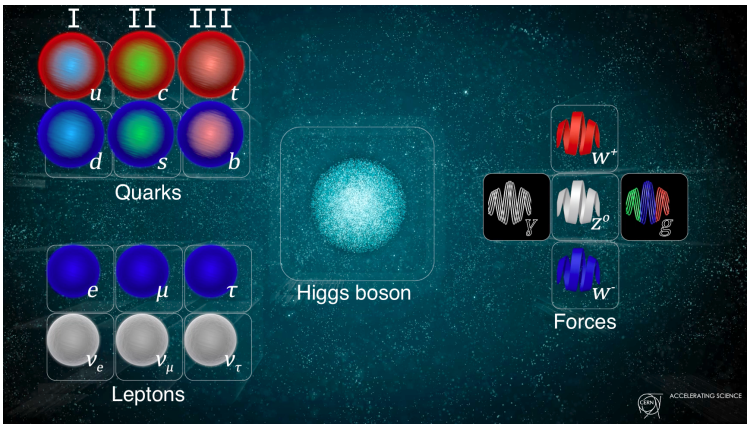

Figure 6.5: El contenido de partículas del modelo estándar. A la izquierda, los fermiones, los bloques de construcción de la materia, se subdividen en tres familias de quarks y leptones. A la derecha, bosones vectoriales que llevan las fuerzas electromagnéticas, débiles y fuertes. En el medio, el bosón de Higgs, responsable de proporcionar masa a todas las partículas masivas.

Hay cuatro fuerzas fundamentales en funcionamiento en el universo: la fuerza fuerte, la fuerza débil, la fuerza electromagnética y la fuerza gravitatoria. Actúan sobre rangos diferentes y tienen fuerzas diferentes. La gravedad es la más débil, pero es una interacción de largo alcance. La fuerza electromagnética es de largo alcance también, pero es muchas veces más fuerte que la gravedad. Las fuerzas débiles y fuertes son eficaces en un rango muy corto y sólo dominan al nivel de las partículas subatómicas. A pesar de su nombre, la fuerza débil es mucho más fuerte que la gravedad, pero es la más débil de las otras tres. La fuerza fuerte, como su nombre indica, es la más fuerte de las cuatro interacciones fundamentales. Tres de las fuerzas fundamentales resultan del intercambio de partículas portadoras de fuerza, que pertenecen a un grupo más amplio llamado "bosones". Las partículas de materia transfieren cantidades discretas de energía intercambiando bosones entre sí. Cada fuerza fundamental tiene su propio bosón correspondiente, la fuerza fuerte es llevada por el gluón, la fuerza electromagnética es llevada por el fotón y los bosones $W^{\pm}$ y Z son responsables de la fuerza débil. El quinto bosón es el bosón de Higgs, asociado con el campo de Higgs, que da masa a los leptones, quarks, bosones W y Z y al propio bosón de Higgs.

El quark Top

Esta tesis se centra básicamente en la física del quark top, la partícula más pesada conocida del Modelo Estándar, con un valor aproximadamente de 173 GeV, lo que equivale a la masa de un átomo de Tungsteno. El quark top fue descubierto en 1995 en los experimentos CDF y DØ en el colisionador Tevatron y recientemente estudiado por los experimentos ATLAS y CMS del Gran Colisionador de Hadrones (LHC). Las propiedades de esta partícula aún no son conocidas con el detalle requerido y por ello la convierten junto al boson de Higgs uno de los temas de estudio más interesantes de la física de partículas actual.

Aparte de la masa del quark top y de los elementos de la matriz de CKM[3], el SM predice todas las propiedades de los quarks top y de sus desintegraciones con alta precisión. Puesto que la vida útil del quark top es mucho más corta que el tiempo requerido para la hadronización, las propiedades del quark top se pueden medir directamente y normalmente con mucha menos incertidumbre que las de otros quarks, donde estas características se derivan de sus estados enlazados.

En el SM el quark top tiene los mismos números cuánticos e interacciones que todos los otros quarks de tipo *up*. Es el compañero isospin débil del quark b con espín $1/2$ y carga eléctrica $Q_t = +2/3$. El quark top zurdo es el componente superior del doblete débil del isospín y el componente de la mano derecha es un singlete débil de isospín. Es un triplete de color con respecto al grupo *gauge* $SU(3)_C$. Desde el punto de vista teórico, el quark top es absolutamente necesario para asegurar la cancelación de la anomalía quiral en el SM y por lo tanto para asegurar su consistencia como una teoría cuántica de campos. Las diferencias entre las propiedades medidas y las predicciones del SM conocidas con gran precisión proporcionan pruebas sensibles a nueva física más allá del SM.

Futuros colisionadores lineales

El descubrimiento del bosón de Higgs en el LHC fue un gran paso en nuestra comprensión de las interacciones fundamentales de la naturaleza y la estructura de la materia descrita por el Modelo Estándar. Con el fin de establecer el mecanismo de ruptura de simetría electrodébil, todas las propiedades del bosón de Higgs (masa, acoplamientos, amplitud de desintegración, espín) deben medirse con precisión. El LHC tiene excelentes perspectivas para los futuros períodos de funcionamiento 2 y 3 donde los haces protón-protón chocan con una energía de $\sqrt{s} = 13$ TeV desde mayo de 2015. En la década siguiente el LHC funcionará a una mayor luminosidad, conocido como el HL-LHC. A pesar de ello, se necesitan colisionadores e^+e^- para probar definitivamente la teoría electrodébil con una precisión sin precedentes. Un colisionador de leptones de alta energía también ofrece un programa de física muy interesante.

Los colisionadores e^+e^- de alta energía ya han sido instrumentos esenciales en el pasado para buscar los componentes fundamentales de la materia y estudiar sus

[3]La matriz de Cabibbo-Kobayashi-Maskawa (matriz CKM o matriz de mezcla de quarks) es una matriz unitaria que contiene información sobre la fuerza de las desintegraciones débiles que cambian el sabor, es decir aquellas que saltan de una generación de quarks a otra.

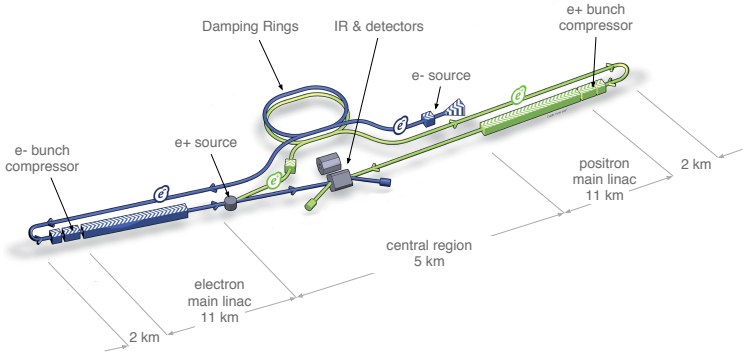

Figure 6.6: Imagen gráfica del colisionador e^+e^- ILC.

interacciones. Hoy en día, el diseño más avanzado para un futuro colisionador es el International Linear Collider (ILC), mostrado en la Figura 6.6, que está configurado para un rango de energía de centro de masa de $\sqrt{s}$ = 250 - 500 GeV (ampliable a 1 TeV) .

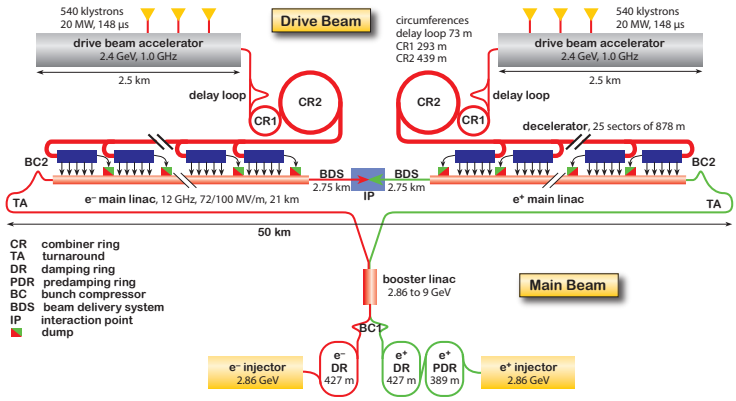

Figure 6.7: Imagen gráfica del colisionador e^+e^- CLIC para una energía de 3 TeV.

Una segunda propuesta, algo menos avanzada y más ambiciosa que el ILC, es el Compact Linear Collider (CLIC), un colisionador e^+e^- que alcanzaría energías de varios TeV. El diseño de este colisionador se muestra en la Figura 6.7. Este se basa en una técnica de aceleración de dos haces que proporcionaría colisiones e^+e^- de alta luminosidad cubriendo un rango de energías en centro de masas de 380 GeV a 3 TeV.

Estos futuros colisionadores lineales ofrecen la oportunidad de estudiar el quark top con una precisión sin precedentes. Las medidas de las propiedades del quark top son de especial interés, ya que el quark top es la partícula elemental más pesada del SM. Medidas de precisión de las propiedades del quark top en colisionadres e^+e^- prometen

ser altamente sensibles a la física más allá del SM.

Los detectores para futuros colisionadores han sido diseñados para lograr los requisitos del programa de física en todo el rango de energías desde unos pocos cientos de GeV hasta 3 TeV. Esto ha motivado a diseñar calorímetros altamente granulares y sistemas de seguimiento de partículas altamente eficientes con detectores y soportes de masa muy baja. Un esfuerzo mundial de I+D de detectores está en curso para satisfacer plenamente los exigentes requisitos. La generación actual de dispositivos de estado sólido sensibles a la posición tiene una mayor precisión, una mayor integración y menos material que las generaciones anteriores de detectores. Se han desarrollado soluciones de detectores para sensores de píxeles pequeños de 50 micras de grosor con una resolución de unas pocas micras. Los sensores ultra finos requieren nuevos conceptos de soporte mecánico y de refrigeración que mantengan un buen comportamiento termomecánico y no sobrepasen los límites de cantidad de material adicional.

Contenidos de la tesis

Esta tesis esta formada por tres partes complementarias. La primera está dedicada al I+D del concepto de detector para futuros colisionadores e^+e^- llamado International Large Detector (ILD), en particular, está dedicada a la región más interna del detector. En ella se ha llevado a cabo la caracterización termomecánica de sensores de silicio ultra finos y se ha diseñado y caracterizado un primer prototipo de FTD[4] en fibra de carbono. Además, se demuestra la viabilidad de utilizar micro circuitos integrados de refrigeración en los sensores activos de silicio.

El programa de física de precisión programado para futuros colisionadores requiere de excelentes detectores, pero también exige los mejores algoritmos de reconstrucción. En la segunda parte de la tesis la reconstrucción de *jets*[5] es estudiada a diferentes energías en centro de masa y un nuevo algoritmo de reconstrucción secuencial de *jets*, llamado VLC, es propuesto para hacer frente a los altos niveles de fondo $\gamma\gamma \to$ *hadrones* esperados en ILC y CLIC.

La última parte se centra en el potencial de los futuros colisionadores para estudiar la física del quark top. En esta parte de la tesis demuestro que ambos proyectos pueden poner limites a los acoplamientos electrodébiles del quark top, tanto los que violan la simetría $\mathcal{CP}$ como los que no, del orden del %. En una simulación completa del detector he estudiado el potencial de un colisionador e^+e^- con haces polarizados, una luminosidad integrada de 500 fb^{-1} y energías de centro de masa de $\sqrt{s} = 500$ GeV para ILC o $\sqrt{s} = 380$ GeV para CLIC. La sensibilidad a la nueva física es un orden de magnitud superior con respecto a lo que se espera del LHC.

[4] FTD ó Forward Tracker Disks, son discos de soporte para los sensores de silicio que rodean el tubo del haz y se encuentran en la parte más interna del detector.

[5] Conjunto de partículas producidas por numerosos procesos físicos encadenados que comparte un mismo origen.

Resultados y conclusiones

En esta tesis se exploran varias opciones de enfriamiento para futuros detectores de vértices. La combinación de fuentes de potencia pulsante, micro canales integrados y refrigeración por aire puede ser una estrategia de refrigeración con suficiente rendimiento de refrigeración y un impacto mínimo en la cantidad de material adicional. En la Figura (a) se muestra una imagen de un módulo de silicio con micro canales de refrigeración integrados y el conector impreso en 3D. El poder de refrigeración del agua a través de los micro canales se muestra en la Figura (b). El gradiente de temperatura del silicio se mantiene en valores pequeños para flujos del refrigerante relativamente bajos. El impacto en la estabilidad mecánica de los módulos DEPFET ultra-delgados y de todo el silicio se muestra como despreciable.

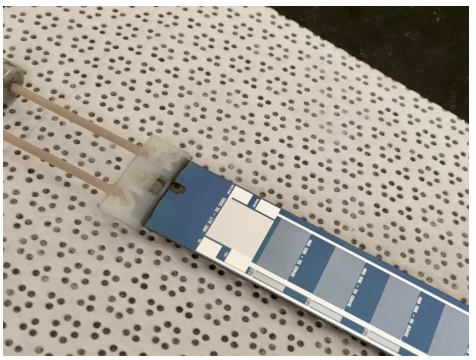

(a) Fotografía de un módulo de silicio con el circuito de refrigeración integrado y el conector impreso en 3D al circuito de refrigeración

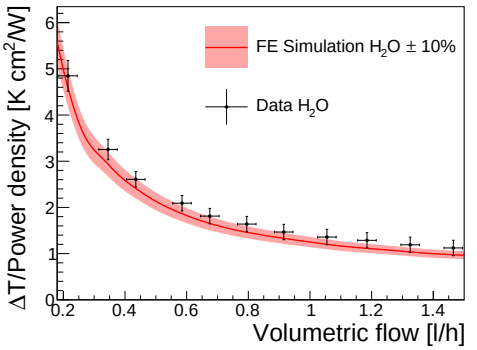

(b) Gradiente de temperatura del punto más caliente de la superficie del sensor dividido por la potencia disipada en función del caudal de agua.

Figure 6.8: I+D en sensores de silicio para la parte más interna del detector ILD para futuros colisionadores.

Por otro lado, un nuevo algoritmo de reconstrucción de *jets* es presentado, el algoritmo VLC, que combina las características positivas de los algoritmos clásicos para e^+e^-, con la mayor robustez de los algoritmos de colisionadores hadrónicos. Estudios comparativos de su potencial en las simulaciones de los principales sucesos físicos de referencia muestran que su comportamiento es mejor que los algoritmos clásicos y el longitudinalmente invariante k_t. La Figura 6.9 muestra la masa de un quark top reconstruido como un *jet* para sucesos $t\bar{t}$ a la energía de 3 TeV. Claramente se puede observar que el algoritmo VLC da lugar a un pico más nítido y más estrecho que los otros dos algoritmos. Esto es un ejemplo de la calidad de reconstrucción de *jets* que ofrece el algoritmo VLC en entornos donde hay mucho fondo de $\gamma\gamma \to hadrones$.

La nueva física puede modificar el vértice electrodébil $t\bar{t}X$ descrito en el modelo estándar por los acoplamientos *V*ectoriales y *A*xiales V y A a los bosones vectoriales $X = \gamma, Z$. Un comisionado de leptones permite sondear estos vértices directamente.

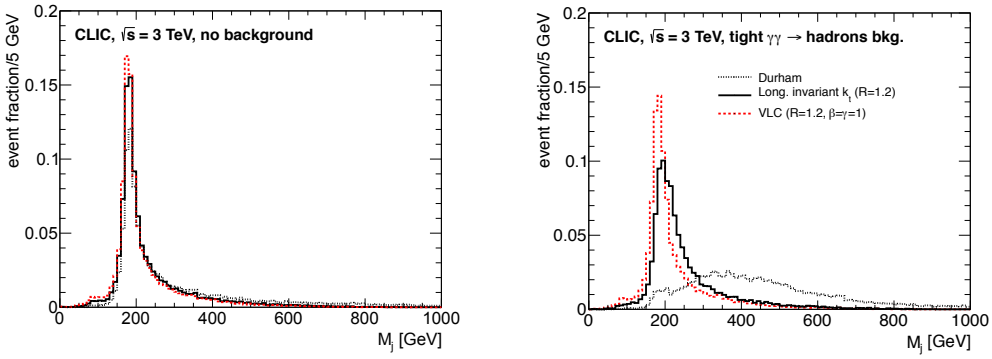

Figure 6.9: La distribución de la masa reconstruida del jet para sucesos de la desintegración hadrónica del par $t\bar{t}$ en CLIC a 3 TeV. (Izquierda) sin fondo $\gamma\gamma \to$ hadrones. (Derecha) el fondo $\gamma\gamma \to$ hadrones se ha superpuesto a la señal.

Al contrario de los colisionadores de hadrones, el proceso de producción de pares de quarks top, $e^+e^- \to t\bar{t}$ ocurre directamente a través de los vértices $t\bar{t}Z$ y $t\bar{t}\gamma$. No hay producción concurrente de QCD de pares de quarks top, lo que aumenta en gran medida el potencial de una medición limpia. Una parametrización del vértice $t\bar{t}X$

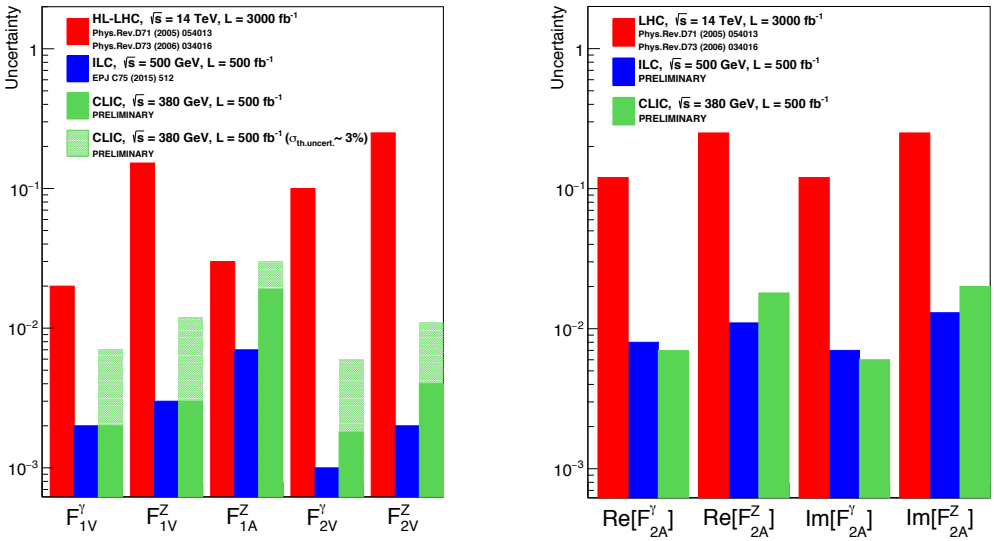

Figure 6.10: Comparación gráfica de las precisiones estadísticas de los acoplamientos electrodébiles del quark top en el HL-LHC, y en el ILC y CLIC.

válido para todos los órdenes de la teoría de las perturbaciones puede escribirse como:

$$\Gamma_{\mu}^{t\bar{t}X}(k^2,q,\bar{q}) = ie\left\{\gamma_{\mu}\left(F_{1V}^{X}(k^2)+\gamma_5 F_{1A}^{X}(k^2)\right) - \tfrac{\sigma_{\mu\nu}}{2m_t}(q+\bar{q})^{\nu}\left(iF_{2V}^{X}(k^2)+\gamma_5 F_{2A}^{X}(k^2)\right)\right\}, \tag{6.16}$$

donde F_{iC}^{X} con $i = 1, 2$ y $C = V, A$ son los factores de forma electrodébiles del quark top asociados a los bosones Z y γ. Todos ellos menos F_{2A}^{X} conservan la simetría $\mathcal{CP}$. Una medida precisa de las interacciones del quark top con el fotón (γ) o el bosón Z puede revelar indicios de nueva física. En la última parte de la tesis, la precisión con la que los factores de forma electrodébiles de los vértices $t\bar{t}Z$ y $t\bar{t}\gamma$ se puede determinar es estudiad. Se realiza un estudio de simulación completo de la reacción $e^+e^- \to Z/\gamma \to t\bar{t}$ a $\sqrt{s} = 500$ GeV con 80% de haz de electrones polarizados y hazes de positrones polarizados al 30% para ILC. El mismo estudio se repite en el entorno de CLIC a $\sqrt{s} = 380$ GeV con haces de electrones polarizados al 80% para evaluar el potencial de la física del quark top de ambos colisionadores.

Los acoplamientos electrodébiles del quark top se pueden medir con una precisión de nivel de % en el ILC o CLIC, mejorando los límites existentes en dos órdenes de magnitud y las expectativas del HL-LHC en un orden. La Figura 6.10 compara gráficamente las precisiones estadísticas esperadas para el LHC y las obtenidas en este estudio para ILC y CLIC.

Bibliography

[1] R. N. Cahn and G. Goldhaber, *The Experimental Foundations of Particle Physics:*. Cambridge University Press, Cambridge, 2 ed., 001, 2001, 10.1017/CBO9780511609923.

[2] A. Soria and E. Martínez, *Física de partículas y de astropartículas*. Educació (Universitat de València): Materials. Publicacions de la Universitat de València, 2014.

[3] Particle Data Group collaboration, K. A. Olive et al., *Review of Particle Physics*, *Chin. Phys.* **C38** (2014) 090001.

[4] A. Pich, *The Standard Model of Electroweak Interactions*, in *Proceedings, High-energy Physics. Proceedings, 18th European School (ESHEP 2010): Raseborg, Finland, June 20 - July 3, 2010*, pp. 1–50, 2012. 1201.0537.

[5] B. R. Stella and H.-J. Meyer, *Y(9.46 GeV) and the gluon discovery (a critical recollection of PLUTO results)*, *Eur. Phys. J.* **H36** (2011) 203–243, [1008.1869].

[6] Planck collaboration, P. A. R. Ade et al., *Planck 2013 results. I. Overview of products and scientific results*, *Astron. Astrophys.* **571** (2014) A1, [1303.5062].

[7] Particle Data Group collaboration, K. Nakamura et al., *Review of particle physics*, *J. Phys.* **G37** (2010) 075021.

[8] MuLan Collaboration collaboration, D. M. Webber et al., *Measurement of the positive muon lifetime and determination of the fermi constant to part-per-million precision*, *Phys. Rev. Lett.* **106** (Jan, 2011) 041803.

[9] ATLAS, CMS collaboration, G. Aad et al., *Combined Measurement of the Higgs Boson Mass in pp Collisions at $\sqrt{s} = 7$ and 8 TeV with the ATLAS and CMS Experiments*, *Phys. Rev. Lett.* **114** (2015) 191803, [1503.07589].

[10] ATLAS, CDF, CMS, D0 collaboration, *First combination of Tevatron and LHC measurements of the top-quark mass*, 1403.4427.

[11] G. 't Hooft, *Dimensional regularization and the renormalization group*, *Nuclear Physics B* **61** (1973) 455 – 468.

[12] Belle, BaBar collaboration, J. Walsh, *CP violation at the B factories*, *J. Phys. Conf. Ser.* **447** (2013) 012013.

[13] CMS collaboration, V. Khachatryan et al., *Measurement of the top quark mass using proton-proton data at $\sqrt{s} = 7$ and 8 TeV*, 1509.04044.

[14] A. Juste, S. Mantry, A. Mitov, A. Penin, P. Skands, E. Varnes et al., *Determination of the top quark mass circa 2013: methods, subtleties, perspectives*, *Eur. Phys. J.* **C74** (2014) 3119, [1310.0799].

[15] ATLAS collaboration, G. Aad et al., *Determination of the top-quark pole mass using $t\bar{t}$ + 1-jet events collected with the ATLAS experiment in 7 TeV pp collisions*, *JHEP* **10** (2015) 121, [1507.01769].

[16] M. Jezabek and J. H. Kuhn, *The Top width: Theoretical update*, *Phys. Rev.* **D48** (1993) R1910–R1913, [hep-ph/9302295].

[17] CMS collaboration, V. Khachatryan et al., *Measurement of the ratio $\mathcal{B}(t \to Wb)/\mathcal{B}(t \to Wq)$ in pp collisions at $\sqrt{s} = 8$ TeV*, *Phys. Lett.* **B736** (2014) 33–57, [1404.2292].

[18] D0 Collaboration collaboration, Abazov et al., *Improved determination of the width of the top quark*, *Phys. Rev. D* **85** (May, 2012) 091104.

[19] U. Baur, A. Juste, D. Rainwater and L. H. Orr, *Improved measurement of ttZ couplings at the CERN LHC*, *Phys. Rev.* **D73** (2006) 034016, [hep-ph/0512262].

[20] R. Röntsch and M. Schulze, *Probing top-Z dipole moments at the LHC and ILC*, 1501.05939.

[21] CMS collaboration, V. Khachatryan et al., *Measurement of the t-channel single-top-quark production cross section and of the $| V_{tb} |$ CKM matrix element in pp collisions at $\sqrt{s}$= 8 TeV*, *JHEP* **1406** (2014) 090, [1403.7366].

[22] J. Brod, A. Greljo, E. Stamou and P. Uttayarat, *Probing anomalous $t\bar{t}Z$ interactions with rare meson decays*, *JHEP* **1502** (2015) 141, [1408.0792].

[23] CDF Collaboration† and D0 Collaboration‡ collaboration, A. et al, *Combination of measurements of the top-quark pair production cross section from the tevatron collider*, *Phys. Rev. D* **89** (Apr, 2014) 072001.

[24] M. Czakon, P. Fiedler and A. Mitov, *Total Top-Quark Pair-Production Cross Section at Hadron Colliders Through $O(\alpha_S^4)$*, *Phys. Rev. Lett.* **110** (2013) 252004, [1303.6254].

[25] D0 collaboration, K. Bloom, *Recent Results on Top-Quark Physics at D0*, in *Proceedings, Meeting of the APS Division of Particles and Fields (DPF 2015): Ann Arbor, Michigan, USA, 4-8 Aug 2015*, 2015. 1510.06993.

[26] *Combination of ATLAS and CMS top quark pair cross section measurements in the eμ final state using proton-proton collisions at $\sqrt{s}$= 8 TeV*, Tech. Rep. ATLAS-CONF-2014-054, CERN, Geneva, Sep, 2014.

[27] CDF Collaboration† and D0 Collaboration‡ collaboration, Aaltonen et al., *Observation of s-channel production of single top quarks at the tevatron*, *Phys. Rev. Lett.* **112** (Jun, 2014) 231803.

[28] *Measurement of the Inclusive and Fiducial Cross-Section of Single Top-Quark t-Channel Events in pp Collisions at $\sqrt{s} = 8$ TeV*, Tech. Rep. ATLAS-CONF-2014-007, CERN, Geneva, Mar, 2014.

[29] G. Aad et al., *Evidence for the associated production of a w boson and a top quark in {ATLAS} at*, *Physics Letters B* **716** (2012) 142 – 159.

[30] J. Fuster, I. García, P. Gomis, M. Perelló, E. Ros and M. Vos, *Study of single top production at high energy electron positron colliders*, *The European Physical Journal C* **75** (2015) .

[31] F. Simon, *A First Look at the Impact of NNNLO Theory Uncertainties on Top Mass Measurements at the ILC*, in *International Workshop on Future Linear Colliders (LCWS15) Whistler, B.C., Canada, November 2-6, 2015*, 2016. 1603.04764.

[32] F. Richard, *Present and future constraints on top EW couplings*, 1403.2893.

[33] M. Amjad, S. Bilokin, M. Boronat, P. Doublet, T. Frisson, I. García et al., *A precise characterisation of the top quark electro-weak vertices at the ilc*, *The European Physical Journal C* **75** (2015) .

[34] A. Pomarol and J. Serra, *Top Quark Compositeness: Feasibility and Implications*, *Phys.Rev.* **D78** (2008) 074026, [0806.3247].

[35] A. Djouadi, G. Moreau and F. Richard, *Resolving the A(FB)**b puzzle in an extra dimensional model with an extended gauge structure*, *Nucl.Phys.* **B773** (2007) 43–64, [hep-ph/0610173].

[36] Y. Hosotani and M. Mabe, *Higgs boson mass and electroweak-gravity hierarchy from dynamical gauge-Higgs unification in the warped spacetime*, *Phys.Lett.* **B615** (2005) 257–265, [hep-ph/0503020].

[37] Y. Cui, T. Gherghetta and J. Stokes, *Fermion Masses in Emergent Electroweak Symmetry Breaking*, *JHEP* **1012** (2010) 075, [1006.3322].

[38] M. S. Carena, E. Ponton, J. Santiago and C. E. Wagner, *Light Kaluza Klein States in Randall-Sundrum Models with Custodial SU(2)*, *Nucl.Phys.* **B759** (2006) 202–227, [hep-ph/0607106].

[39] C. Grojean, O. Matsedonskyi and G. Panico, *Light top partners and precision physics*, 1306.4655.

[40] G. Panico, A. Wulzer, private communication, Possible deviations of couplings in framework described in [39].

[41] D. Barducci, S. De Curtis, S. Moretti and G. M. Pruna, *Top pair production at a future e^+e^- machine in a composite Higgs scenario*, 1504.05407.

[42] C. Berger, M. Perelstein and F. Petriello, *Top quark properties in little Higgs models*, hep-ph/0512053.

[43] M. Lamont, *LHC, HL-LHC and Beyond*, in *Proceedings, 2013 European Physical Society Conference on High Energy Physics (EPS-HEP 2013)*, vol. EPS-HEP2013, p. 149, 2013.

[44] ILC Parameters Joint Working Group collaboration, J. E. Brau, T. Barklow, J. Brau, K. Fujii, J. Gao, J. List et al., *500 GeV ILC Operating Scenarios*, in *Meeting of the APS Division of Particles and Fields (DPF 2015) Ann Arbor, Michigan, USA, August 4-8, 2015*, 2015. 1510.05739.

[45] CLICdp, CLIC collaboration, M. J. Boland et al., *Updated baseline for a staged Compact Linear Collider*, 1608.07537.

[46] ATLAS collaboration, G. Aad et al., *Observation of a new particle in the search for the Standard Model Higgs boson with the ATLAS detector at the LHC*, *Phys. Lett.* **B716** (2012) 1–29, [1207.7214].

[47] CMS collaboration, S. Chatrchyan et al., *Observation of a new boson at a mass of 125 GeV with the CMS experiment at the LHC*, *Phys. Lett.* **B716** (2012) 30–61, [1207.7235].

[48] H. Baer, T. Barklow, K. Fujii, Y. Gao, A. Hoang et al., *The International Linear Collider Technical Design Report - Volume 2: Physics*, 1306.6352.

[49] ECFA/DESY LC Physics Working Group collaboration, J. Aguilar-Saavedra et al., *TESLA: The Superconducting electron positron linear collider with an integrated x-ray laser laboratory. Technical design report. Part 3. Physics at an e+ e- linear collider*, hep-ph/0106315.

[50] ILC community collaboration, T. Behnke, J. E. Brau, B. Foster, J. Fuster, M. Harrison, J. M. Paterson et al., *The International Linear Collider Technical Design Report - Volume 1: Executive Summary*, 1306.6327.

[51] ILC community collaboration, C. Adolphsen, M. Barone, B. Barish, K. Buesser, P. Burrows, J. Carwardine et al., *The International Linear Collider Technical Design Report - Volume 3.I: Accelerator & in the Technical Design Phase*, 1306.6353.

[52] ILC community collaboration, C. Adolphsen, M. Barone, B. Barish, K. Buesser, P. Burrows, J. Carwardine et al., *The International Linear Collider Technical Design Report - Volume 3.II: Accelerator Baseline Design*, 1306.6328.

[53] L. Linssen, A. Miyamoto, M. Stanitzki and H. Weerts, *Physics and Detectors at CLIC: CLIC Conceptual Design Report*, 1202.5940.

[54] H. Abramowicz et al., *The International Linear Collider Technical Design Report - Volume 4: Detectors*, 1306.6329.

[55] J. Marshall and M. Thomson, *The Pandora Particle Flow Algorithm*, 1308.4537.

[56] L. Andricek, M. Boronat, I. Garcia, P. Gomis, C. Marinas, J. Ninkovic et al., *Integrated cooling channels in position-sensitive silicon detectors*, *JINST* **11** (2016) P06018, [1604.08776].

[57] DEPFET collaboration, O. Alonso et al., *DEPFET active pixel detectors for a future linear e^+e^- collider*, 1212.2160.

[58] DEPFET collaboration, C. Marinas, *DEPFET detectors for future electron-positron colliders*, *JINST* **10** (2015) C11002.

[59] R. Richter, L. Andricek, P. Fischer, K. Heinzinger, P. Lechner, G. Lutz et al., *Design and technology of depfet pixel sensors for linear collider applications*, *Nucl. Instr. and Meth. A* **511** (2003) 250 – 256.

[60] P. Fischer, M. Schumacher, M. Trimpl, J. Ulrici, N. Wermes, L. Andricek et al., *A DEPFET based pixel vertex detector for the detector at TESLA*, 2002.

[61] F. Duarte Ramos, W. Klempt and F.-X. Nuiry, "Experimental tests on the air cooling of the CLIC vertex detector." https://cds.cern.ch/record/2138963, Mar, 2016, CLICdp-Note-2016-002.

[62] L. Andricek, G. Lutz, R. H. Richter and M. Reiche, *Processing of ultra-thin silicon sensors for future e+ e- linear collider experiments*, *IEEE Trans.Nucl.Sci.* **51** (2004) 1117–1120.

[63] J. M. Deltoro, *Sistema de alimentación pulsado para la caracterización en el laboratorio de detectores para ILC*.

[64] M. Banzi, *Getting Started with Arduino*. Make Books - Imprint of: O'Reilly Media, Sebastopol, CA, ill ed., 2008.

[65] M. Vos and I. Vila, *Infrastructure for thermo-mechanical measurements*, Mar, 2014, AIDA-D9.1, https://cds.cern.ch/record/1692906.

[66] E. Curras, A. L. Virto, D. Moya, I. Vila, J. G. Carrion, M. Frovel et al., *Influence of the fiber coating type on the strain response of proton-irradiated fiber bragg gratings*, *IEEE Transactions on Nuclear Science* **59** (Aug, 2012) 937–942.

[67] M. Thomson, *Particle flow calorimetry and the pandorapfa algorithm*, *Nuclear Instruments and Methods in Physics Research Section A: Accelerators, Spectrometers, Detectors and Associated Equipment* **611** (2009) 25 – 40.

[68] R. Turchetta, *CMOS Monolithic Active Pixel Sensors (MAPS) for future vertex detectors*, *JINST* **1** (2006) P08004, [physics/0605238].

[69] F. M. Pitters, "The CLIC Detector Concept." https://cds.cern.ch/record/2221094, Oct, 2016, CLICdp-Conf-2016-009.

[70] F. Gaede, T. Behnke, N. Graf and T. Johnson, *LCIO - A persistency framework for linear collider simulation studies*, *ArXiv Physics e-prints* (June, 2003) , [physics/0306114].

[71] *GEAR - a geometry description toolkit for ILC reconstruction software*, http://ilcsoft.desy.de/portal/software_packages/gear.

[72] P. Mora de Freitas and H. Videau, *Detector simulation with MOKKA / GEANT4: Present and future*, in *Linear colliders. Proceedings, International Workshop on physics and experiments with future electron-positron linear colliders, LCWS 2002, Seogwipo, Jeju Island, Korea, August 26-30, 2002*, pp. 623–627, 2002.

[73] F. Gaede, *Marlin and lccd—software tools for the {ILC}*, *Nuclear Instruments and Methods in Physics Research Section A: Accelerators, Spectrometers, Detectors and Associated Equipment* **559** (2006) 177 – 180.

[74] F. Gaede, *Design document for alignment Toolkit with tight coupling to DD4hep*, Sep, 2016.

[75] GEANT4 collaboration, S. Agostinelli et al., *GEANT4: A Simulation toolkit*, *Nucl.Instrum.Meth.* **A506** (2003) 250–303.

[76] A. Waite, *Serial Input Output: the SIO Manual*, 2011.

[77] W. Kilian, T. Ohl and J. Reuter, *WHIZARD: Simulating Multi-Particle Processes at LHC and ILC*, *Eur. Phys. J.* **C71** (2011) 1742, [0708.4233].

[78] T. Sjöstrand, S. Mrenna and P. Skands, *Pythia 6.4 physics and manual*, *Journal of High Energy Physics* **2006** (2006) 026.

[79] D. Schulte, *Beam-Beam Simulations with GUINEA-PIG*, Mar, 1999, CERN-PS-99-014-LP, http://cds.cern.ch/record/382453.

[80] B. Li, K. Fujii and Y. Gao, *Kalman-filter-based track fitting in non-uniform magnetic field with segment-wise helical track model*, *Comput. Phys. Commun.* **185** (2014) 754–761, [1305.7300].

[81] J. Marshall and M. Thomson, *The Pandora software development kit for particle flow calorimetry*, *J.Phys.Conf.Ser.* **396** (2012) 022034.

[82] R. Walsh, *Flavour tag studies with the lcfivertex package*, Tech. Rep. arXiv:0901.4894, Feb, 2009.

[83] LCD collaboration, O. S. T. Barklow, D. Dannheim and D. Schulte, *Simulation of gamma-gamma to hadrons background at CLIC*, 2011, LCD-Note-2011-020.

[84] T. Barklow, D. Dannheim, M. O. Sahin and D. Schulte, *Simulation of $\gamma\gamma \to$ hadrons background at CLIC*, Feb, 2012, LCD-Note-2011-020, https://cds.cern.ch/record/1443518.

[85] J. S. Marshall, A. Münnich and M. A. Thomson, *Performance of Particle Flow Calorimetry at CLIC*, *Nucl. Instrum. Meth.* **A700** (2013) 153–162, [1209.4039].

[86] S. Moretti, L. Lonnblad and T. Sjostrand, *New and old jet clustering algorithms for electron - positron events*, *JHEP* **9808** (1998) 001, [hep-ph/9804296].

[87] M. Cacciari, G. P. Salam and G. Soyez, *The Anti-k(t) jet clustering algorithm*, *JHEP* **0804** (2008) 063, [0802.1189].

[88] M. Boronat, J. Fuster, I. García, E. Ros and M. Vos, *A robust jet reconstruction algorithm for high-energy lepton colliders*, *Physics Letters B* **750** (2015) 95 – 99.

[89] M. Boronat, J. Fuster, I. García, E. Ros and M. Vos, *A new jet reconstruction algorithm for lepton colliders*, *Nucl. Part. Phys. Proc.* **273-275** (2016) 2749–2751.

[90] M. Boronat, J. Fuster, I. Garcia, P. Roloff, R. Simoniello and M. Vos, *Jet reconstruction at high-energy lepton colliders*, 1607.05039.

[91] M. Boronat, J. Fuster, I. García, E. Ros and M. Vos, *A new jet reconstruction algorithm for lepton colliders*, *Nucl. Part. Phys. Proc.* **273-275** (2016) 2749–2751.

[92] JADE Collaboration collaboration, W. Bartel et al., *Experimental Studies on Multi-Jet Production in e+ e- Annihilation at PETRA Energies*, *Z.Phys.* **C33** (1986) 23.

[93] JADE Collaboration collaboration, S. Bethke et al., *Experimental Investigation of the Energy Dependence of the Strong Coupling Strength*, *Phys.Lett.* **B213** (1988) 235.

[94] S. Catani, Y. L. Dokshitzer, M. Olsson, G. Turnock and B. Webber, *New clustering algorithm for multi - jet cross-sections in e+ e- annihilation*, *Phys.Lett.* **B269** (1991) 432–438.

[95] S. Catani, Y. L. Dokshitzer, M. Seymour and B. Webber, *Longitudinally invariant K_t clustering algorithms for hadron hadron collisions*, *Nucl.Phys.* **B406** (1993) 187–224.

[96] S. D. Ellis and D. E. Soper, *Successive combination jet algorithm for hadron collisions*, *Phys.Rev.* **D48** (1993) 3160–3166, [hep-ph/9305266].

[97] S. Catani, Y. L. Dokshitzer and B. Webber, *The K^- perpendicular clustering algorithm for jets in deep inelastic scattering and hadron collisions*, *Phys.Lett.* **B285** (1992) 291–299.

[98] M. Cacciari and G. P. Salam, *Dispelling the N^3 myth for the k_t jet-finder*, *Phys.Lett.* **B641** (2006) 57–61, [hep-ph/0512210].

[99] M. Cacciari, G. P. Salam and G. Soyez, *FastJet User Manual*, *Eur.Phys.J.* **C72** (2012) 1896, [1111.6097].

[100] M. S. Amjad et al., *A precise characterisation of the top quark electro-weak vertices at the ILC*, 1505.06020.

[101] H. Abramowicz et al., *Higgs Physics at the CLIC Electron-Positron Linear Collider*, 1608.07538.

[102] J. Fuster, S. Heinemeyer, C. Lacasta, C. Marinas, A. Ruiz Jimeno and M. Vos, *Forward tracking at the next e+ e- collider. Part I. The Physics case*, *JINST* **4** (2009) P08002, [0905.2038].

[103] ATLAS collaboration, G. Aad et al., *Jet mass and substructure of inclusive jets in $\sqrt{s} = 7$ TeV pp collisions with the ATLAS experiment*, *JHEP* **05** (2012) 128, [1203.4606].

[104] D. E. Kaplan, K. Rehermann, M. D. Schwartz and B. Tweedie, *Top tagging: A method for identifying boosted hadronically decaying top quarks*, *Phys. Rev. Lett.* **101** (Oct, 2008) 142001.

[105] J. M. Butterworth, A. R. Davison, M. Rubin and G. P. Salam, *Jet substructure as a new Higgs search channel at the LHC*, *Phys. Rev. Lett.* **100** (2008) 242001, [0802.2470].

[106] S. D. Ellis, C. K. Vermilion and J. R. Walsh, *Techniques for improved heavy particle searches with jet substructure*, *Phys. Rev.* **D80** (2009) 051501, [0903.5081].

[107] D. Krohn, J. Thaler and L.-T. Wang, *Jet Trimming*, *JHEP* **02** (2010) 084, [0912.1342].

[108] B. Nachman, P. Nef, A. Schwartzman, M. Swiatlowski and C. Wanotayaroj, *Jets from Jets: Re-clustering as a tool for large radius jet reconstruction and grooming at the LHC*, *JHEP* **02** (2015) 075, [1407.2922].

[109] L. Randall and R. Sundrum, *A Large mass hierarchy from a small extra dimension*, *Phys.Rev.Lett.* **83** (1999) 3370–3373, [hep-ph/9905221].

[110] A. Pomarol and J. Serra, *Top quark compositeness: Feasibility and implications*, *Phys. Rev. D* **78** (Oct, 2008) 074026.

[111] I. García García, *Top quark studies at a Linear Collider*. Universitat de Valencia, 2012, http://digital.csic.es/handle/10261/64306.

[112] J. Fuster, I. García, P. Gomis, M. Perelló, E. Ros and M. Vos, *Study of single top production at high energy electron positron colliders*, *Eur. Phys. J.* **C75** (2015) 223.

[113] CLICdp, ILC Physics and Detector Study collaboration, I. García, *Measurement of the top quark mass and couplings at Linear Colliders*, *Nucl. Part. Phys. Proc.* **273-275** (2016) 2307–2310.

[114] E. Boos, M. Dubinin, A. Pukhov, M. Sachwitz and H. J. Schreiber, *Single top production in e+ e-, e- e-, gamma e and gamma gamma collisions*, *Eur. Phys. J.* **C21** (2001) 81–91, [hep-ph/0104279].

[115] G. L. Kane, G. A. Ladinsky and C. P. Yuan, *Using the top quark for testing standard-model polarization and* CP *predictions*, *Phys. Rev. D* **45** (Jan, 1992) 124–141.

[116] L. Labun and J. Rafelski, *Top anomalous magnetic moment and the two photon decay of Higgs*, 1209.1046.

[117] W. Bernreuther, O. Nachtmann, P. Overmann and T. Schroder, *Angular correlations and distributions for searches of CP violation in top quark production and decay*, *Nucl. Phys.* **B388** (1992) 53–80.

[118] W. Bernreuther, A. Brandenburg and P. Overmann, *CP nonconservation in top quark production by (un)polarized e^+e^- and $\gamma\gamma$ collisions*, in *e+ e- collisions at TeV energies: The physics potential. Proceedings, Workshop, Annecy, France, February 4, 1995, Gran Sasso, Assergi, Italy, June 2-3, 1995, Hamburg, Germany, August 30-September 1, 1995*, pp. 49–56, 1996. hep-ph/9602273.

[119] W. Bernreuther and P. Overmann, *Probing Higgs boson and supersymmetry induced CP violation in top quark production by (un)polarized electron - positron collisions*, *Z. Phys.* **C72** (1996) 461–467, [hep-ph/9511256].

[120] S. J. Parke and Y. Shadmi, *Spin correlations in top quark pair production at e^+e^- colliders*, *Phys.Lett.* **B387** (1996) 199–206, [hep-ph/9606419].

[121] C. R. Schmidt, *Top quark production and decay at next-to-leading order in e+ e- annihilation*, *Phys.Rev.* **D54** (1996) 3250–3265, [hep-ph/9504434].

[122] W. Bernreuther et al., *Top quark physics: Theoretical aspects*, in *Workshop on Physics and Experiments with Linear Colliders Saariselka, Finland, September 9-14, 1991*, 1991.

[123] F. Richard, "CP violation with top quarks at ILC." http://indico.lal.in2p3.fr/materialDisplay.py?contribId=3&materialId=slides&confId=2104, Mar, 2013.

[124] T. Behnke et al., *ILC TDR and DBD, ILC-Report-2013-040* .

[125] J. Rouëné, *A Highly Granular Silicon-Tungsten Electromagnetic Calorimeter and Top Quark Production at the International Linear Collider*. Thesis, Université Paris Sud - Paris XI, June, 2014.

[126] M. Amjad, M. Boronat, T. Frisson, I. Garcia, R. Poschl et al., *A precise determination of top quark electro-weak couplings at the ILC operating at* $\sqrt{s} = 500$ *GeV*, 1307.8102.

[127] G. Moortgat-Pick, T. Abe, G. Alexander, B. Ananthanarayan, A. Babich et al., *The Role of polarized positrons and electrons in revealing fundamental interactions at the linear collider*, *Phys.Rept.* **460** (2008) 131–243, [hep-ph/0507011].

[128] S. K. Gupta, A. S. Mete and G. Valencia, *cp violating anomalous top-quark couplings at the lhc*, *Phys. Rev. D* **80** (Aug, 2009) 034013.

[129] S. Poss and A. Sailer, *Luminosity Spectrum Reconstruction at Linear Colliders*, *Eur. Phys. J.* **C74** (2014) 2833, [1309.0372].

[130] G. Guennebaud, B. Jacob et al., "Eigen v3." http://eigen.tuxfamily.org, 2010.

[131] U. Baur, A. Juste, L. H. Orr and D. Rainwater, *Probing electroweak top quark couplings at hadron colliders*, *Phys. Rev.* **D71** (2005) 054013, [hep-ph/0412021].

[132] M. Vos et al., *Top physics at high-energy lepton colliders*, 1604.08122.

[133] ECFA/DESY LC Physics Working Group collaboration, J. Aguilar-Saavedra et al., *TESLA: The Superconducting electron positron linear collider with an integrated x-ray laser laboratory. Technical design report. Part 3. Physics at an e+ e- linear collider*, hep-ph/0106315.

[134] P. Khiem, E. Kou, Y. Kurihara and F. L. Diberder, *Probing New Physics using top quark polarization in the* $e^+e^- \to t\bar{t}$ *process at future Linear Colliders*, 1503.04247.

[135] P. Janot, *Top-quark electroweak couplings at the FCC-ee*, *JHEP* **04** (2015) 182, [1503.01325].

[136] W. J. Stirling, *Hard QCD working group: Theory summary*, *J.Phys.* **G17** (1991) 1567–1574.

[137] J. Alwall, R. Frederix, S. Frixione, V. Hirschi, F. Maltoni, O. Mattelaer et al., *The automated computation of tree-level and next-to-leading order differential cross sections, and their matching to parton shower simulations*, *JHEP* **07** (2014) 079, [1405.0301].

Agradecimientos

Bueno, esto se acabó y tengo que decir que estoy enormemente agradecido por todo lo que he vivido estos cuatro años. No sólo ha sido una formación académica y profesional, personalmente me ha aportado incluso más. He tenido que asumir retos y superarme en cosas las cuales me veía incapaz de afrontar años atrás. Cada persona con la que he hablado, cada lugar en el que he estado y cada momento vivido son ahora parte de mi.

Por otro lado me entristece que esto se acabe, el doctorado para mí es una experiencia que recomiendo, ha sido una de las etapas más bonitas y enriquecedoras de mi vida. Me llevo amigos inigualables y termino con más fuerza y más ganas de superarme y luchar por lo que quiero y los que quiero.

Quiero agradecer de corazón a Marcel todo lo que ha hecho por mí, ha sido un magnífico tutor. Me siento afortunado de haber sido dirigido por él durante estos años. Es un brillantísimo investigador, pero su calidad humana incluso lo supera. Siempre ha apostado por mí y me ha ayudado muchísimo a crecer como físico. Como no, agradecer a Eduardo toda la física que me ha enseñado y sus peculiares lecciones que te hacen ver las cosas con más claridad y realismo.

También me siento agradecido por haber trabajado dentro de un grupo de investigación de personas llanas y muy profesionales. Agradecer a Juan por sus sabios consejos y el aprecio con el que me ha tratado desde el primer día. No podían faltar mis compañeros, Miguel Ángel, Deltoro, Marçà, Martín y Pablo G. Por todos esos días de trabajo juntos y por supuesto, el pincho de tortilla, las tostadas con tomate, los cruasanes, los zumos ácidos y los cafés amargos de las 11:00h. ¡Gracias amigos!

Quiero hacer mención especial a tres grandes amigos que iniciaron conmigo el doctorado, Carlos, Pablo y Víctor, empezamos juntos, acabamos juntos y seguiremos juntos. Esos inicios en Benimaclet, en los que se fundó el grupo de Birras, irán siempre conmigo. Hemos conseguido ampliar el grupo con grandes personas y ahora también grandes amigos. Gracias a todos vosotros por escuchar mis impectaculares e ingeniosos juegos de palabras, sólo vosotros sabéis apreciarlos de verdad.

A mis padres, José Luis y Nieves, y a mi hermano, Pepe, decirles que ¡Lo conseguí! y que los quiero con locura. Todos teníamos miedo, yo el primero, cuando aquel adolescente tímido y vergonzoso de 17 años salió de casa por primera vez en 2006 rumbo a una nueva vida. Gracias a su amor incondicional y su apoyo, ese muchacho se hizo cada día más fuerte y más optimista para afrontar la realidad y llegar donde ha llegado. Durante mi camino del doctorado conocí a alguien muy especial, Esther,

mi compañera, mi amiga, mi confidente y mi amor. Cada día me ha apoyado y me ha dado un cariño que no se puede describir con palabras. Me considero una persona ambiciosa y fuerte, pero junto a ella no tengo límites.

Esta tesis es fruto de muchos años de esfuerzo, de malos momentos y muy buenos y quiero dedicársela especialmente a ellos cuatro. Son el pilar central de mi vida y agradezco cada día que paso con ellos.